Title

Quantifying sediment resuspension linkages to nutrient enrichment in the existing and future Salton Sea

Authors

Schladow, S. Geoffrey
Fleenor, Wm. E.
Bombardelli, Fabian A
et al.

Publication Date

2007-12-01

Quantifying Sediment Resuspension Linkages to Nutrient Enrichment in the Existing and Future Salton Sea

Principle Investigator:
S. Geoffrey Schladow
Professor, Department of Civil and Environmental Engineering
and
Director, Tahoe Environmental Research Center
University of California, Davis
gschladow@ucdavis.edu
(530) 752 6932 phone
(530) 752 7872 fax

Report Authors:
S. Geoffrey Schladow
Wm. E. Fleenor
Fabián A. Bombardelli
Eu Gene Chung

UC Water Resources Center Technical Completion Report
Project No. W-998

December 2007

ABSTRACT
The UC Davis research involved a 24-month study (including a 4-month measurement program) in the Salton Sea to directly measure sediment resuspension using an array of OBS instruments and an acoustic wave height and current profiling instrument (AWAC). The data provided by these instruments, in conjunction with existing UC Davis temperature recording instruments in the Sea and the existing CIMIS meteorological network, point to the existence of a quasi-equilibrium condition for the suspension of sediments in the lake.

Non-linear relations were developed between the wind intensity and turbidity near which were in relative agreement with relationships from reviewed literature. In particular, the extended García and Parker formulation with DLM-WQ shows the best prediction to describe the seasonal trends as well as short-term variations. The relationship was incorporated into the existing DLM-WQ model.

DLM-WQ, combined with this new sediment model, was used to more fully explore the potential for ecological restoration of the Salton Sea under possible future configurations. Two scenarios, the North Sea Combined Alternative and South Sea Combined Alternative, as suggested by PEIR were examined. The simulation of North Sea Combined Alternative indicates that the Marine Sea might have a better eutrophic status than that of the whole Sea because of fewer sediment resuspension events due to lower average wind speed acting on a smaller surface. On the other hand, the simulation of South Sea Combined Alternative suggested that the concentrations of nutrients in the water column would be the same or higher than those of the whole Sea, because of more sediment resuspension events due to higher average wind speed and due to shallower water depth. In the both alternatives, however, the anoxia in the hypolimnion would be spatially and temporally increased due to increased stratification periods, during which time toxic substances (such as hydrogen sulfide) and organic materials could be accumulated in the sediments.

DLM-WQ with the new sediment algorithm successfully accounts for the dominant processes that control eutrophication in the current Salton Sea and provides an indication of variations in properties that could be expected in potential future configurations. In addition to being a tool for comparing future configurations, DLM-WQ provides a basis for designing future monitoring needs.

CHAPTER 1: Introduction and Problem Statement

The Salton Sea is a hyper-saline "lake" located in a desert basin in southern California, East of Los Angeles and San Diego (see Figure 1.1). It occupies the northern part of the Salton Trough that includes the Coachella and Imperial Valleys of California and the Mexicali Valley of Mexico. The Sea has no outlets due to its location, and can be characterized as a terminal lake.

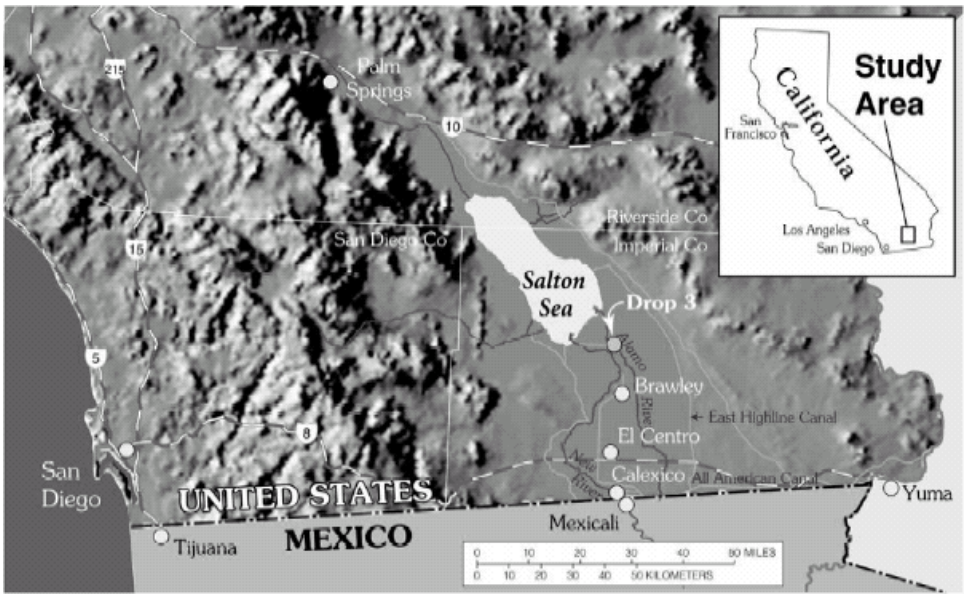

Figure 1.1 Salton Sea basin and surrounding area of California, U.S.A. and Mexico. Source: (Schroeder et al., 2002).

The Salton Sea has been filled with water from the Colorado River many times in the geological past. According to the Department of Water Resources (http://www.crss.water.ca.gov/),

"… The Colorado River is California's largest interstate water source. Rights to use of Colorado River water have been established through a complex framework of statutes and court decisions. California had historically been able to use as much as 800,000 acre-feet annually more than its basic interstate apportionment (consumptive use of 4.4 million acre-feet annually plus half of any surplus water) because of wet hydrologic conditions and because other Colorado River Basin states were not using their full apportionments. By the early 1990s Arizona and Nevada neared use of their full apportionments, setting the stage for negotiations among California's local agency users of Colorado River water that eventually culminated in execution of the Quantification Settlement Agreement (QSA) in October 2003. …"

This agreement has been signed between the Imperial Irrigation District (IID), the Coachella Valley Water District and the Metropolitan Water District of Southern

California (MWDSC) for an agriculture-to-urban water transfer of part of the California's allotment of Colorado River water.

Under the 2003 Colorado River QSA and Salton Sea ecosystem restoration legislation, it becomes the responsibility of California's Resource Agencies to restore the ecological well being of the Sea while at the same time preserving its federal status as a repository for agricultural waste. However, due to the diversions (up to 20% of the current inflow), this restoration will be for a lake that is much smaller than the existing Salton Sea.

Besides reduced inflows and mounting salinity concentrations, probably the most severe of the Salton Sea's issues is its water quality. The Sea is a highly eutrophic water body, characterized by high nutrient concentrations, high algal biomass as demonstrated by high chlorophyll *a* concentrations, high fish productivity, low clarity, frequent very low dissolved oxygen concentrations, massive fish kills, and noxious odors (Holdren and Montaño, 2002; Setmire et al., 2000; Watts et al., 2001). Its eutrophic condition is believed to be controlled, or limited, by phosphorus concentrations in the Sea. Until recently it was widely held that the control of nutrient loads to the Sea had the potential to alleviate eutrophication, and the Regional Water Quality Control Board of California is currently developing a TMDL for inflow nutrients. However, recent computer modeling, performed in support of developing a TMDL, strongly suggests that internal loading via resuspension of nutrients in both particulate and dissolved form (from sediment porewater), rather than external loading, is the most dominant factor in the Sea's nutrient cycling (Schladow et al., 2004). Factors that pointed to this conclusion were the extremely episodic fluctuation of the total phosphorus concentrations measured at three stations by Holdren and Montaño (2002), and the fact that the fluctuations of total mass of phosphorus in the water column was orders of magnitude larger than the stream input of phosphorus.

The possibility that internal nutrient loading driven by resuspension may be such a dominant factor in the ecological status of the Sea casts a tremendous uncertainty on the future restoration efforts. Numerous "alternative" restoration scenarios have been developed by groups with a direct interest in the Sea (although none have yet been adopted by the Resources Agency). These range from the building of a dam across the Sea to divide it in half and preserve the current water level in just one half of the lake, to simply allowing the Sea to recede into a smaller water body. The differences in the costs between various alternative scenarios are many hundreds of millions of dollars, yet the effectiveness of any scenario may be impossible to determine without better information on sediment resuspension. Whatever the final scenario is, the Sea's ecological restoration is still tied to controlling the nutrient fluxes that drive the process of eutrophication.

The importance of sediment resuspension in shallow and wind-exposed lakes has resulted in the development of several models attempting to describe the relation between wind and sediment resuspension rates (Aalderink et al., 1985; Bailey and Hamilton, 1997; Blom et al., 1992; Hawley and Lee, 1999; Hawley and Lesht, 1992; James et al., 1997; Kristensen et al., 1992; Lindstrom et al., 1999; Luettich et al., 1990; Somlyody,

1986; Strehlow et al., 2005). The rate of sediment resuspension (or entrainment rate of sediment into the water column) is a function of the vertical turbulent Reynolds flux of solid particles very close to the bottom, ϕ_E , as follows:

$$\phi_E = \overline{w'\, c'} \tag{1.1}$$

where w' and c' denote the fluctuations of the vertical component of velocity and the concentration, respectively, and the horizontal overbar denotes temporal averaging. In most cases of interest, this flux will be directed upward from the bed. When divided by w_s, E_s is obtained, which is a dimensionless coefficient describing the entrainment of bed sediment into suspension due to turbulence (García and Parker, 1991). When the suspension is in equilibrium, $E_s = c_{ae}$, where c_{ae} is the equilibrium near-bed concentration. It can be assumed that the same relation holds for disequilibrium suspensions as well, for mild disequilibrium conditions. Most of the available models to compute E_s establish dependence on the bottom-shear stresses due to the motion of the underlying fluid and on the local sediment characteristics, usually through a given measure of the sediment size (Sanford and Maa, 2001).

However, mathematical formulations for the computation of the sediment entrainment rate can give widely disparate values under the same set of conditions, leading to confusion and problematic interpretation, which adds to the inherent complexity in understanding lacustrine flows. The mathematical treatments of entrainment formulations differ considerably according to: a) the nature of the behavior of the sediment (*cohesive* or non-*cohesive*); b) the type of erosion observed (Sanford and Maa, 2001); c) the way the critical bottom shear stress is defined; d) the nature of the flow (steady or unsteady); etc. (Sanford and Maa, 2001). This situation generates a considerable degree of uncertainty when relatively-accurate predictions are required to assess the impact of sediment resuspension in wind-exposed lakes.

In order to quantify sediment resuspension, two general methods are widely used. The one is the continuous method, which measures sediment (or a surrogate of it) in the water column continuously by using beam transmissometers and optical backscatter sensors (OBS) (Gloor et al., 1994; James et al., 1997; Jin and Wang, 1998; Weyhenmeyer et al., 1995). The other is the integrated method by using sediment traps (Evans, 1994; Jurg, 1996; Kozerski, 1994; Lindstrom et al., 1999; Rosa et al., 1983), and isotopic tracers (Bloesch, 1994; 1994). Sediment traps directly measure the total sediment falling through the water column at a location, however, can tell little about the dynamics or the frequency of the process. By contrast, the continuous method allows for the direct measurement of resuspension as it occurs at a particular location, which is ideal for model validation.

In this research, results of a project are reported aimed at understanding the sediment resuspension phenomenon in the Salton Sea and its role in the water quality of the lake, by in-situ measuring resuspension with an array of OBS and an acoustic wave height and current profiling instrument (AWAC). The data collected by these

instruments, in conjunction with existing UC Davis temperature instruments in the Sea and the California Irrigation Management Information System (CIMIS) meteorological network, provide information to develop a new, process-based resuspension algorithm, and to fully calibrate and validate it as part of a hydrodynamic and water quality model, Dynamic Lake Model – Water Quality (DLM-WQ). The model can then be used to more fully explore the potential for ecological restoration of the Salton Sea, either under its present geometrical configuration or possible future configurations. The model, which is in the public domain, is also applicable to many other lakes and reservoirs where sediment resuspension or the nutrients and contaminants that are associated with the sediments are an issue.

This report is arranged as follows. Chapter 2 describes the Salton Sea, its geography and ecological significance and its water quality conditions as well as the characteristics of bed sediments. The chapter also includes the theoretical approach of sediment resuspension, the computations of shear stresses both by wind-induced currents and waves, and a predictive model of wave characteristics (i.e. Sverdrup-Munk-Bretschneider (SMB) method predicting wave heights and periods).

Chapter 3 describes the data collection program that was undertaken as part of this study, and the data analysis and interpretation. The data collection program consisted primarily of the installation of three sediment observation stations, a Nortek acoustic wave and current profiler (AWAC) and 10 thermistor chains in the Salton Sea. The intended purpose was to provide an assessment of the times and frequency of sediment resuspension in the Sea. The analysis that has been performed to date represents the relation among sediment resuspension and flow variables, such as wind speed and wave heights. Also computed are sediment entrainment rates using two sediment entrainment models, for *cohesive* sediments represented as Mian and Yanful (2004) and for the non-*cohesive* sediments as an extended García and Parker formulation, respectively.

Chapter 4 describes the physical and ecological processes of DLM-WQ and the sediment resuspension models which are incorporated into DLM-WQ. Each of the DLM-WQ models with new sediment resuspension relationships is calibrated and the results are presented. These simulations provide a means to investigate the potential for eutrophication reduction for the historic Salton Sea configuration, and several of the proposed future configurations of the Salton Sea. Section 5 summarizes the major findings of the study, and makes specific recommendations for improving the modeling capability for the Salton Sea.

References

Aalderink, R. H., Lijklema, L., Breukelman, J., Vanraaphorst, W., and Brinkman, A. G. 1985. Quantification of Wind Induced Resuspension in a Shallow Lake. Water Science and Technology **17:** 903-914.

Bailey, M. C., and Hamilton, D. P. 1997. Wind induced sediment resuspension: A lake-wide model. Ecological Modelling **99:** 217-228.

Bloesch, J. 1994. A Review of Methods Used to Measure Sediment Resuspension. Hydrobiologia **284:** 13-18.

Bloesch, J. 1994. Sediment Resuspension in Lakes - Introduction to a Series of Papers Given in a Special Session at the Xxvth Congress of the International-Association-of-Limnology (Sil), 21-27 August 1992, Barcelona, Spain - Editorial. Hydrobiologia **284:** 1-3.

Blom, G., Vanduin, E. H. S., Aalderink, R. H., Lijklema, L., and Toet, C. 1992. Modeling Sediment Transport in Shallow Lakes - Interactions between Sediment Transport and Sediment Composition. Hydrobiologia **235:** 153-166.

Evans, R. D. 1994. Empirical-Evidence of the Importance of Sediment Resuspension in Lakes. Hydrobiologia **284:** 5-12.

García, M., and Parker, G. 1991. Entrainment of Bed Sediment into Suspension. Journal of Hydraulic Engineering-Asce **117:** 414-435.

Gloor, M., Wuest, A., and Munnich, M. 1994. Benthic Boundary Mixing and Resuspension Induced by Internal Seiches. Hydrobiologia **284:** 59-68.

Hawley, N., and Lee, C. H. 1999. Sediment resuspension and transport in Lake Michigan during the unstratified period. Sedimentology **46:** 791-805.

Hawley, N., and Lesht, B. M. 1992. Sediment Resuspension in Lake St-Clair. Limnology and Oceanography **37:** 1720-1737.

Holdren, G. C., and Montaño, A. 2002. Chemical and physical characteristics of the Salton Sea, California. Hydrobiologia **473:** 1-21.

James, R. T., Martin, J., Wool, T., and Wang, P. F. 1997. A sediment resuspension and water quality model of Lake Okeechobee. Journal of the American Water Resources Association **33:** 661-680.

Jin, K. R., and Wang, K. H. 1998. Wind generated waves in Lake Okeechobee. Journal of the American Water Resources Association **34:** 1099-1108.

Jurg, B. 1996. Towards a new generation of sediment traps and a better measurement/understanding of settling particle flux in lakes and oceans: A hydrodynamical protocol. Aquatic Sciences **58:** 283-296.

Kozerski, H. P. 1994. Possibilities and Limitations of Sediment Traps to Measure Sedimentation and Resuspension. Hydrobiologia **284:** 93-100.

Kristensen, P., Sondergaard, M., and Jeppesen, E. 1992. Resuspension in a Shallow Eutrophic Lake. Hydrobiologia **228:** 101-109.

Lindstrom, M., Hakanson, L., Abrahamsson, O., and Johansson, H. 1999. An empirical model for prediction of lake water suspended particulate matter. Ecological Modelling **121:** 185-198.

Luettich, R. A., Harleman, D. R. F., and Somlyody, L. 1990. Dynamic Behavior of Suspended Sediment Concentrations in a Shallow Lake Perturbed by Episodic Wind Events. Limnology and Oceanography **35:** 1050-1067.

Rosa, F., Nriagu, J. O., Wong, H. K., and Burns, N. M. 1983. Particulate Flux at the Bottom of Lake-Ontario. Chemosphere **12:** 1345-1354.

Sanford, L. P., and Maa, J. P. Y. 2001. A unified erosion formulation for fine sediments. Marine Geology **179:** 9-23.

Schladow, S. G., Robertson, D. M., Hook, S. J., Chung, E. G., Losada, J. P., Cardona, B. M., Palmarsson, S. O., Steissberg, T. E., and Fleenor, W. E. 2004. Salton Sea Nutrients TMDL Modeling Studies. Colorado River Basin Regional Water Quality Control Board.

Schroeder, R. A., Orem, W. H., and Kharaka, Y. K. 2002. Chemical evolution of the Salton Sea, California: nutrient and selenium dynamics. Hydrobiologia **473:** 23-45.

Setmire, J., Holdren, C., Robertson, D., Amrhein, C., Elder, J., Schroeder, R., Schladow, G., McKellar, H., and Gersberg, R. 2000. Eutrophic Conditions at the Salton Sea. *In* Setmire, J. [ed.], Eutrophication Workshop. The Salton Sea Authority, the Salton Sea Science office, USBR.

Somlyody, L. 1986. Wind induced sediment resuspension in shallow lakes, p. 287-298. *In* Bhra, T. F. E. C. [ed.], Water Quality Modelling in the Inland Natural Environmnet. BHRA, The Fluid Engineering Centre.

Strehlow, K., Davis, J., Sim, L., Chambers, J., Halse, S., Hamilton, D., Horwitz, P., McComb, A., and Froend, R. 2005. Temporal changes between ecological regimes in a range of primary and secondary salinised wetlands. Hydrobiologia **552:** 17-31.

Watts, J. M., Swan, B. K., Tiffany, M. A., and Hurlbert, S. H. 2001. Thermal, mixing, and oxygen regimes of the Salton Sea, California, 1997-1999. Hydrobiologia **466:** 159-176.

Weyhenmeyer, G. A., Meili, M., and Pierson, D. C. 1995. Simple Method to Quantify Sources of Settling Particles in Lakes - Resuspension Versus New Sedimentation of Material from Planktonic Production. Marine and Freshwater Research **46:** 223-231.

CHAPTER 2: BACKGROUND

The Salton Sea is saline, located below sea level and in a desert area as are many terminal lakes (Cooper and Koch, 1984). The Salton Sea occupies the lowest portion of a structural basin, the Salton Trough. Mountains, including the Santa Rosa Range to the west, Orocopia Mountains to the north and the Chocolate Mountains to the east, surround the closed basin (Salton Sea Authority, 2000).

Geography and its ecological significance

The Salton Sea initially formed during the 17 months from October 1905 to February 1907 when the main flow of the Colorado River was diverted into the Salton Trough by way of failed irrigation diversion structures. The diversion took place through poorly-built levees. Until the closure of the break, floodwaters flowed and filled the basin, and the Salton Sea's elevation reached -195 ft Mean Sea Level (MSL), with a surface area 520 square miles. Evaporation and lack of significant tributary inflow caused the Sea's elevation to gradually recede to a low of -250 ft MSL by 1925. From 1925 to the mid 1980's, the elevation of the Salton Sea gradually increased to its current level of approximately -227 ft MSL as a result of increased agricultural discharge. The Sea is now sustained primarily through irrigation return flows from the Imperial, Coachella, and Mexicali Valleys. Rainfall and small volumes of municipal effluent and storm water runoff help supplement the agricultural drainage (Carpelan, 1958; Cook et al., 2002).

The bathymetry of the Salton Sea is shown in Figure 2.1 with five feet contours. The length of the Sea is over 35 miles along a northwest/southeast axis, and the width is 15 miles. Its southern half is broader than the northern half. It constitutes the largest body of water in the State, encompassing 376 square miles with a maximum depth of 51 feet. Its total volume is about 7.5 million acre-feet (maf).

The Salton Sea is part of the Colorado Desert ecosystem; the mean annual precipitation is only about 6 cm, while the mean annual evaporation is 180 cm (Ponce). Drought vegetation, such as desert scrub, creosote bush, saltbush, and tamarisk, grows in the Salton Sea basin. Streams and springs, ultimately draining into the Salton Sea, provide an environment for cottonwood, willow, and other plants in freshwater marshes, as well as agricultural lands with crops, which need water imported from the Colorado River (Salton Sea Authority, 2000). In addition, the Sea and the wetlands along its shoreline are a significant region of the Pacific Flyway, a major migratory avian corridor, which supports permanent habitat for wildlife and seasonal refuge to millions of birds representing hundreds of species (Salton Sea Authority, 2000).

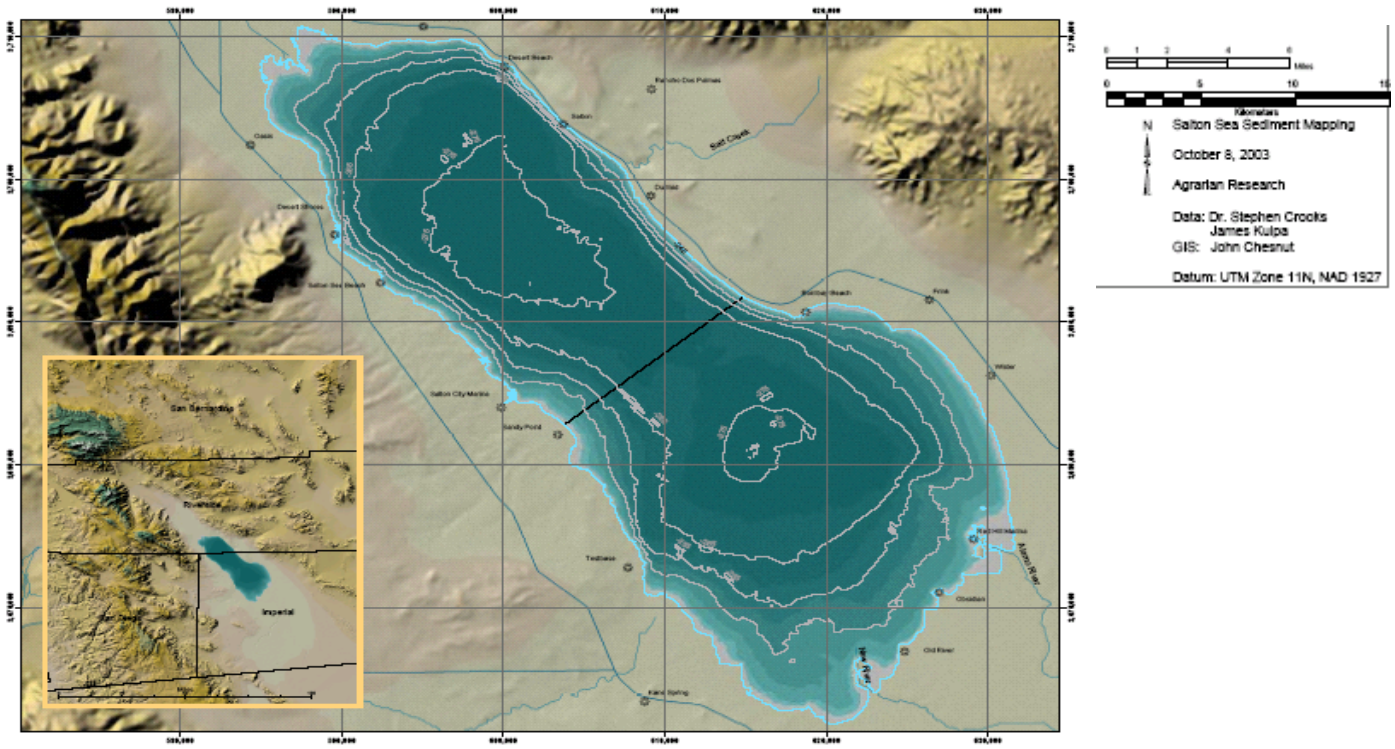

Figure 2.1 Bathymetry of the Salton Sea: five foot contours. Major contours are at 15, 25, 35 and 45 feet. Source: (Scheidlinger et al., 2003).

Water quality conditions

Over many years, water has left the Salton Sea through evaporation, accumulating high concentrations of salt in the Sea. The salinity of the Salton Sea is very high, between 44 and 45 g L^{-1} (ppt), about 30% greater than that of the ocean (Cook et al., 2002) and well above the tolerance for sustained reproduction of most sport fish.

Setmire et al. (2001) summarized what was known about the eutrophication of the Salton Sea at that time. While that report considered nutrient flux loading from sediments, it did so from the classical limnology perspective of phosphorus release under anoxic conditions. Such an increase, however, was never observed in the Salton Sea. In fact, concentrations near the bottom were usually less than near the surface during periods of anoxia. Consequently, Setmire et al. (2001) reported that sediment related release of phosphorus was not relevant at Salton Sea.

Due to the unique chemistry of the Salton Sea, Holdren & Montaño (2002) hypothesized that the low bottom phosphorus concentrations could be caused by the rapid chemical sequestration of phosphorus out of the water column in the form of the precipitation of hydroxyapatite ($Ca_5(PO_4)_3OH$) and fluorapatite ($Ca_5(PO_4)_3F$), which do not solubilize under anoxic conditions, based on the results from geochemical programs, PHRQPITZ and PHREEQC. Therefore, there was no indication of internal loading of phosphorus from the deep sediments, even during extended periods of anoxia, based on

the data collected in 1999. However, they did not consider the possibility of sediment resuspension.

The possibility of sediment resuspension was raised by Anderson (2003) through modeling that described the susceptibility of different parts of the lake to wind resuspension. Large areas were determined to be prone to the possibility of resuspension. Furthermore, as part of the same research, Anderson (2003) found that under laboratory conditions, agitated sediment could release high concentrations of phosphorus.

Sediment resuspension is closely related to hydrodynamic processes, such as wind-induced currents and waves. Wind forcing can not only affect water temperature, DO, and nutrient cycling (Carpelan, 1958; Watts et al., 2001), but also has been shown to affect water quality in shallow water bodies via sediment resuspension (Aalderink et al., 1985; Hamilton and Mitchell, 1997; Luettich et al., 1990; Somlyòdy, 1986). The hydrodynamic behavior of the Salton Sea, as a double gyre circulation pattern and polymixis, is mainly driven by the wind blowing over the long fetch of the lake (Cook et al., 2002). Furthermore, such hydrodynamic behaviors of the Sea may add to the possibility that resuspension of sediment and release of phosphorus may be a dominant factor in the ecological status of the Salton Sea.

DLM-WQ, which had been run for the Salton Sea using the resuspension formula of Somlyody (1986), gave a reasonable match between the scant measured data for orthophosphate concentration and total suspended sediment (TSS) concentration (Schladow et al., 2004). It is noteworthy that when the model was run without including the sediment resuspension algorithm, it was impossible for any of the modeled parameters to approach the measured values. This strongly suggested that a better understanding and representation of sediment (and nutrient) resuspension was essential to address the question of eutrophication control.

Characteristics of bed sediments of the Salton Sea

Sediment characteristics of the Salton Sea have been analyzed by Andersen (2002), and Anderson's sediment analysis data are shown in Table 2.1. Based on these data, a median of the sediments' size was determined assuming the following sediment distribution (Hakanson and Jansson, 1983; Julien, 1998).

Table 2.1 Summary of sediment characterization data (Andersen, 2002)

Property	Size	Units	Mean	Std Dev	Median	Min	Max
Sand	63μm – 2mm	%	24.1	26.3	12.5	0.6	92.5
Silt	2μm – 63μm	%	45.4	17.9	52.2	0.0	68.1
Clay	$2e^{-3}$μm – 2μm	%	30.5	10.4	33.0	7.2	50.3

One could infer from the table that the median of the sediment diameter ranges into the silt category, 2μm – 63μm, since sand and clay are only around 24.1% and 30.5%, respectively. On the other hand, a mean of sediment size, D, can be estimated by the equation below:

$$D = \frac{\sum_i X_i D_i}{\sum_i X_i} \tag{2.1}$$

where X_i denotes percentage of a property i of sediments and D_i denotes diameter of a property i of sediments. The mean is computed using minimum values of each distribution and the result value is 16 μm as follows:

$$D_{\min} = \frac{24.1\% \times 63\mu m + 45.4\% \times 2\mu m + 30.5\% \times 2e-3\mu m}{100\%} = 16.09\mu m \cong 16\mu m$$

Based on the range of the median above, a conservative value for average sediment size of 25 μm was assumed.

Density of sediment is also estimated based on the sediment classification of the Salton Sea. Clay minerals generally include Kaolinite, Montmorillonite/Smectite, Illite (or Clay-mica) and Chlorite, and densities of clay vary from 2.2 to 2.6 g/cm^3 (Hakanson and Jansson, 1983). The most common constituent of sand, in inland continental settings and non-tropical coastal settings, is silica (silicon dioxide), usually in the form of quartz. The density of quartz ranges from 2.5 to 2.8 g/cm^3 and we assume the solid density of the Salton Sea sediments is 2.65 g/cm^3.

SEDIMENT RESUSPENSION

When the water current near a bed is increased from rest, a range of conditions can result. First, particles remain on the bed for small flow velocities. Then, for larger velocities, particles start to move close to the bottom, by rolling and/or saltating. If the velocity of flow is further increased, some of the small particles begin to be "entrained" into suspension (particles are resuspended).

Sediment entrainment rate

Aalderink et al. (1985) compared four formulae for entrainment rates. These formulae are based on: a) only wave-induced motion; b) a theoretical relation for wave-induced resuspension; c) an empirical, site-specific, relation (Somlyòdy, 1981), which is valid for wave-induced resuspension and d) a theoretical relation for only current motion. The four relations give the following proportionalities:

a) $\phi_E \sim u_m$ (where u_m the maximum horizontal velocity at bed due to waves);
b) $\phi_E \sim u_m^{1.875}$;
c) $\phi_E \sim w^m$ (where w is the wind velocity), with m ranging between 1 and 3 and
d) $\phi_E \sim w^p$, with p =2.75 for a wind intensity below 5.67 m/s, and p =3.5 otherwise.

Aalderink et al. (1985) concluded that proposal c), based on data collected from Lake Balaton, Hungary, presented the best agreement with measurements taken in Lake Veluwe, Netherlands.

Furthermore, there is a vast corpus of formulations to compute the entrainment rate of sediment in open-channel flows (García, 1999; García and Parker, 1991). Most of the available relations to predict sediment entrainment, E_S, reviewed by García and Parker (1991) are of the following type:

$$E_S \sim \phi_E \sim \tau_b^P \sim u_*^{2P} \sim w^K \tag{2.2}$$

where τ_b and u_* are the bed shear stress and shear velocity due to skin friction, respectively, and P is an exponent; K is an exponent with values ranging between 3 and 10 depending on the formulation considered. These relations have been developed under steady-state, equilibrium conditions (or, at least, mild disequilibrium conditions), for essentially uni-modal, non-*cohesive* sediment particles, and for a uniform distribution of the shear stress in space. To the best of the authors' knowledge, the formulation by García and Parker (1991) is the only one developed to handle sediment mixtures, i.e., a distribution of sediment sizes; the formula is given by:

$$E_s = \frac{A\ Z_u^5}{1 + \frac{A}{0.3}\ Z_u^5} \tag{2.3}$$

where A is a constant equal to 1.3 x 10^{-7} and $Z_u = \frac{u_*'}{w_s} f\left(\mathrm{Re}_p\right)$, with: $f\left(\mathrm{Re}_p\right) = R_p^{0.6}$ and $\mathrm{Re}_p = \frac{\sqrt{g R D^3}}{\nu}$ being the particle Reynolds number, with: $R = \frac{\rho_s - \rho}{\rho}$ being the submerged specific gravity where ρ is water density, and ρ_s is sediment density; D is

the sediment grain size, g is the acceleration of gravity, and ν is the kinematic viscosity of water. This formula is valid for Re_p ranging from 3.62 to 36.82.

García and Parker (1993) extended their formula to small sediment sizes, down to 100 μm with $1 < \mathrm{Re}_p < 3$. For fine particles: $f(\mathrm{Re}_p) = 0.586\,\mathrm{Re}_p^{1.23}$, with: $w_s = R_f\sqrt{R\,g\,D}$ is sediment fall velocity in still water and $R_f = \exp\left\{-b_1 + b_2\ln(\mathrm{Re}_p) - b_3[\ln(\mathrm{Re}_p)]^2 - b_4[\ln(\mathrm{Re}_p)]^3 + b_5[\ln(\mathrm{Re}_p)]^5\right\}$ with: b_1 = 2.8913494; b_2 = 0.95296; b_3 = 0.056835; b_4 = 0.002892; b_5 = 0.000245 (Dietrich, 1982). The relation by García and Parker (1991; 1993) was later tested for flow pulses by Admiraal et al. (2000), who corroborated that the formula can give satisfactory predictions in unsteady conditions as long as a time delay is applied to account for the lag between the bed shear stress and the entrainment.

A large number of expressions for sediment erosion rates of *cohesive* sediments have been reviewed by Mehta et al. (1982) and Sanford and Maa (2001). Most of those expressions are of the following type (Mehta et al., 1982; Raudkivi, 1990):

$$E = \alpha\left[\frac{\tau_b - \tau_{cr}}{\tau_{cr}}\right]^m \qquad \text{for } \tau \geq \tau_{cr} \qquad (2.4)$$

$$E = 0 \qquad \text{for } \tau \leq \tau_{cr}$$

where E is the net, specific rate of entrainment of sediment in mass area^{-1}time^{-1}; α is a coefficient; m is an exponent ranging from 1 to 2 (Raudkivi, 1990); and τ_{cr} is the critical shear stress. The exponent is equal to 2 in the equation by Mian and Yanful (2004). Expressions for erosion rate of *cohesive* and non-*cohesive* sediments reviewed by Mehta et al. (1982) and García and Parker (1991), respectively, are shown in Table 2.2.

Table 2.2 Formulae to estimate sediment entrainment or near-bed concentration under equilibrium conditions (García and Parker, 1991).

Non-*Cohesive* Sediment		
Author	Formula	Parameters
Einstein (1950)	$c_{ae} = \frac{q_*}{23.2\left(\tau_s^*\right)^{0.5}}$	$q_* = \frac{q_b}{\sqrt{RgD_s}D_s}$
Engelund and Fredsoe (1976; 1982)	$c_{ae} = \frac{0.65}{\left(1+\lambda_b^{-1}\right)^3}$	$\lambda_b = \left[\frac{\tau_s^* - 0.06 - \frac{\beta p \pi}{6}}{0.027(R+1)\tau_s^*}\right]^{0.5}$; $p = \left[1+\left(\frac{\frac{\beta\pi}{6}}{\tau_s^* - 0.06}\right)^4\right]^{-0.25}$; $\beta = 1.0$
Smith and McLean (1977)	$c_{ae} = \frac{0.65\gamma_0 T}{1+\gamma_0 T}$	$T = \frac{\tau_s^* - \tau_c^*}{\tau_c^*}$; $\gamma_0 = 2.4\cdot 10^{-3}$
Itakura and Kishi (1980)	$c_{ae} = k_1\left(k_2 \frac{u_*}{\nu_s}\frac{\Omega}{\tau^*} - 1\right)$	$\Omega = \frac{\tau^*}{k_3}\left(k_4 + \left[\frac{\exp\left(-A_0^2\right)}{\int_{A_0}^{\infty}\exp\left(-\xi^2\right)d\xi}\right]\right) - 1$; $A_0 = \frac{k_3}{\tau^*} - k_4$; $k_1 = 0.008$; $k_2 = 0.14$; $k_3 = 0.143$; $k_4 = 2.0$
Van Rijn (1984)	$c_{ae} = 0.015\frac{D_s}{b}\frac{T^{1.5}}{D_*^{0.3}}$	$D_* = D_s\left(\frac{gR}{\nu^2}\right)^{1/3}$
Celik and Rodi (1984)	$c_{ae} = \frac{k_0 C_m}{I}$	$C_m = 0.034\left[1-\left(\frac{k_s}{H}\right)^{0.06}\right]\frac{u_*^2}{gRH}\frac{U_m}{\nu_s}$;

		$I = \int_{0.05}^{1} \left(\frac{1-\eta}{\eta} \cdot \frac{\eta_b}{1-\eta_b} \right)^{\nu_s / 0.4u_*} d\eta \; ; \eta = z/H \; ; \eta_b = 0.05 \; ; k_0 = 1.13$
Akiyama and Fukushima (1986)	$E_s = 0 \; ; \; Z < Z_c$ $E_s = 3 \cdot 10^{-12} Z^{10} \left(1 - \frac{Z_c}{Z} \right) ; Z_c < Z < Z_m$ $E_s = 0.3 \; ; \; Z > Z_m$	$Z = \frac{u_*}{\nu_s} R_p^{0.5} \; ; R_p = \frac{\sqrt{gRD_s} D_s}{\nu} \; ; \; Z_c = 5 \; ; Z_m = 13.2$
Zyserman and Fredsoe (1994)	$c_{ae} = \frac{0.331 \left(\theta' - 0.045 \right)^{1.75}}{1 + \frac{0.331}{0.46} \left(\theta' - 0.045 \right)^{1.75}}$	$\theta' = \frac{(u_{*s})^2}{RgD_s}$

where q_b = volume bed-load transport rate per unit width;
D_s = grain size;
U_m = mean flow velocity;
H = water depth.

***Cohesive* Sediment**

Author	Formula	Parameters
Partheniades (1962)	$\varepsilon = \alpha_1 \left[1 - \frac{1}{\sqrt{2\pi}} \int_{-c}^{c} \exp\left(-\omega^2 / 2 \right) d\omega \right]$	$c = \left(\beta_1 / \tau \right) - \beta_2$
Christensen (1965)	$\varepsilon = \alpha_2 \left[0.5 - \frac{1}{\sqrt{2\pi}} \int_{0}^{c} \exp\left(-\omega^2 / 2 \right) d\omega \right]$	$c = -6.10 + \left(6.18 / \sqrt{\beta_3 \tau} \right)$
Kandiah (1974); Arulanandan (1975)	$\varepsilon = \alpha_3 \left(\frac{\tau - \tau_c}{\tau_c} \right)$	
Christensen and Das (1973); Raudkivi and Hutchison (1974); Gularte (1978)	$\varepsilon = \beta_4 \exp\left[\alpha_4 \left(\tau - \tau_c \right) \right]$	

Lambermont and Lebon (1977)	$\varepsilon = \alpha_5 \left(\tau^{\beta_4} - \tau_c^{\beta_4} \right) \tau^{1/2}$
Mehta (1981)	$\frac{\varepsilon - \varepsilon_{ch}}{\varepsilon_{ch}} = \alpha_6 \left(\frac{\tau - \tau_{ch}}{\tau_{ch}} \right)$
Krone (1962)	$\varepsilon = \delta_1 t^{-\lambda_1}$
Yeh (1979); Fukuda and Lick (1980)	$\varepsilon = \delta_2 \exp(-\lambda_2 t)$
Thorn and Parsons (1980)	$\varepsilon = \delta_3(z)[\tau - \tau_c(z)]$

where ε = erosion rate [g/cm^2/min];

α, β = coefficients;

τ = bed shear stress;

τ_c = critical shear stress for erosion;

τ_{ch} = characteristic shear stress: when $\tau > \tau_{ch}$, the bed erodes much more rapidly than $\tau < \tau_{ch}$;

ε_{ch} = erosion rate when $\tau = \tau_{ch}$;

δ, λ = empirical constants.

Critical Shields shear stress

The critical shear stress which is introduced in Equation (2.4) is a feature that naturally adds to the uncertainty of entrainment values, and has been given diverse meaning by different authors (Sanford and Maa, 2001). Shields (1936) experimentally determined that a critical Shields stress, τ_c^*, is required to initiate motion of non-*cohesive* particles. Based on Neill (1968), Parker et al. (2003) amended Brownlie's (1981) fitting curve to the experimental line of Shields and the formula is given by (Parker, 2004):

$$\tau_c^* = 0.5\left[0.22\,\mathrm{Re}_p^{-0.6} + 0.06\cdot 10^{\left(-7.7\,\mathrm{Re}_p^{-0.6}\right)}\right] \tag{2.5}$$

$$\tau^* = \frac{\tau_b}{\rho RgD} \tag{2.6}$$

where τ^* denotes dimensionless Shields number and τ_c^* denotes critical Shields number. Assuming the sediment diameter is 25 μm described in the preceding section, the critical Shields shear stress is 0.065927.5 Pa.

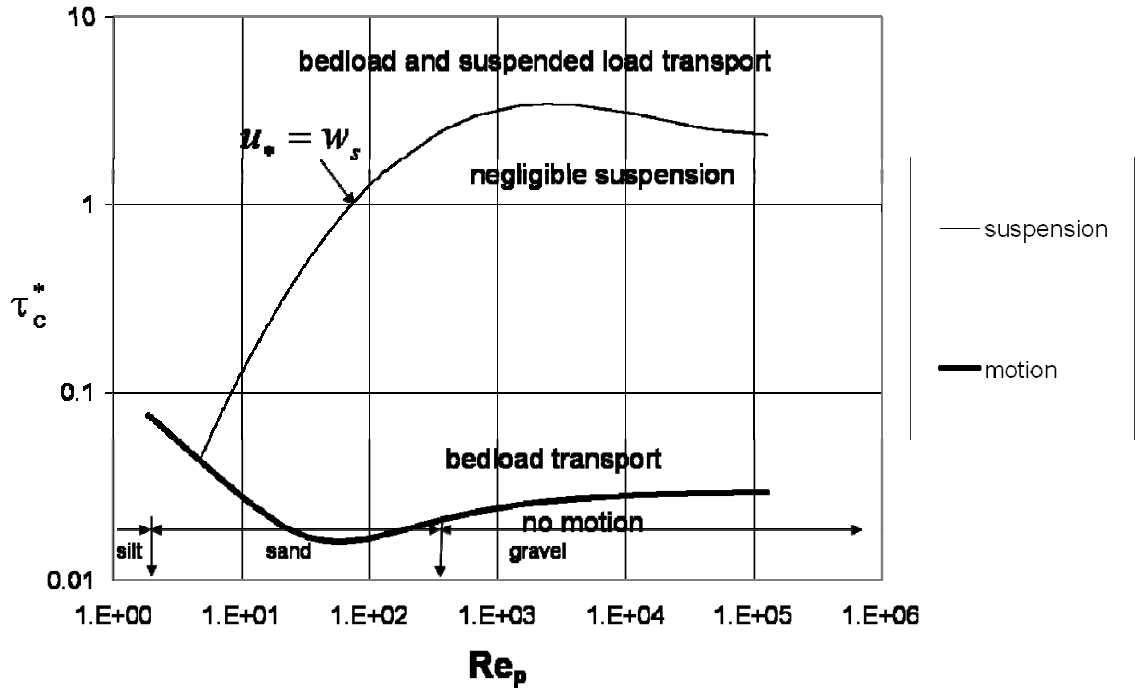

Figure 2.2 Shields regime diagram: The thick solid line approximately divides the regimes of no motion versus motion (normally as bedload) of the surface material at bankfull flow, and the thin solid line plays the same role in regard to significant suspension of the surface material. Source: (Parker, 2004).

Figure 2.2 replicates the so-called Shields regime diagram put forward by Parker (2004). The diagram indicates the initiation of motion curve given by the experimental tests of Shields and the tentative curve of entrainment into suspension, given by the Baguold criterion $u_* = w_s$ (where u_* is the shear velocity and w_s is the settling velocity of the sediment).

Expression for the computations of the shear stress

The most important forcing that causes sediment resuspension in shallow lakes is the wind acting on the water surface, which induces waves, currents and, eventually, surface and internal seiches (Bloesch, 1995). Generally speaking, bed shear stress induced by wind events varies in time and space; furthermore, the bottom shear stress associated with the near-bed wave velocity is usually larger than that associated with the near-bed current velocity in shallow lakes (Hawley et al., 2004; Jin and Wang, 1998; Luettich et al., 1990; Mian and Yanful, 2004). Waves are therefore mostly responsible for the sediment entrainment and, consequently, wave theory has been largely used to estimate wave parameters to quantify the bed shear stress (Anderson, 2003; Bombardelli and García, 1999; Hamilton and Mitchell, 1996; Hawley and Lesht, 1992; Sheng and Lick, 1979). In stratified lakes, bottom shear stresses induced by internal seiches may also be an important driving force for sediment resuspension (Gloor et al., 1994; Shteinman et al., 1997).

Shear stress due to wind-induced currents

Wind can cause currents at the surface in the direction of the wind and/or reverse currents due to pressure near the bottom. Currents, driven by wind, induce shear stresses at the surface as well as the bottom of the lake. Wind induces shear stress at the surface of the lake, τ_0, which is estimated by the quadratic drag stress law as follows (Mian and Yanful, 2004):

$$\tau_o = C_D \rho_a U(10)^2 \tag{2.7}$$

where ρ_a is the density of air, 1.16 at 28 ºC (kg m^{-3}), and C_D is the drag coefficient which can be calculated using Garratt's formula, $C_D = 0.001(0.75 + 0.067U(10))$, and $U(10)$ denotes wind speed at 10 m above the water surface (m/s). The bottom shear stress due to return currents is about 10% of the surface wind induced shear stress as follows:

$$\tau_{curr} = 0.1 C_D \rho_a U(10)^2 \tag{2.8}$$

Shear stress due to wind-induced waves

The maximum shear stress exerted on the bottom sediments due to wind-induced waves, τ_{wave}, is estimated by the below equation (Mian and Yanful, 2004):

$$\tau_{wave} = 0.5 f_W \rho U_W^2 \tag{2.9}$$

where U_W is wave orbital velocity: $U_W = \frac{H\pi}{T \sinh\left(\frac{2\pi d}{L}\right)}$ and f_W is bottom friction factor: $f_W = \frac{2}{\sqrt{R_W}}$; R_W is Reynolds number: $R_W = \frac{U_W A_W}{\nu}$ and A_W is maximum displacement of the individual fluid particles from their mean position: $A_W = \frac{U_W}{\omega}$.

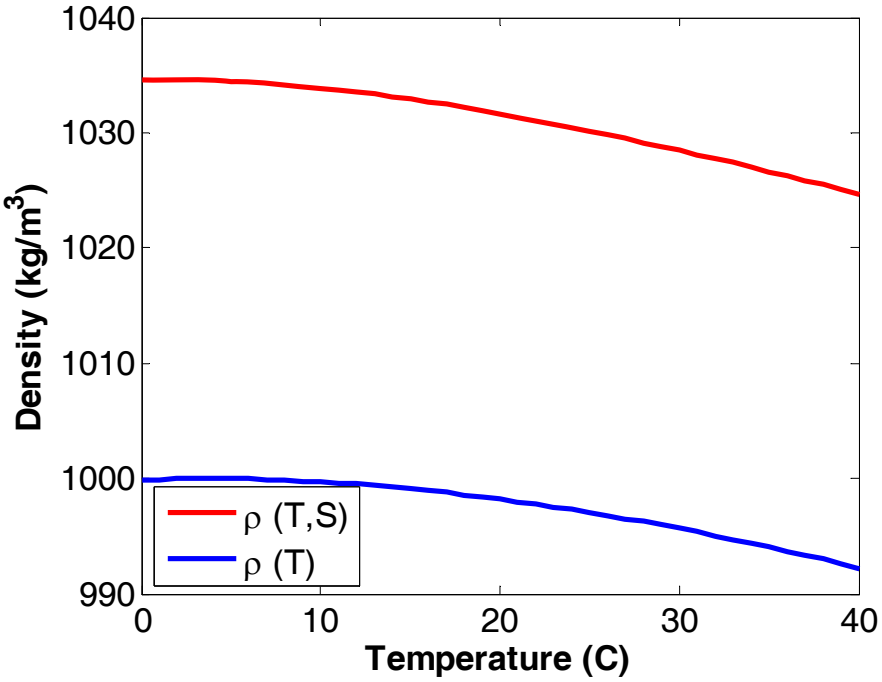

Figure 2.3 Comparison of the simulated water densities by the equations of state for sea water by UNESCO: Blue line indicates water density calculated only as a function of Temperature (ºC); red line indicates water density calculated as a function of Temperature (ºC) and salinity 44 ppt.

The water density, ρ, is controlled by high temperatures and high salinity of the Salton Sea. Using well-know formula, the equations of state for sea water (covering salinity from 42 ppt to 50 ppt) by UNESCO (Poisson et al., 1991), the water density of the Sea with an average value of salinity 44 mg L^{-1} (ppt) is calculated at 1029 kg m^{-3} for 28 ºC. The kinematic viscosity of water, ν, is 0.82×10^{-6} m^2 s^{-1} for 28 ºC. In Figure 2.3 the simulated water densities due to temperature alone and due to both temperature and salinity using the equations of state for seawater are compared. Analysis of the figure shows the water density with high salinity is heavier than that of fresh water.

In Figure 2.4 a comparison of the calculated bed shear stresses as a function of wind speed (m/s) according to Equations (2.12) – (2.15) is made with the critical Shields shear stress estimated by Equations (2.5) – (2.6).

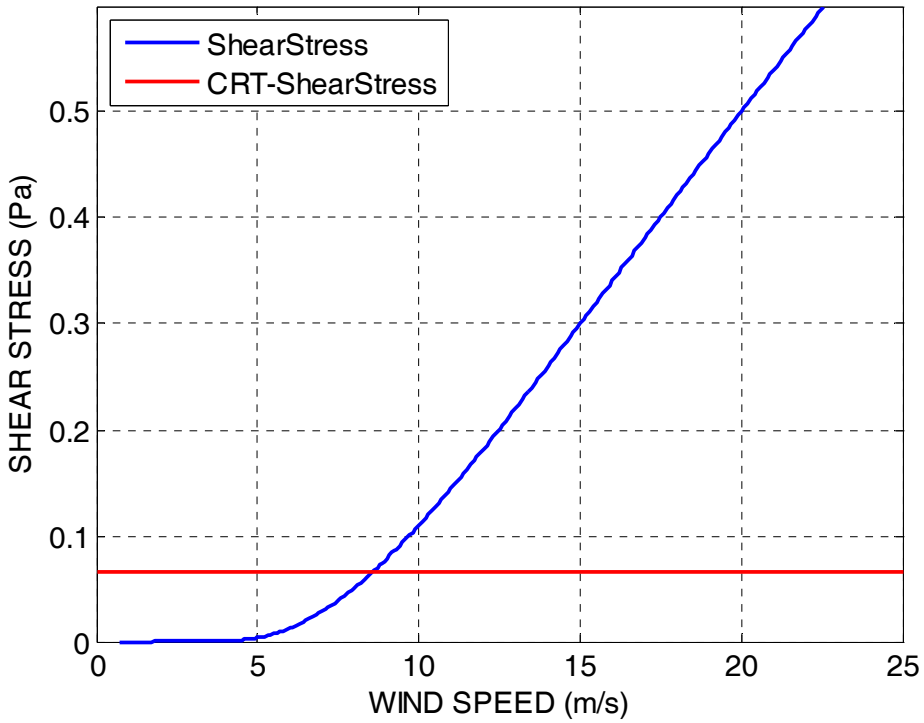

Figure 2.4 Calculated shear stresses as a function of wind speed (m/s). Blue line indicates bed shear stress (Pa) and red line indicates a critical Shields shear stress (Pa).

Computations of wind-induced wave characteristics

Since waves are mainly responsible for the sediment entrainment in shallow lakes, one of the commonly used wave theories to estimate wave parameters to quantify the bed shear stress is presented in this section. Prior to computation of wave characteristics, a water body should first be classified as deep water, shallow water or transitional

according to the water depth and the wavelength which affect wave propagation as shown in Table 2.3. For this classification, the water depth of the Salton Sea is assumed to be 10 m (as was done for the previous water quality modeling in the TMDL research), thereby assuming that sediment resuspension is not significant below this depth. The wavelength of the Sea can also be estimated using following equations by CERC (1984):

$$L = \frac{gT^2}{2\pi}\tanh\left(\frac{2\pi d}{L}\right) \tag{2.10}$$

$$L \approx \frac{gT^2}{2\pi}\sqrt{\tanh\left(\frac{4\pi^2}{T^2}\frac{d}{g}\right)} \tag{2.11}$$

where L and T denote wavelength and wave period, respectively, and d is water depth. Equation (2.10) is an implicit equation in L. Several methods exist for the solution of implicit equations which could be used to solve Equation (2.10), i.e., bisection, iteration of a point, etc. In this case, the Esckart (1952) Equation (2.11) was sued as an initial guess and the iteration of a point method was used to solve Equation (2.10).

Table 2.3 Classification of a water body according to the magnitude of d/L and the resulting limiting values taken by the function tanh(2πd/L) (Source: CERC, 1984)).

Classification	d/L	2πd/L	tanh(2πd/L)
Deep water	> ½	> π	≈ 1
Transitional	1/25 to ½	¼ to π	tanh(2πd/L)
Shallow water	< 1/25	< 1/4	≈ 2πd/L

From the measured AWAC data, the normal peak periods are a 5-second average peak period and 40-second maximum peak period. The wavelengths corresponding to these periods are computed as about 35 m and 340 m, respectively. Based on these data, d/L is calculated as 0.29 and 0.029, respectively. Therefore, the Salton Sea can be classified as ranging through both transitional and shallow water.

Wave generation does not only occur in the direction of the wind, but also at various angles to the wind direction. The energy of waves measured at a particular point is direction dependent (Saville, 1954). Bengtsson et al. (1990) noted that unless the water body is very large and the storm of short duration, the wave conditions are controlled by the wind speed and the fetch and not by the storm duration (Bengtsson et al., 1990; Mian and Yanful, 2004). Calculation of wave characteristics requires fetch conditions of a water body as well as wind conditions. Effective fetch calculation involves the measurement of the fetch distance in the wind direction, and along several directions from a given point from the shore, which is a standard engineering measurement for shore protection studies (Bhowmik, 1975; Hakanson and Jansson, 1983). In mathematical terms:

$$F_e = \frac{\sum(\cos\alpha_i)F_i}{\sum(\cos\alpha_i)} \tag{2.12}$$

where F_e and F_i denote effective fetch and the fetch distance along direction i (km), respectively, and α_i is the angle between the shore normal and the direction i.

In Figure 2.5 examples of effective fetch calculation are shown for the Salton Sea. The locations for effective fetch calculation were chosen according to the closest CIMIS stations for which wind data have already been analyzed. The dominant wind direction was assumed to be from the west. A norm fetch along the main wind direction along with fetches from the norm with the angle α = 6 º, 12 º, 18 º, …, 42 º were used for this estimation. Effective fetches are calculated according to Equation (2.11) to be 25.4 km for CIMIS Station #127 and 30 km for CIMIS Station #128. The fetch of the Salton Sea is assumed to be 30 km in this research.

For a given set of wind and fetch conditions, wave heights and periods can be estimated by a wave forecast model, Sverdrup-Munk-Bretschneider (SMB) method, for transitional or shallow water bodies (CERC, 1984). The SMB model is applied to calculate wave characteristics of the Salton Sea.

(a)

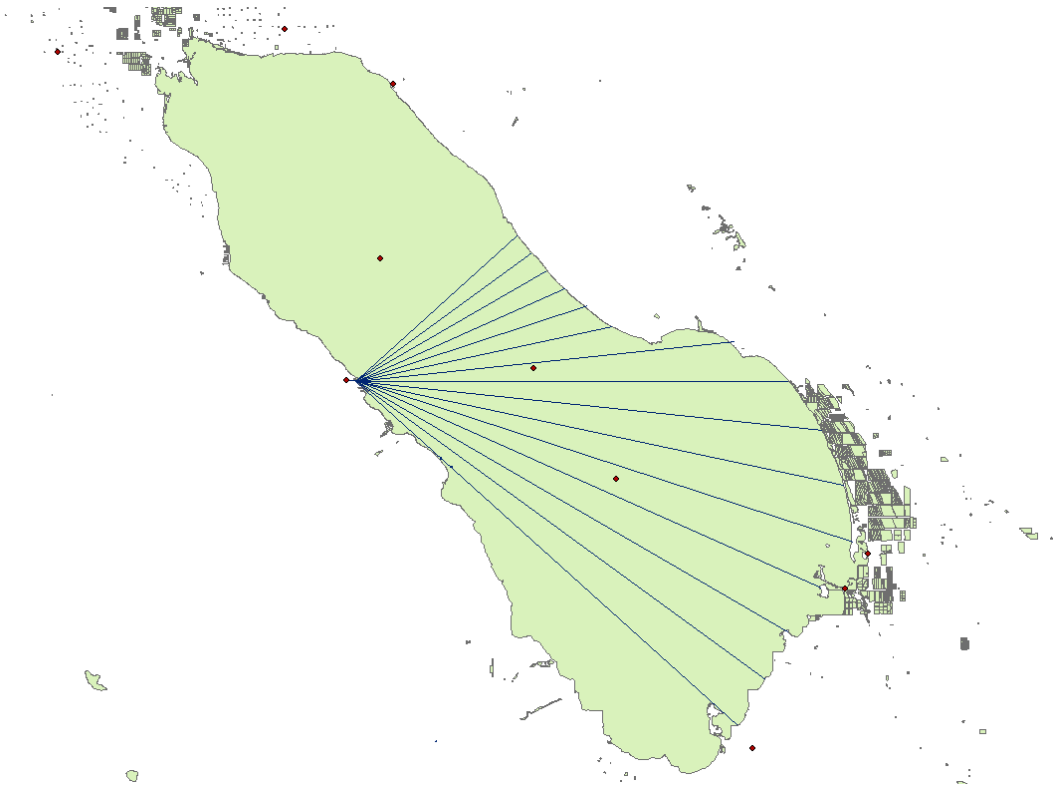

(b)

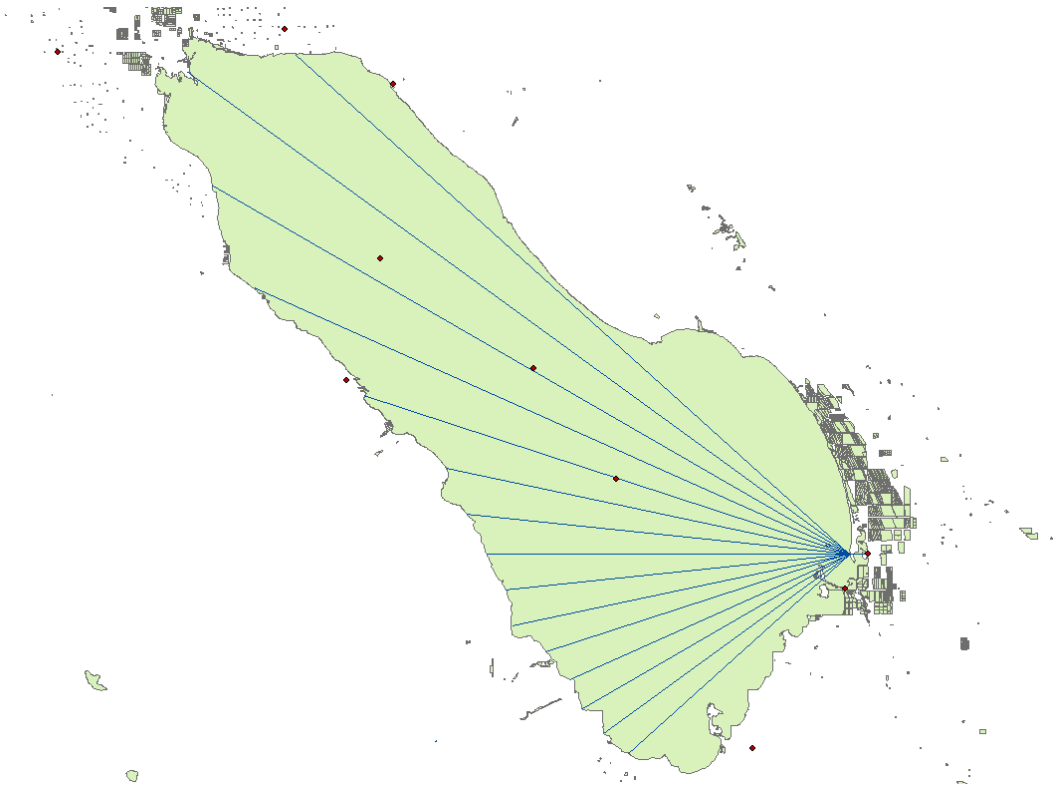

Figure 2.5 Determination of effective fetch of the Salton Sea: (a) from CIMIS station 127; (b) from CIMIS station 128.

$$\frac{gH}{U_A^2} = 0.283 \tanh\left[0.530\left(\frac{gd}{U_A^2}\right)^{3/4}\right] \tanh\left\{\frac{0.00565\left(\frac{gF}{U_A^2}\right)^{1/2}}{\tanh\left[0.530\left(\frac{gd}{U_A^2}\right)^{3/4}\right]}\right\} \tag{2.13}$$

$$\frac{gT}{U_A} = 7.54 \tanh\left[0.833\left(\frac{gd}{U_A^2}\right)^{3/8}\right] \tanh\left\{\frac{0.0379\left(\frac{gF}{U_A^2}\right)^{1/3}}{\tanh\left[0.833\left(\frac{gd}{U_A^2}\right)^{3/8}\right]}\right\} \tag{2.14}$$

$$\frac{gt}{U_A} = 5.37 \cdot 10^2 \left(\frac{gT}{U_A}\right)^{7/3} \tag{2.15}$$

where H is wave height, F is fetch, t is duration and U_A denotes wind-stress factor; $U_A = 0.71 U^{1.23}$.

References

Aalderink, R. H., Lijklema, L., Breukelman, J., Vanraaphorst, W., and Brinkman, A. G. 1985. Quantification of Wind Induced Resuspension in a Shallow Lake. Water Science and Technology **17:** 903-914.

Akiyama, J., and Fukushima, Y. 1986. Entrainment of noncohesive sediment into suspension, p. 804-813. *In* Wang, S. Y., Shen, H. W. and Ding, L. Z. [eds.], 3rd International Symposium on River Sedimentation.

Andersen, M. a. A., C. 2002. Nutrient Cycling in the Salton Sea. Department of Environmental Sciences, UC Riverside.

Anderson, M. 2003. Bioavailability, Resuspension and Control of Sediment-Borne Nutrients in the Salton Sea. Department of Environmental Sciences, UC Riverside.

Arulanandan, K. 1975. Fundamental Aspects of Erosion of Cohesive Soils. Journal of the Hydraulics Division-Asce **101:** 635-639.

Bengtsson, L., Hellstrom, T., and Rakoczi, L. 1990. Redistribution of Sediments in 3 Swedish Lakes. Hydrobiologia **192:** 167-181.

Bhowmik, N. 1975. Development of Criteria for Shore Protection against Wind-Generated Waves for Lakes and Ponds in Illinois. Water Resources Center, University of Illinois

Bloesch, J. 1995. Mechanisms, Measurement and Importance of Sediment Resuspension in Lakes. Marine and Freshwater Research **46:** 295-304.

Bombardelli, F. A., and García, M. H. 1999. Numerical Simulation of Wind-Induced Resuspension of Bed Sediment in Sallow Lakes. International Water Resources Engineering Conference, ASCE.

Carpelan, L. H. 1958. The Salton Sea. Physical and Chemical Characteristics. Limnology and Oceanography **3:** 373-386.

Celik, I., and Rodi, W. 1984. A deposition entrainment model for suspended sediment transport. Universitat Karlsruhe.

CERC. 1984. Shore Protection Manual. US Army Corps of Engineers.

Cook, C. B., Orlob, G. T., and Huston, D. W. 2002. Simulation of wind-driven circulation in the Salton Sea: implications for indigenous ecosystems. Hydrobiologia **473:** 59-75.

Cooper, J. J., and Koch, D. L. 1984. Limnology of a Desertic Terminal Lake, Walker Lake, Nevada, USA. Hydrobiologia **118:** 275-292.

Christensen, B. A. 1965. Discussion of erosion and deposition of cohesive soils (by E. Partheniades). Journal of the Hydraulics Division-Asce **91:** 301-308.

Christensen, B. A., and Das, B. M. 1973. Hydraulic erosion of remolded cohesive soils, p. 8-19. *In* Council, N. R. [ed.], Soil erosion: causes and mechanisms, prevention and control. Highway Research Board

Dietrich, W. E. 1982. Settling Velocity of Natural Particles. Water Resources Research **18:** 1615-1626.

Eistein, H. A. 1950. The bed load function for sediment transportation in open channels. Soil Conservation Service, U.S. Department of Agriculture.

Engelund, F., and Fredsoe, J. 1976. A sediment transport model for straight alluvial channels. Nordic Hydrology **7:** 293-306.

Engelund, F., and Fredsoe, J. 1982. Hydraulic theory of alluvial rivers, p. 187-215. *In* Chow, V. T. [ed.], Advances in hydroscience. Academic Press, Inc.

Fukuda, M. K., and Lick, W. 1980. The Entrainment of Cohesive Sediments in Fresh-Water. Journal of Geophysical Research-Oceans and Atmospheres **85:** 2813-2824.

García, M. 1999. Sedimentation and Erosion Hydraulics. *In* Mays, L. W. [ed.], Hydraulic Design Handbook. McGraw-Hill.

García, M., and Parker, G. 1991. Entrainment of Bed Sediment into Suspension. Journal of Hydraulic Engineering-ASCE **117:** 414-435.

Gloor, M., Wuest, A., and Munnich, M. 1994. Benthic Boundary Mixing and Resuspension Induced by Internal Seiches. Hydrobiologia **284:** 59-68.

Gularte, R. C. 1978. Erosion of cohesive marine sediment as a rate process. Ph.D. dissertation. University of Rhode Island.

Hakanson, L., and Jansson, M. 1983. Principles of Lake Sedimentology. Springer-Verlag.

Hamilton, D. P., and Mitchell, S. F. 1996. An empirical model for sediment resuspension in shallow lakes. Hydrobiologia **317:** 209-220.

Hamilton, D. P., and Mitchell, S. F. 1997. Wave-induced shear stresses, plant nutrients and chlorophyll in seven shallow lakes. Freshwater Biology **38:** 159-168.

Hawley, N., and Lesht, B. M. 1992. Sediment Resuspension in Lake St-Clair. Limnology and Oceanography **37:** 1720-1737.

Hawley, N., Lesht, B. M., and Schwab, D. J. 2004. A comparison of observed and modeled surface waves in southern Lake Michigan and the implications for models of sediment resuspension. Journal of Geophysical Research-Oceans **109**.

Itakura, T., and Kishi, T. 1980. Open Channel Flow with Suspended Sediments. Journal of the Hydraulics Division-Asce **106:** 1325-1343.

Jin, K. R., and Wang, K. H. 1998. Wind generated waves in Lake Okeechobee. Journal of the American Water Resources Association **34:** 1099-1108.

Julien, P. 1998. Erosion and Sedimentation. Cambridge University Press.

Kandiah, A. 1974. Fundamental aspects of surface erosion of cohesive soils. Ph.D. dissertation. University of California, Davis.

Krone, R. B. 1962. Flume studies of the transport of sediment in estuarial shoaling processes, p. 118. Hydraulic Engineering Laboratory. and Sanitary Engineering Research Laboratory, University of California, Berkeley.

Lambermont, J., and Lebon, G. 1978. Erosion of cohesive soils. Journal of Hydraulic Research **16:** 27-44.

Luettich, R. A., Harleman, D. R. F., and Somlyody, L. 1990. Dynamic Behavior of Suspended Sediment Concentrations in a Shallow Lake Perturbed by Episodic Wind Events. Limnology and Oceanography **35:** 1050-1067.

Mehta, A. J. 1981. Review of erosion function for cohesive sediment beds, p. 122-130. First Indian Conference on Ocean Engineering.

Mehta, A. J., Parchure, T. M., Dixit, J. G., and Ariathurai, R. 1982. Resuspension Potential of Deposited Cohesive Sediment Beds. Academic Press.

Mian, M. H., and Yanful, E. K. 2004. Analysis of wind-driven resuspension of metal mine sludge in a tailings pond. Journal of Environmental Engineering and Science **3:** 119-135.

Neill, C. R. 1968. A reexamination of the beginning of movement for coarse granular bed materials. Hydraulics Research Station.

Parker, G., Toro-Escobar, C. M., Ramey, M. A., and Beck, S. 2003. The effect of floodwater extraction on the morphology of mountain streams. Journal of Hydraulic Engineering-ASCE **129:** 885-895.

Parker, G. 2004. 1D Sediment Transport Morphodynamics with applications to Rivers and Turbidity currents. http://cee.uiuc.edu/people/parkerg/.

Partheniades, E. 1962. A study of erosin and deposition of cohesive soils in salt water. Ph.D. dissertation. University of California, Berkeley.

Poisson, A., Gadhoumi, M. H., and Morcos, S. 1991. Salinity and density of seawater: Tables for high salinities (42 to 50).

Ponce, V. THE SALTON SEA: AN ASSESSMENT http://saltonsea.sdsu.edu/.

Raudkivi, A. J. 1990. Loose Boundary Hydraulics, 3rd edition ed. Pergamon Press.

Raudkivi, A. J., and Hutchison, D. L. 1974. Erosion of kaolinite by flowing water, p. 537-554. Proceedings of the Royal Society of London. Series A.

SaltonSeaAuthority. 2000. Sea Geography. http://www.saltonsea.ca.gov/geography.htm.

Sanford, L. P., and Maa, J. P. Y. 2001. A unified erosion formulation for fine sediments. Marine Geology **179:** 9-23.

Saville, T. 1954. The effect of fetch width on wave generation. U.S. Beach Erosion Board.

Scheidlinger, C., Kulpa, J., Crooks, S., Montano, J., Webb, B., and Chesnut, J. 2003. Characterization of Shallow Sub-Surface Sediment of the Salton Sea. Agrarian Research.

Schladow, S. G., Robertson, D. M., Hook, S. J., Chung, E. G., Losada, J. P., Cardona, B. M., Palmarsson, S. O., Steissberg, T. E., and Fleenor, W. E. 2004. Salton Sea Nutrients TMDL Modeling Studies. Colorado River Basin Regional Water Quality Control Board.

Sheng, Y. P., and Lick, W. 1979. Transport and Resuspension of Sediments in a Shallow Lake. Journal of Geophysical Research-Oceans and Atmospheres **84:** 1809-1826.

Shields, A. F. (1936), Anwendung der aehnlichkeitsmechanik und der turbulenzforschung auf die geschiebebewegung, Ph.D. dissertation, Mitt. Preuss Ver.-Anst., Berlin, Germany (in German), (English translation by W. P. Ott and J. C. van Uchelen available as Hydrodynamics Laboratory Publication No. 167, Hydrodynamics Lab., California Inst. of Tech., Pasadena).

Shteinman, B., Eckert, W., Kaganowsky, S., and Zohary, T. 1997. Seiche-induced resuspension in Lake Kinneret: A fluorescent tracer experiment. Water Air and Soil Pollution **99:** 123-131.

Smith, J. D., and McLean, S. R. 1977. Spatially Averaged Flow over a Wavy Surface. Journal of Geophysical Research-Oceans and Atmospheres **82:** 1735-1746.

Somlyòdy, L. 1981. Modeling a complex environmental system: The Lake Balaton Study., p. 14-19. International Institute for Applied System Analysis.

Somlyòdy, L. 1986. Wind induced sediment resuspension in shallow lakes, p. 287-298. *In* Bhra, T. F. E. C. [ed.], Water Quality Modelling in the Inland Natural Environmnet. BHRA, The Fluid Engineering Centre.

Thorn, M. F. C., and Parsons, J. G. 1980. Erosion of cohesive sediments in estuaries: An engineering guide, p. 349-358. *In* Stephens, H. S. [ed.], 3rd International Symposium on Dredging Technology, BHRA.

Van Rijn, L. C. 1984. Sediment Transport .2. Suspended-Load Transport. Journal of Hydraulic Engineering-ASCE **110:** 1613-1641.

Watts, J. M., Swan, B. K., Tiffany, M. A., and Hurlbert, S. H. 2001. Thermal, mixing, and oxygen regimes of the Salton Sea, California, 1997-1999. Hydrobiologia **466:** 159-176.

Yeh, H. Y. 1979. Resuspension properties of flow deposited cohesive sediment beds. M.S. Thesis. University of Florida.

Zyserman, J. A., and Fredsoe, J. 1994. Data-Analysis of Bed Concentration of Suspended Sediment. Journal of Hydraulic Engineering-ASCE **120:** 1021-1042.

CHAPTER 3: CHAPTER 3. DATA ANALYSIS AND COMPUTATION OF SEDIMENT RESUSPENSION

LOCATIONS OF FIELD OBSERVATIONS

Numerous field studies have been undertaken to observe the hydrodynamics and sediment resuspension in lakes around the world. In some studies, only lake currents have been characterized (Gloor et al., 1994); in other studies, only lake waves have been considered (Freire and Andrade, 1999; Hamilton and Mitchell, 1996; Hawley et al., 2004; Mian and Yanful, 2004; Sheng and Lick, 1979); in other studies, data on both currents and waves have been observed (Luettich et al., 1990; Osborne and Greenwood, 1993). The present set of observations differs from previous field campaigns in that a comprehensive set of variables have been simultaneously and continuously monitored in the Salton Sea for a relatively-long period; in addition, this work reports one of the first studies undertaken with an acoustic wave and current profiler, AWAC, in lakes.

The fundamental data set was obtained from four main sources including YSI 6-Series instruments from three "sediment" observation stations for turbidity, which we used herein as a surrogate of suspended sediment concentration, a Nortek AWAC for wave characteristics and water currents, thermistor chains for water temperature, and the local CIMIS stations for meteorological data. These main instruments including YSI 6-Series, AWAC and one of thermistor chains (E2) were located toward the eastern shore of the Salton Sea as shown in Figure 3.1 (a). The location was chosen because the southern and eastern side shores of the Sea are particularly prone to sediment resuspension due to strong winds out of the west-southwest, Anderson (2003).

The sediment observation stations were installed with YSI instruments at water depths of 4 m, 6 m, and 8 m respectively, as shown in Figure 3.1 (a) and (b), from August 4, 2005 to September 26, 2005. Each station comprised a YSI instrument 0.5 m off the bottom, and the middle station located in a water depth of 6m had another YSI instrument 5 m off the bottom. The YSI instruments recorded turbidity through optical backscatter (OBS), dissolved oxygen (DO), water temperature, pressure (water depth), and specific conductivity. The sensors were synchronized using GPS time, set to record at 15 minute intervals for 70 days. The resolution and time frame allowed the effect of wind waves on the lake bed to be well quantified both spatially and temporally. Data from YSI 6-Series were retrieved and processed using ECOWW (version 3.17) software provided by the instrument company.

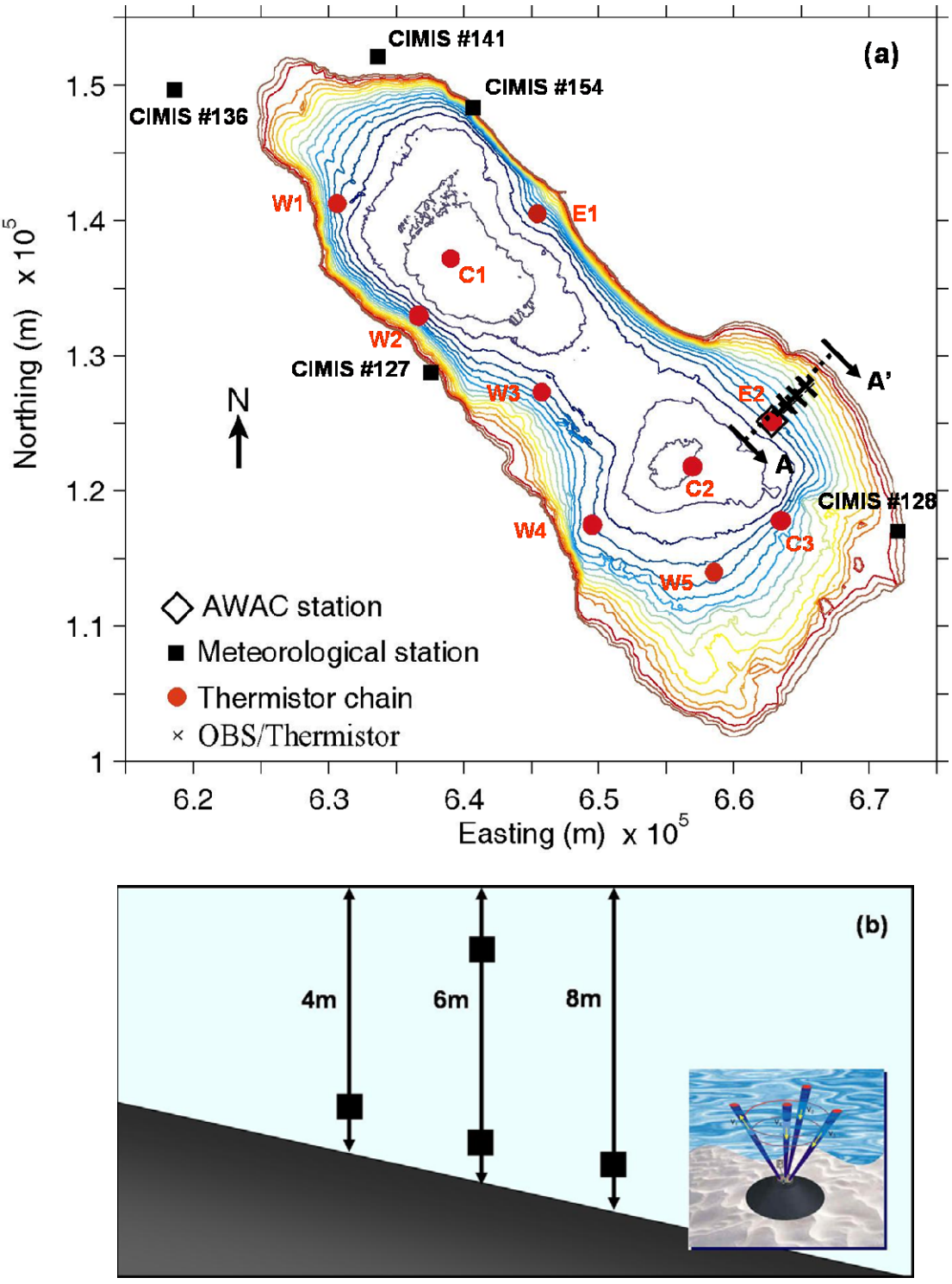

Figure 3.1 Location of sampling stations and bathymetry of the Salton Sea: (a) Bathymetry showing depth contours (at 1 m intervals). Red circles are location of UC Davis thermistor chains; black squares are locations of CIMIS meteorological stations; crosses are the locations of the OBS stations; (b) schematic side view of section A-A' including installation of YSI instruments.

The turbidity measurements of the OBS on the YSI instrument are used as a surrogate of suspended sediment concentration. The OBS sensor incorporates a wiper blade to avoid biofouling and barnacle growth. The use of two OBS sensors installed at the 6m Sea depth at 1 m from the bottom and 1 m from the top provided information on the vertical extent of the sediment resuspension. The OBS was paired with temperature data to provide simultaneous information about the strength of the temperature stratification.

A Nortek AWAC was also deployed. The AWAC is a newly developed instrument that can provide continuous profiles of both current speed and direction (at 0.75 m increments) along with wave height, period and direction. Each of these data types is extremely important to developing a model that correctly represents the main mechanisms behind sediment resuspension. In addition, the "signal strength" at each measurement bin can be used as a surrogate for suspended sediment in the water column, thus providing an almost continuous measure of vertical sediment distribution at one station.

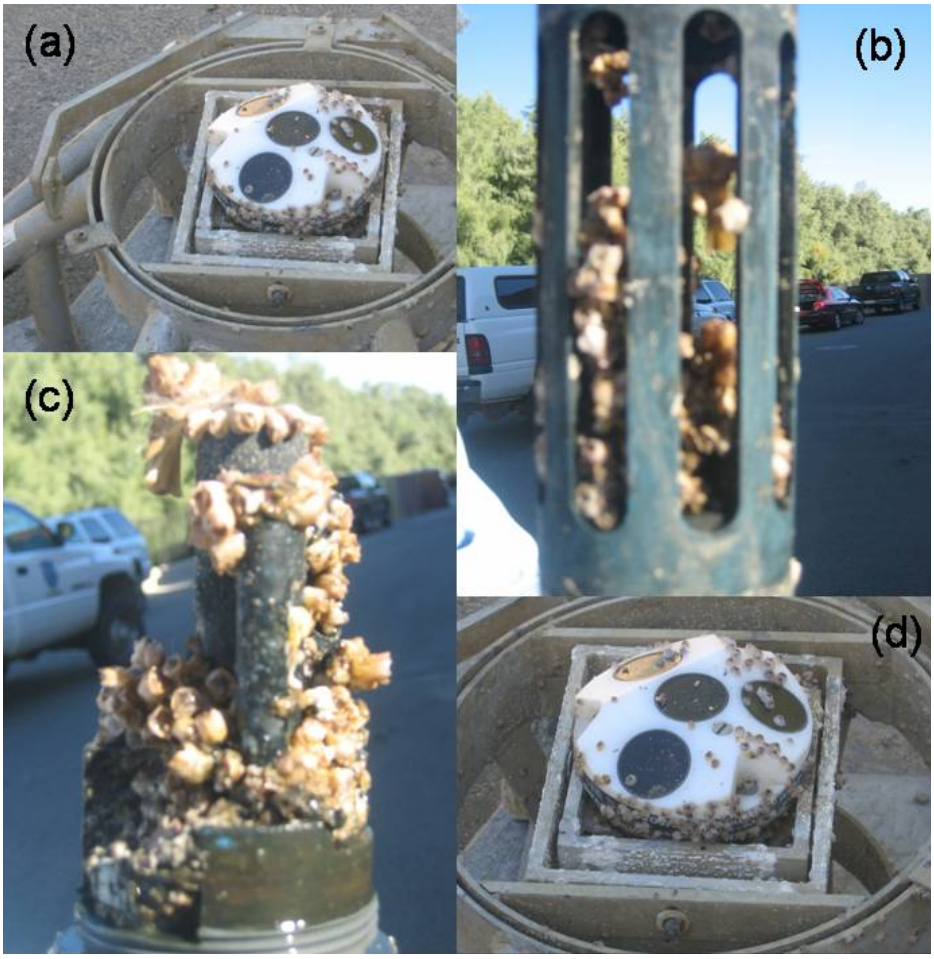

Figure 3.2 AWAC and YSI instruments with barnacle growth right after removing from stations. (a) AWAC mounted in a frame; (b) YSI instrument with a cap; (c) YSI instrument without cap; (d) AWAC.

The Nortek AWAC instrument was co-located with one of the 10 thermistor chains (E2) that UC Davis installed in the Sea, as shown in Figures 3.1 (a). The AWAC was also synchronized using GPS time. AWAC sampled at frequencies of 7 Hz for wave characteristics and 4.34 Hz for currents, respectively, from August 4, 2005 to November 29, 2005. The data sampled at these frequencies were averaged and recorded at 30- and 10-minute intervals for waves and currents, respectively, to extend battery duration and memory storage. The instrument mounting frame and the "blanking distance" (where the velocity profile is lost while the system recovers from acoustic transmission) precluded velocity measurements in the first 1.8 m above the bottom (Nortek, 2004). STORM (version 1.05), a software provided by Nortek, was used for retrieving and processing AWAC data. The extent of barnacle growth (see Figure 3.2) on instruments is significant in spite of the preventative measures taken.

Figure 3.3 Locations of thermistor chains in the Salton Sea.

The thermistor chains were installed as a part of the nutrient TMDL research of the Salton Sea (Schladow et al., 2004). Each thermistor chain had either 8 or 10 temperature loggers depending on the elevation of the Sea, and provided a continuous record of the water temperature providing a status of stratification of the Sea. The instruments were deployed for 4 months, and cleaned and downloaded after 2 months as biofouling was a major issue. The thermistor chains were installed in August 2005, and the geographical location of the thermistor chains in the Sea is shown in Figure 3.3.

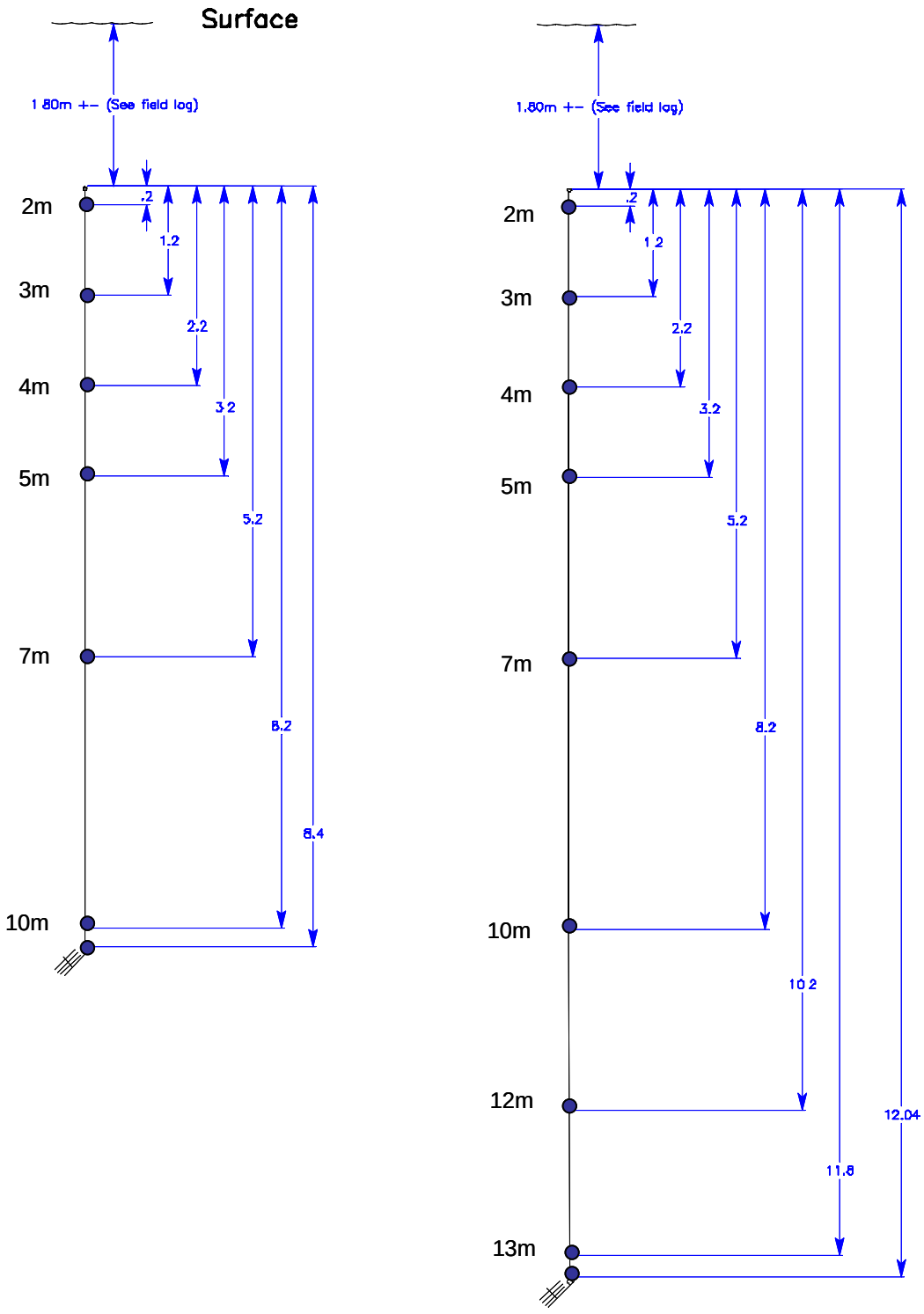

Figure 3.3 Thermistor depths (in meters) of the long and short thermistor chains. Two thermistor chain designs were used. A deep water (nominally 14 m) design was used for the sites C1 and C2. A shallow water design (nominally 10.2 m) was used for the remainder of the sites.

Locations were chosen to provide 3 lines of thermistor chains – one on the west side of the Sea (Sites W1-W5), one down the center of the Sea (C1-C3), and one down the east side of the Sea (E1-E2). The thermistor chains were constructed of ¼'' stainless steel wire rope with a 150 lb anchor at the bottom. The thermistors were secured onto the wire rope by stainless steel wire. Heavy pipe tape was wrapped around each thermistor to prevent encrustation by barnacles. A stainless steel T-bar supported by two sub-surface buoys was used to provide a means for manually grappling for the chain if the surface marker was lost. A solid bar from the T-bar was attached to a surface marker float (Schladow et al., 2004). The design depths of the thermistor chains are given in Figure 3.4.

Meteorological data were obtained from CIMIS stations surrounding the lake. Figure 3.1 (a) shows locations of CIMIS meteorological stations in the vicinity of Salton Sea. Data for this research were obtained from the two closest stations, numbered 127 and 128. Station 127 (33.327 ºN, 115.95 ºW) is located in Imperial County, near Salton City, and Station 128 (33.22 ºN, 115.58 ºW) is located in Imperial County, near Niland. Solar radiation (Q_s), air temperature (T_a), relative humidity (RH), and wind speed (w_S) and direction (w_D) were recorded at 1-hour intervals, and daily data were provided as well. Wind data, in particular, among the meteorological data were crucial to quantify sediment resuspension. Wind speed and direction were measured using three-cup anemometers and a wind vane, respectively, at 2.0 meters above the ground. Wind direction values range from zero to 360 degrees (both being true north) in the clockwise direction.

Table 3.1 Period and frequency of data sampling

Instrument/ Data Sources	Measurement Data	Period	Frequency
OBS	Temperature Turbidity Conductivity DO	08/08/2005 – 09/26/2005	15 min.
AWAC	Wave height Peak period	08/04/2005 – 11/29/2005	30 min.
	Current intensity and direction		10 min.
Thermistor Chains	Water temperature	08/04/2005 – 11/25/2005	10 min.
CIMIS	Air temperature Wind speed Wind direction	08/04/2005 – 11/29/2005	hourly

DATA ANALYSIS

The time series data, including wind data, water temperature data, YSI instrument data, and AWAC data obtained from the four main sources described in the preceding section, are presented and analyzed in this section.

Wind data

Meteorological data were obtained from CIMIS Station 127 and 128. Since wind events are the main driving force for sediment resuspension in shallow lakes, wind data of these two stations were analyzed as eastern (U) and northern components (V) from August 4, 2005 to November 29, 2005 (Figure 3.5 (a) and (b)). Nine years of wind data are shown in Figures 3.5 (c) and (d) from Station 127 and 128 from 1997 to 2005, to compare the wind data set during this research period with long-term wind characteristics. Station 127 had a dominant component along the centerline of the Sea as well as a western component, Figure 3.5 (a) and (c). Station 128 has a stronger primary western component with a minor component along the centerline of the Sea Figure 3.5 (b) and (d). The difference between primary components of two stations likely produce a rotation, such as a gyre, in the wind field, as well as the gyres in the southern part of the Sea currents which are occasionally observed and simulated by modeling (Cook et al., 2002).

Relative frequency of hourly wind data from Station 127 and 128 from August 4, 2005 to November 29, 2005, respectively, are shown in Figures 3.6 (a) and (b). The most frequent wind speed is around 1.5 m s^{-1} at both stations for this period. Figures 3.6 (c) and (d) also show relative frequency of hourly wind data of the same two stations from year 1997 to year 2005 providing a comparison of wind data sets obtained during this research with a longer term data set. The most frequent wind speed, 1.5 m s^{-1}, is consistent for both stations. However, the relative frequency of the dominant wind speeds of the long term data set is different than that of short term data set.

Wind data at Station 127 showed similar wind speed patterns for both the short and long term data set. For example, wind speeds above 2 m s^{-1} were 54.2 % for year 2005 data and 53.0 % for nine year's of data; those above 5 m s^{-1} were 4.3 % and 4.7 %, and those above 8.5 m $^{-1}$s were 0.2 % and 0.3 %, respectively. However, wind data at Station 128 indicated that the long term data had a greater frequency of higher wind speeds than occurred in year 2005 data. For instance, wind speeds above 2 m s^{-1} were 36.7 % for year 2005 data while 42.5 % for nine year data; those above 5 m s^{-1} were 5.2 % and 9.4 %, and those above 8.5 m s^{-1} were 0.6 % and 2.9 %, respectively. In addition, long term data at Station 128 had greater frequencies of higher wind speeds than those at Station 127.

Time series of hourly meteorological data, including air temperature (ºC), wind speed (m s^{-1}) and wind direction (degree), from CIMIS Stations 127 and 128 are shown in Figure 3.7. Air temperature ranged daily by about 10 ºC almost throughout the whole

research period. The average temperature was around 35 ºC from day 216 to 240, it decreased from 35 ºC to around 25 ºC starting day 256, and varied in a range between 30ºC and 25ºC from day 256 to day 290.

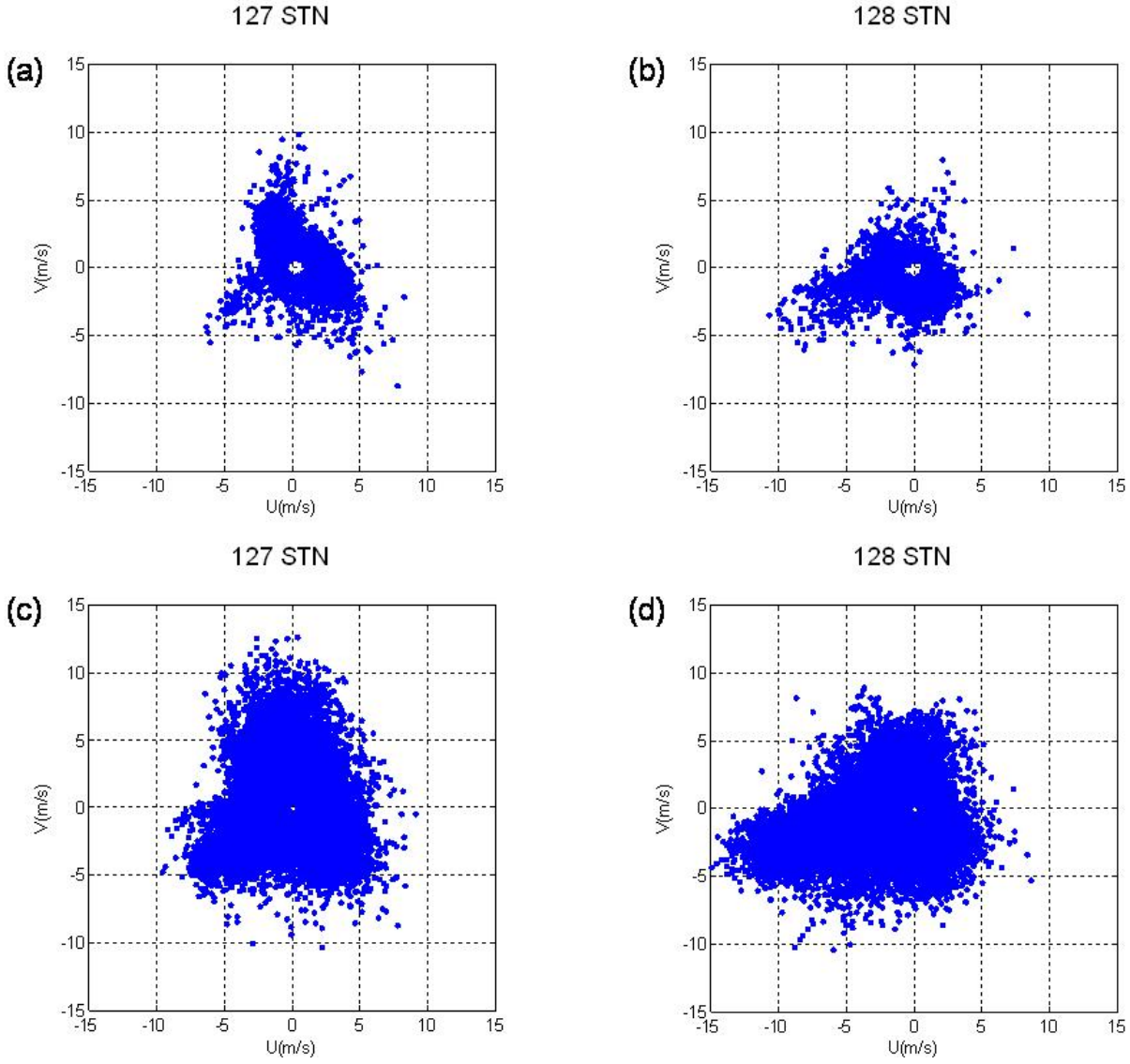

Figure 3.5 Wind components of hourly wind data. U (m s^{-1}) is eastern component and V (m s^{-1}) is northern component: (a) CIMIS Station 127 from August 4, 2005 to November 29, 2005; (b) CIMIS Station 128 from August 4, 2005 to November 29, 2005; (c) CIMIS Station 127 from year 1997 to year 2005; (d) CIMIS Station 128 from year 1997 to year 2005.

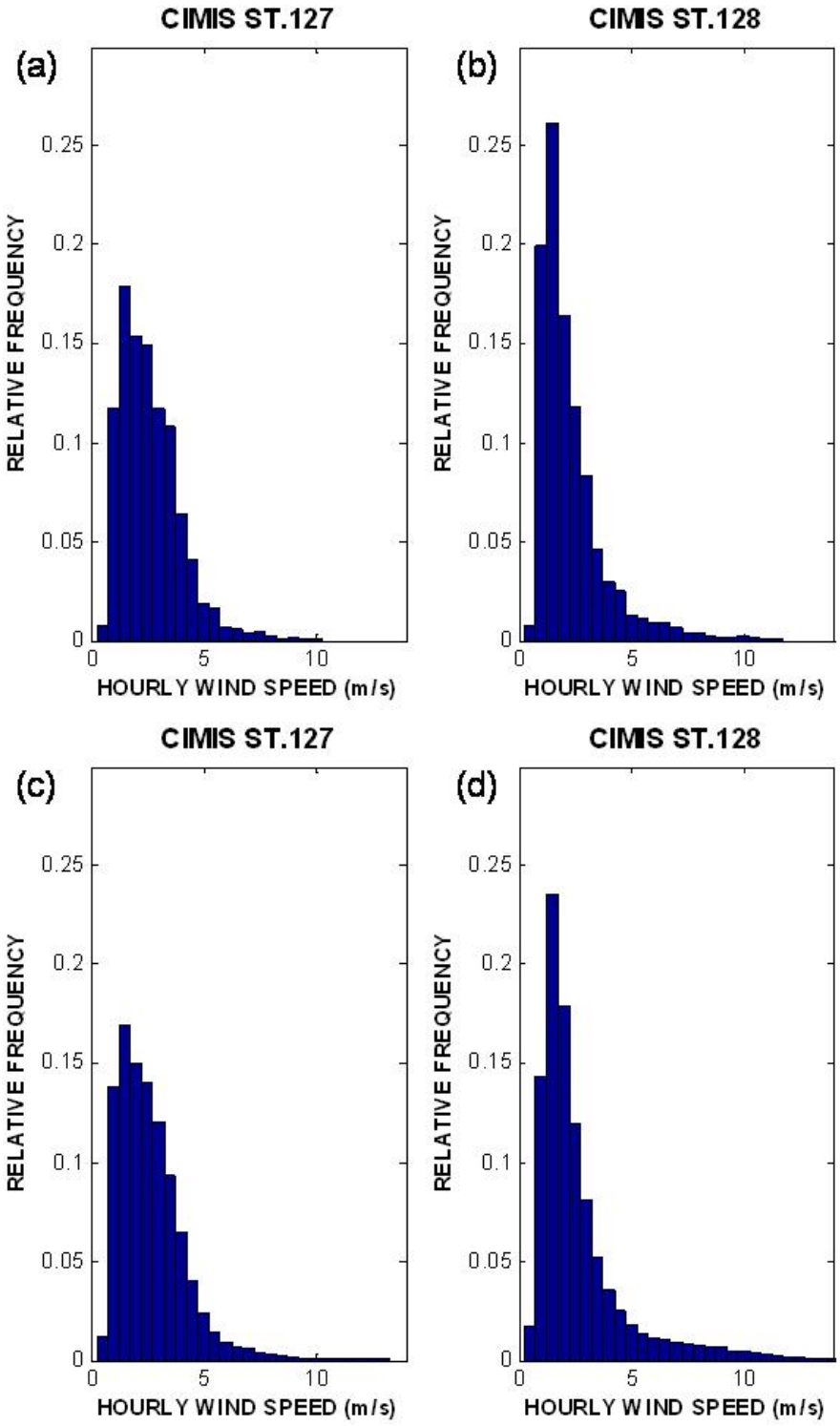

Figure 3.4 Relative frequency of hourly wind data: (a) CIMIS Station 127 from August 4, 2005 to November 29, 2005; (b) CIMIS Station 128 from August 4, 2005 to November 29, 2005; (c) CIMIS Station 127 from year 1997 to year 2005; (d) CIMIS Station 128 from year 1997 to year 2005.

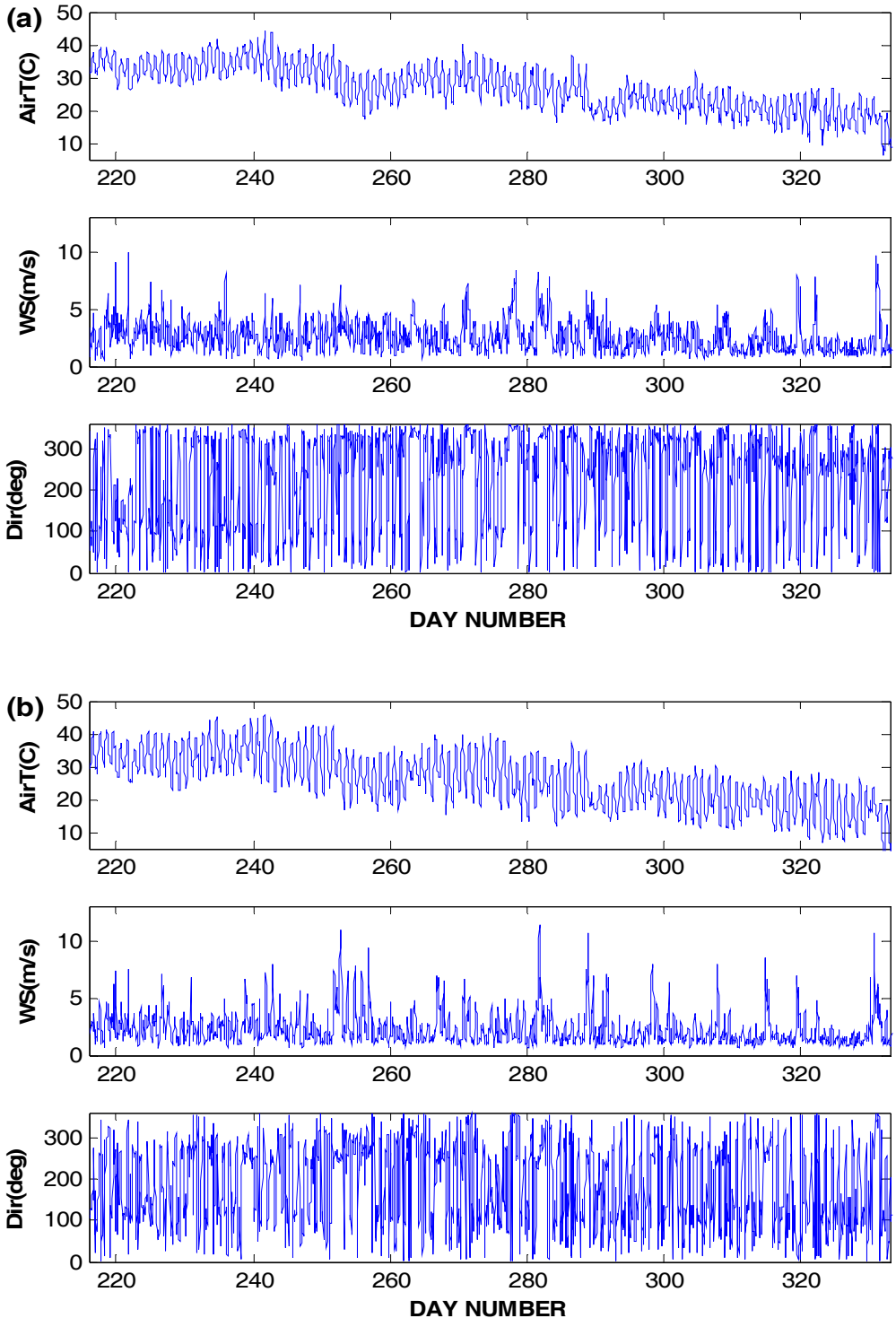

Figure 3.5 Hourly meteorological data for air temperature (ºC), wind speed (m s^{-1}), wind direction (degrees from N) from August, 4, 2005 to November 29, 2005: (a) CIMIS Station 127; (b) CIMIS Station 128.

Strong wind storms were not observed for the recent research observation period shown in Figure 3.7, however, there are several wind events above 10 m s^{-1} in this period. Maximum wind speed was about 12 m s^{-1} and wind speeds above 10 m s^{-1} were observed at days 252 – 253, at days 281 – 283, at around day 290, and at day 311 – 312 at Station 128. The first and second events have a consistent wind direction from the west.

Thermistor chain data

Vertical profiles of water temperature were used to assess the condition of vertical mixing or stratification in the lake, which has an impact on sediment entrainment and transport. For example, stratification can constrain sediment resuspension in lakes. elevation time contours of temperature data obtained from seven thermistor chains from August 4, 2005 to November 25, 2005, including Station W1, W2, W3, W5, C2, E1 and E2 are presented in Figure 3.8. Station locations are shown in Figure 3.1 (a) and 3.3. The water temperature data from the other three stations were not available because the stations were not recovered. Water temperatures through most of the vertical water column exceeded 30ºC from August until early September. Weak stratification at the surface was frequently observed at almost all the stations. Often the whole water column was well mixed, such as shown around days 248 – 250 and 288 – 291. Well-mixed conditions were more often observed at stations located in shallow areas; while stratification was more consistently observed in the deepest part of the Sea (C2). Stratification was particularly prevalent at the bottom, as was observed for days 220 – 240 (see Figure 3.8). These findings agree with the previous work by Holdren and Montaño (2002), who found that the Sea is well mixed during the spring and fall months.

Temperature differences ($\Delta T = T_{lower} - T_{upper}$) between each thermistor on the chain and the upper-most thermistor from days 220 to 260 are shown in Figure 3.9. The depths of loggers located in the thermistor chains are shown in Figure 3.4. Positive ΔT indicates an inverse temperature gradient (i.e. temperature increasing with depth) (Schladow et al., 2004). This inverse temperature gradient rarely occurs, for example at Station W1 at day 222, at Station E1 at days 258 – 260, and at Station E2 at days 252, 253, 256 – 257. Negative ΔT was dominant, suggesting the Sea was hydrostatically stable.

Obviously, the well mixed conditions of the Sea during the observation period significantly facilitate the analysis of sediment resuspension. Stratification of the Station E2, especially where sediment observation stations were installed, was not strong enough to prevent sediment resuspension induced by wind.

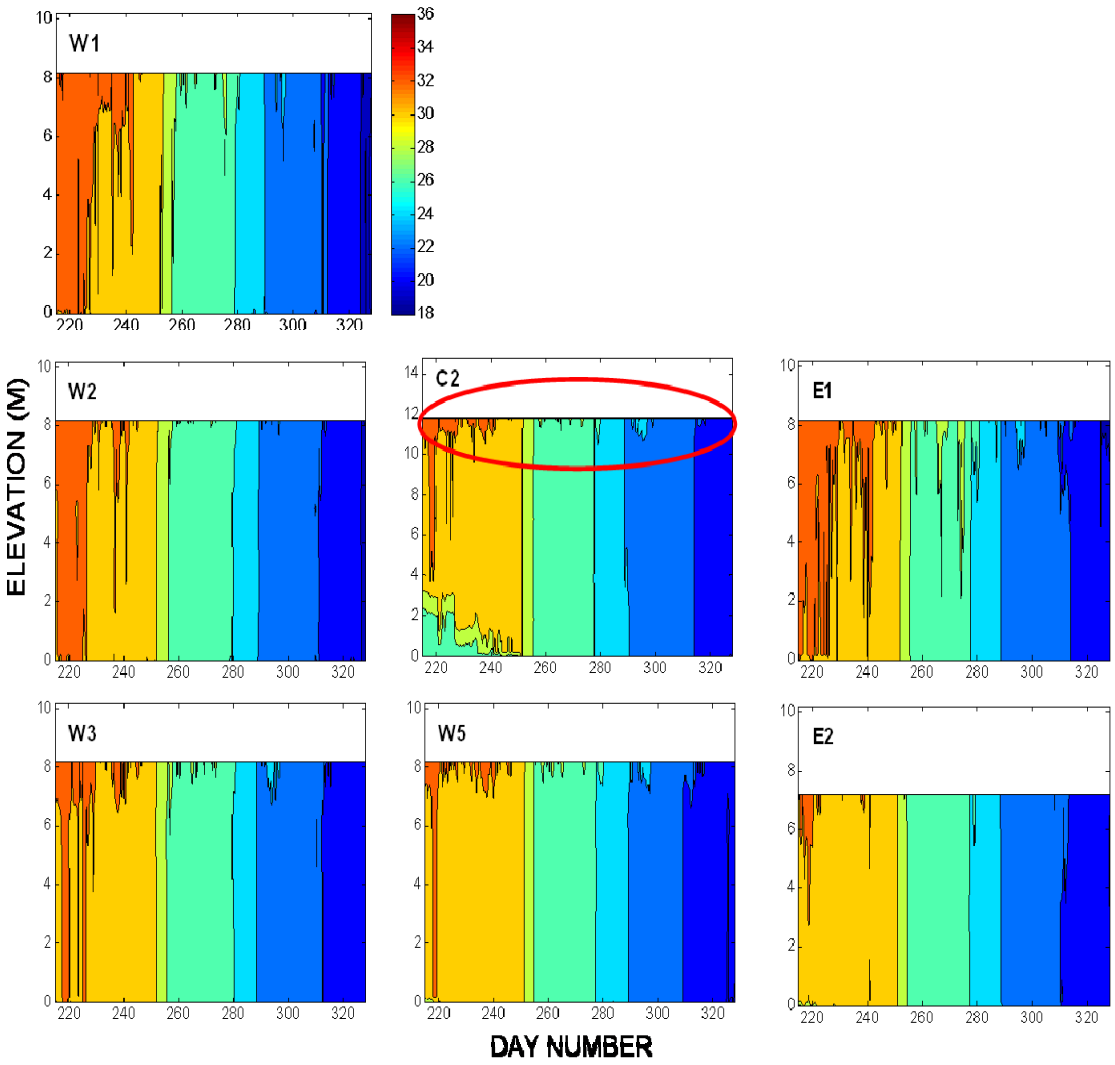

Figure 3.6 Elevation time contours of temperature data from August 4, 2005 to November 25, 2005: (a) Station W1; (b) Station W2; (c) Station C2; (d) Station E1; (e) Station W3; (f) Station W5; (g) Station E2.

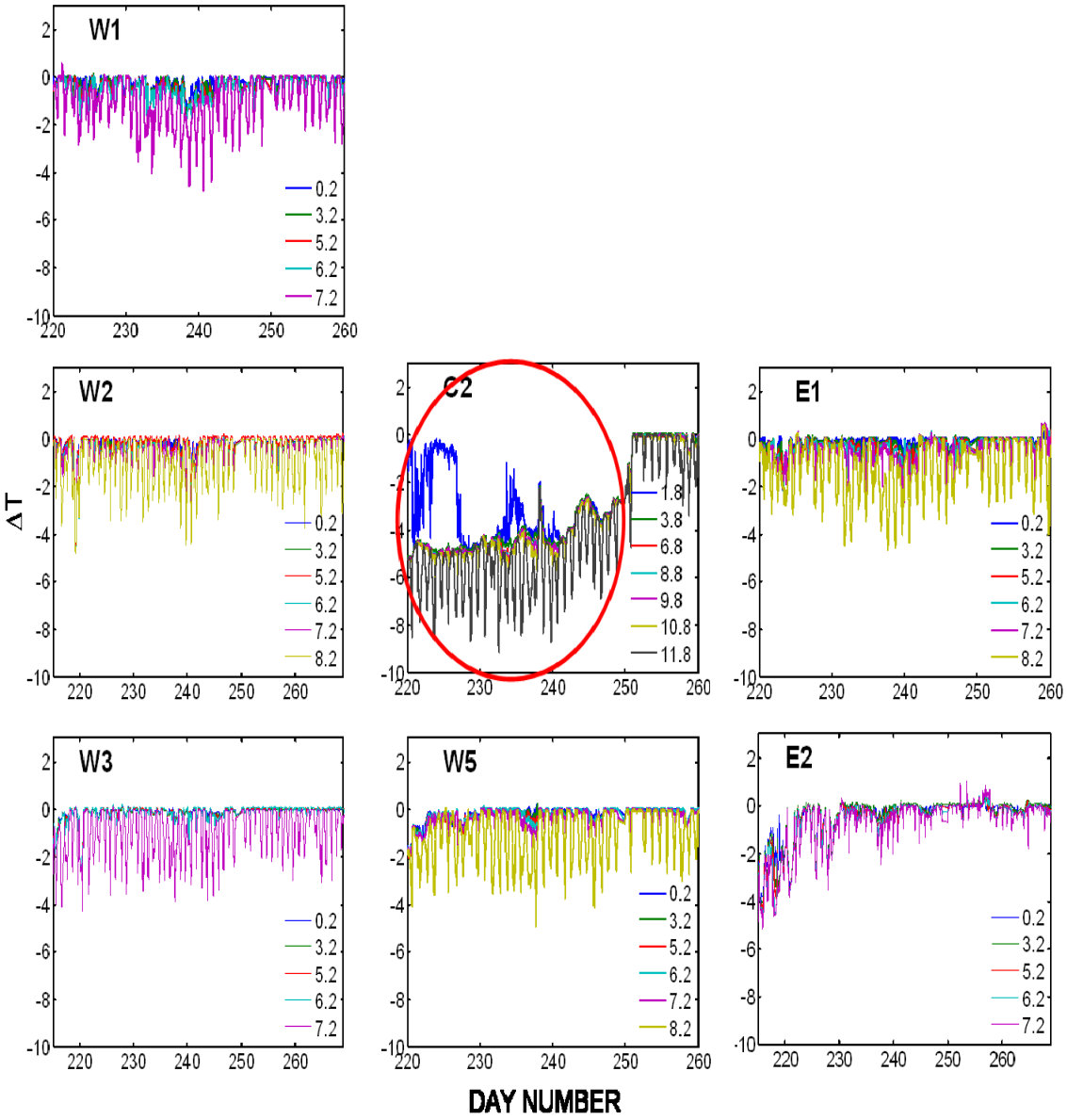

Figure 3.9 Temperature differences ($\Delta T = T_{lower} - T_{upper}$, ºC) between each thermistor in the chain and the upper-most thermistor chain. Negative ΔT suggests lower temperature with increasing depth. Positive ΔT indicates an inverse temperature gradient.

YSI instrument data

The data from four YSI instruments included water temperature, specific conductivity, dissolved oxygen (DO), and turbidity (OBS). The data were collected at three stations from August 4, 2005 to September 26, 2005. The four water temperature data sets at Stations 4 m, 6 m upper and bottom, and 8 m are compared with air temperature of CIMIS Station 128 in Figure 3.10. Analysis of the figure shows that the

Salton Sea was weakly stratified until day 225, but after that day the water columns were well mixed. In addition, temperature abruptly dropped after around day 250 from 31 ºC to 28 ºC, and then further decreased to around 25 ºC; finally, there is a small increase up to 28 ºC. These temperature changes are dominantly influenced by meteorological variations, since no indication of upwelling is noticed in Figure 3.9.

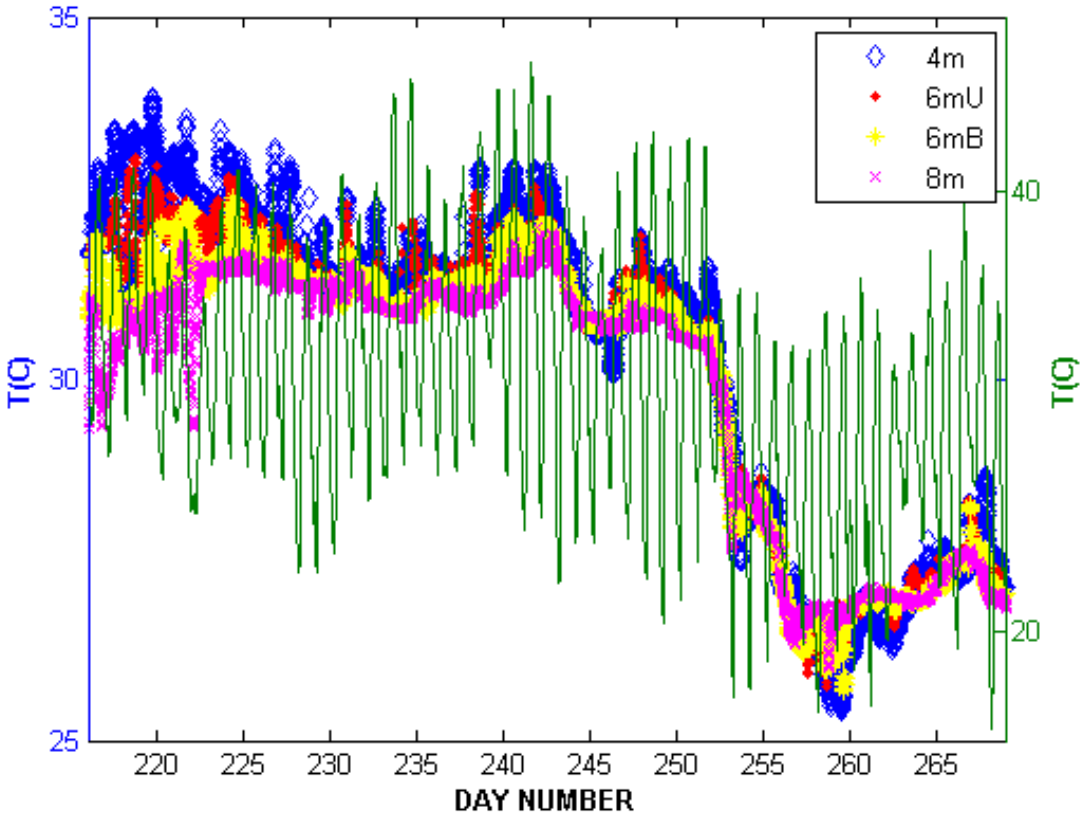

Figure 3.7 Comparison of the water temperature data at sediment observation stations to air temperature of CIMIS Station 128 from August 4, 2005 to September 26, 2005. Water temperature and air temperature of CIMIS station 128 are displayed on the left (blue) and on the right (green) of y-axes, respectively.

Time series of specific conductivity, DO, and turbidity at the three sediment observation stations are shown in Figure 3.11. Also included is hourly wind speed (m s^{-1}) and wind direction (degree) at CIMIS Station 128. These data are presented in a reduced time frame extending from August 8, 2005 to September 17, 2005 (days 220-260), due to the uncertainty of some of the data. Only in this period were specific conductivity values within reasonable ranges. The unusual values are attributed to fouling by barnacle growth inside the instruments as shown in Figure 3.2. Specific conductivity at all stations was stable; however, the values at the three stations are different. For example, specific conductivity during the observation period was about 80 µS cm^{-1} at Station 4 m, while at both 6 m Stations was about 70 µS cm^{-1} and at Station 8 m was about 65 µS cm^{-1}.

Peaks were observed in DO concentrations at Station 4 m on days 233–235, and at Station 6 m upper on days 233–238 in Figure 3.11 (a) and (b), respectively. These peaks might be caused by production from phytoplankton. However, this could not be tested, since no measurement of phytoplankton was performed in this research. DO concentrations at Station 6 m bottom and Station 8 m are not reliable, probably since high hydrogen sulfide concentrations at the bottom of the Sea ”poisoned” the DO probes on the YSI instruments.

Peaks in turbidity at all three stations can be seen in Figure 3.11. Peaks were observed at Station 4 m at days 253–237, at Station 6 m upper at day 253, at Station 6 m bottom at days 242–245, 247–254, at Station 8 m at days 235–254. Comparing two OBS sensors at Stations 6 m upper and bottom, the suspended sediment extended to the surface only at high entrainment intensity events, such as on day 253. However, turbidity values were often observed over 1000 NTU, especially, at Station 8 m. These unduly high values are assumed to be due to malfunction of the wiper blade assembly. These values are much higher than those observed in 1999 by Holdren and Montaño (2002), in which the highest value of turbidity observed in the Salton Sea was 479 NTU. In examining turbidity of other water bodies, the turbidity of eleven saline lakes in Australia ranged from 1 NTU to 310 NTU (Dedeckker and Williams, 1988). Turbidity in six wetlands, south-western Australia ranged from 0.9 NTU to 241.5 NTU between September, 2002 to February, 2004 (Strehlow et al., 2005). If the turbidity is greater than 10 NTU, a wetland is classified as turbid by the Australian and New Zealand Environment and Conservation Council (ANZECC) (2001). Furthermore, turbidity due to inorganic silt particles in Rhenosterkop Dam, KwaNdebele, South Africa ranged only from 10.9 to 52.8 NTU (Robarts et al., 1992). Therefore, values of turbidity larger than 500 NTU were disregarded.

The analysis of the time series reveals that the existence of peaks in wind intensity is associated with peaks in turbidity. These peaks of hourly wind speed seem to occur with quasi-invariant wave direction from the west. Red circles in Figure 3.11 indicate that high wind speed and persistent wind direction could cause high turbidity. The same relation is also shown between all turbidity data (NTU), wind speed (m s^{-1}) and wind direction (degree) plotted from September 8, 2005 to September 15, 2005 in Figure 3.12. Examination of Figure 3.12 indicates that peaks in turbidity are in phase with peaks in wind intensity and quasi-constant wind direction from the west.

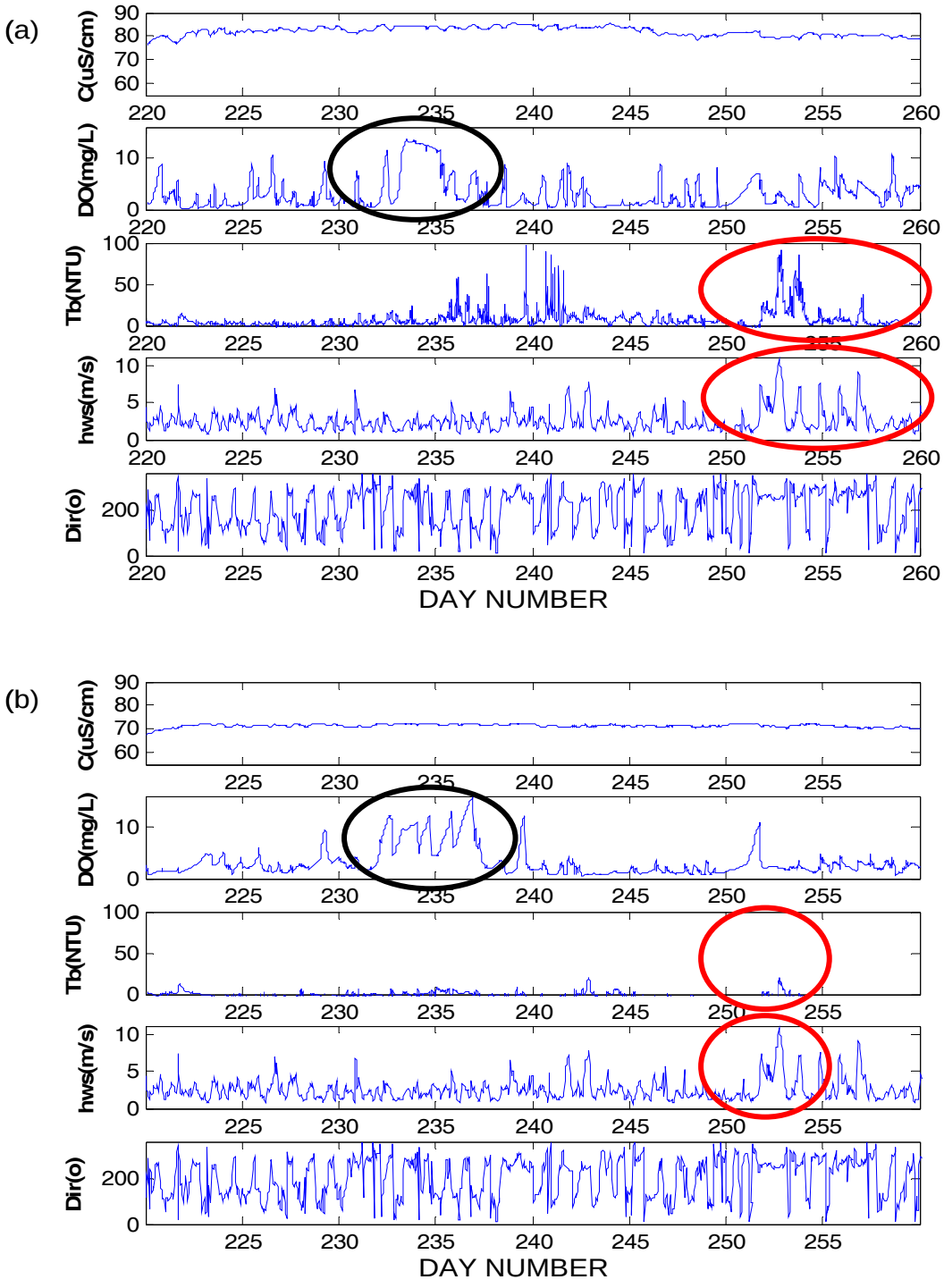

Figure 3.8 Comparison of data variables, including conductivity (µS cm^{-1}), DO (mg L^{-1}), turbidity (NTU), hourly wind speed (m s^{-1}) and wind direction (degree) from August 8, 2005 to September 17, 2005. Hourly wind data were obtained from CIMIS Station 128, closest to the three sediment observation stations: (a) Station 4 m; (b) Station 6 m upper; (c) Station 6 m bottom; (d) Station 8 m.

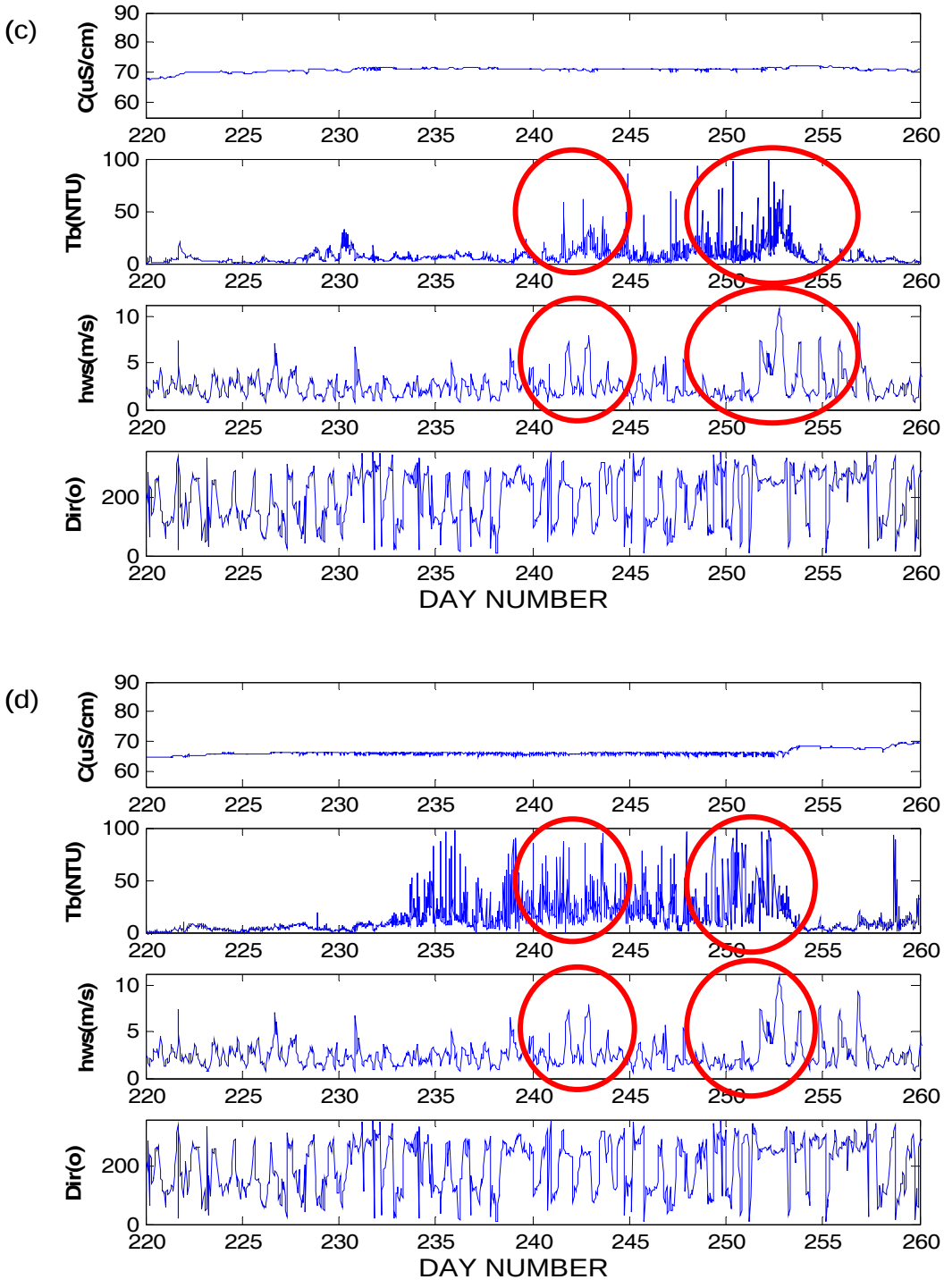

Figure 3.11 (continued) Comparison of data variables, including conductivity (µS cm^{-1}), DO (mg L^{-1}), turbidity (NTU), hourly wind speed (m s^{-1}) and wind direction (degree) from August 8, 2005 to September 17, 2005. Hourly wind data were obtained from CIMIS Station 128, closest to the three sediment observation stations: (a) Station 4 m; (b) Station 6 m upper; (c) Station 6 m bottom; (d) Station 8 m.

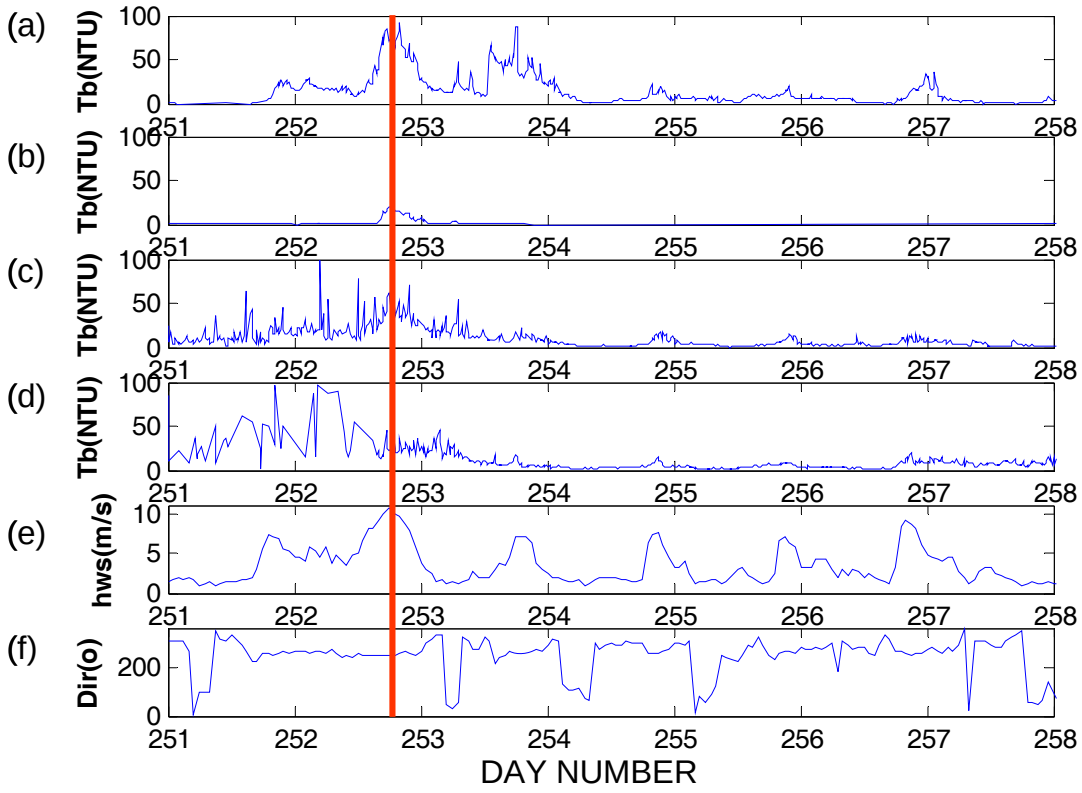

Figure 3.9 Comparison of turbidity (NTU), wind data of CIMIS Station 128 from September 8, 2005 to September 15, 2005: (a) Station 4 m; (b) Station 6 m upper; (c) Station 6 m bottom; (d) Station 8 m; (e) hourly wind speed (m s^{-1}); (f) wind direction (degree).

AWAC Data

Data on current speed and direction from the AWAC between August 4, 2005 and November 29, 2005 are shown in Figure 3.13. White spaces in the figure indicate no data could be retrieved for the time period or elevation due to malfunction of the instrument. In the figure, current speed varies from 0 to 0.3 m s^{-1}. Higher current speeds, around 0.2 m s^{-1}, are observed at the bottom around days 255 and 281 and can be explained by the hourly wind speed data. Similar values of velocity at the sampling locations were obtained by Cook et al. (2002) in their numerical simulations. Dominant current directions are around 300 degrees at the bottom, mainly in the western direction for the period. (The direction of currents is flowing toward , e.g. 270° is flowing to the west)

East-North-Up (ENU) current velocities (m s^{-1}) are shown in Figure 3.14. It is noticeable that the surface velocity reversed direction for a few days, specifically days 263, 270, 278, and 280. The reversals demonstrate that wind produces currents at the

surface of the Salton Sea in the direction of the wind, i.e. eastern direction, and return currents due to pressure near the bottom, i.e. western direction.

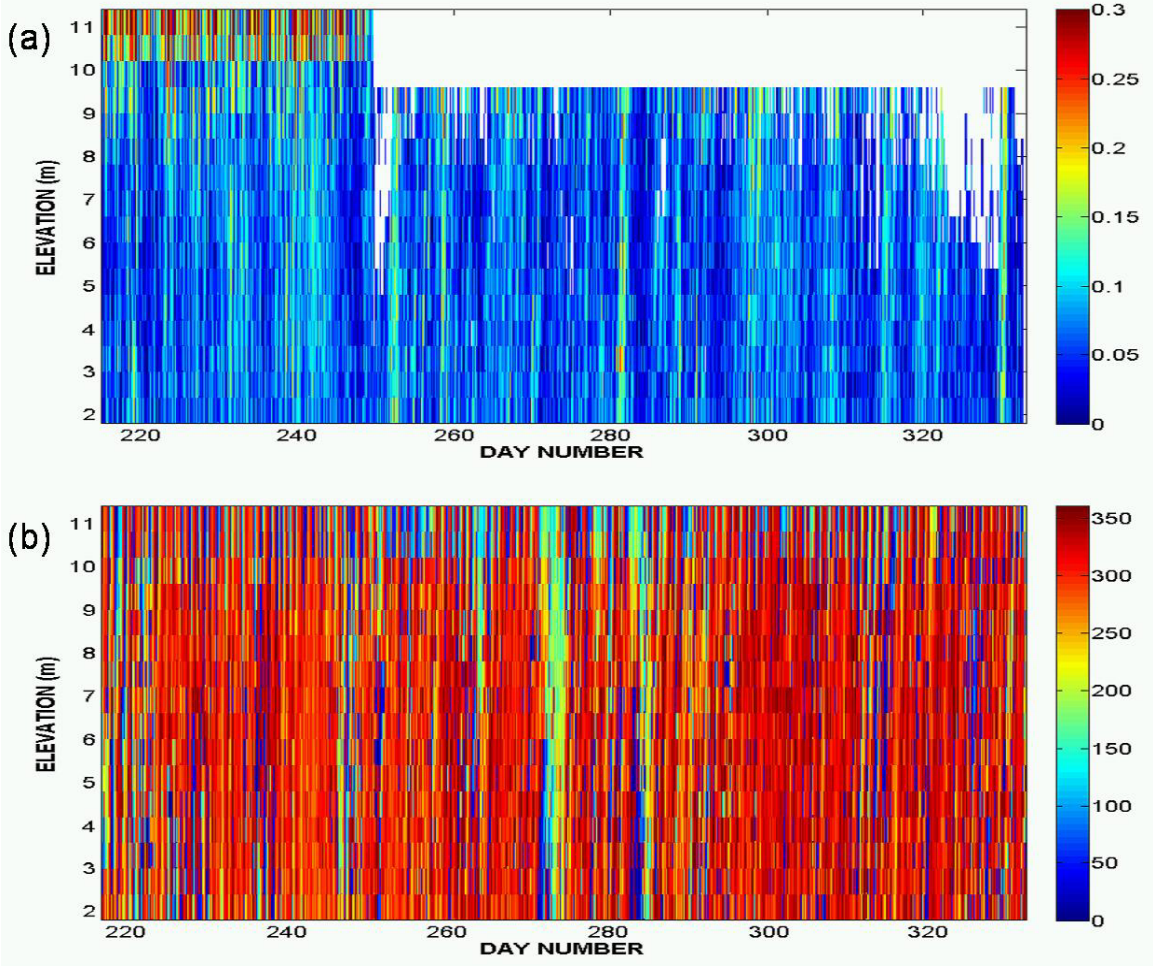

Figure 3.10 Elevation-time contours of current data of AWAC from August 4, 2005 to November 29, 2005: (a) current speed (m s^{-1}); (b) current direction (degree).

Daily averaged signal strength (counts) from August 8, 2005 to September 17, 2005 is produced in Figure 3.15. Higher signal strengths are observed for days 252–260 close to the bottom, which is coincident with higher wind speeds during that period. Daily profiles of averaged signal strength (counts) every 3 days from August 12, 2005 (day 224) to September 14, 2005 (day 257) are produced in Figure 3.16. Signal strengths at the bottom were from 70 counts to 100 counts, and these strengths decreased exponentially as the elevation increases. At the surface, the strengths increased from 10 counts up to 100 counts, which is likely due to near boundary effects, for example, bubbles, phytoplankton, zooplankton, and debris, rather than suspended sediments itself.

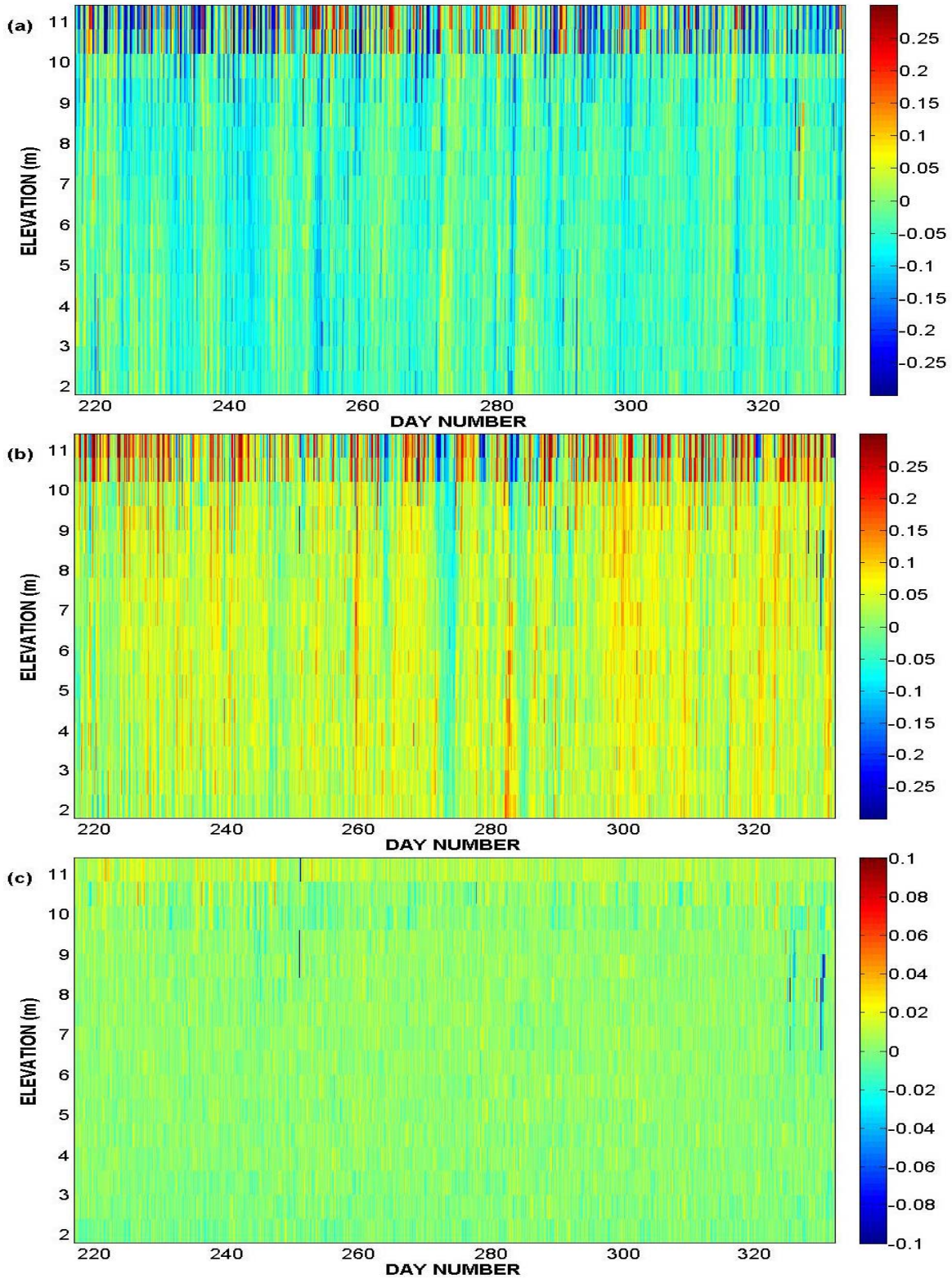

Figure 3.11 Elevation-time contour of ENU velocity of AWAC from August 4, 2005 to November 29, 2005: (a) East current velocity (m s^{-1}); (b) North current velocity (m s^{-1}); (c) Up current velocity (m s^{-1}).

Signal strength naturally decreases logarithmically with the distance to the source and no correction has been made to normalize these data. Values should only be compared at the same distance from the bottom mounted sensor (Lohrmann, 2001).

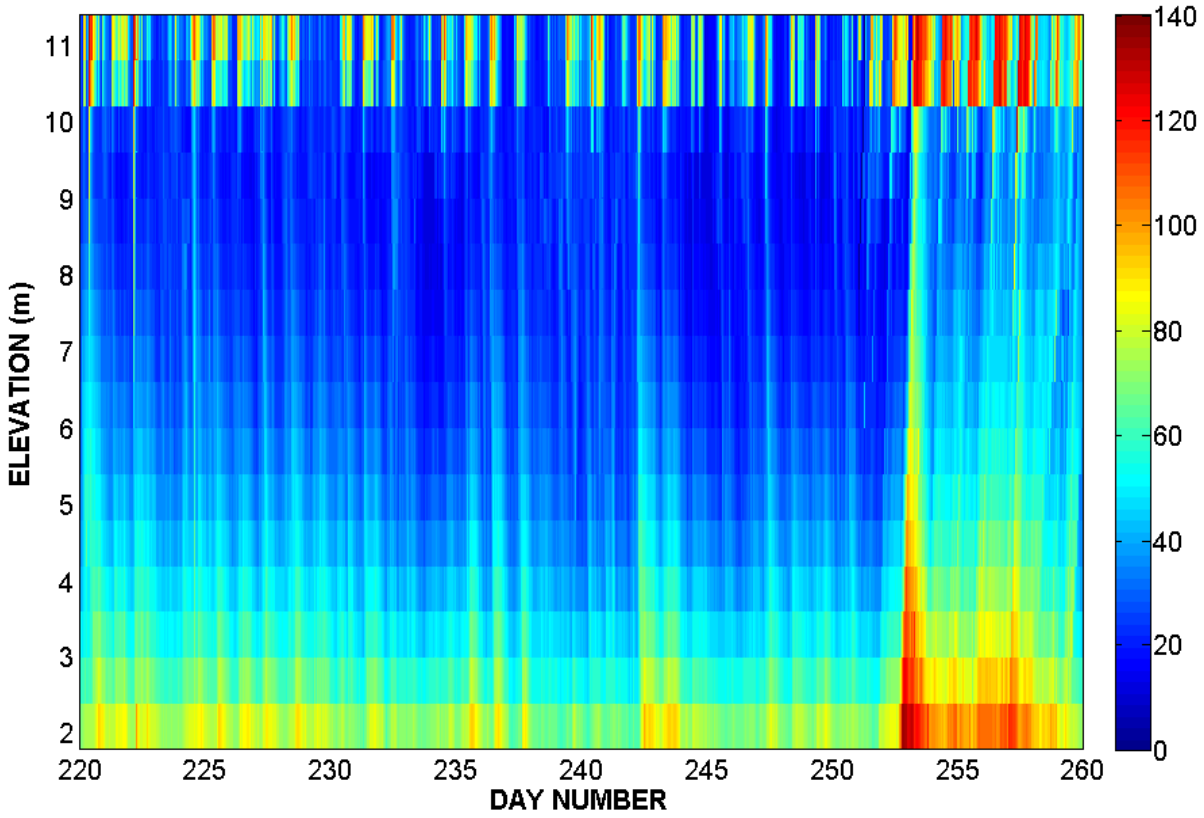

Figure 3.12 Elevation-time contour of daily averaged signal strength (counts) from August 8, 2005 to September 17, 2005.

The signal strength (or backscattering strength or signal amplitude) of the AWAC was used to evaluate the condition of the sediment resuspension of the Sea. Acoustic sensors receive scatterings of acoustic signals from particles in suspension; the signal strength can provide information about the quantity and type of particulate matter in the water column (Lohrmann, 2001). The profiles of signal strength are compared on Figure 3.17 with the well-known Rousean distribution, which is valid for open-channel flow, as follows:

$$\bar{c} = \bar{c}_b \left[\frac{(H-z)/z}{(H-b)/b} \right]^Z \tag{3.1}$$

$$Z = \frac{w_s}{\kappa u_*} \tag{3.2}$$

where $\bar{c}$ is the local mean volume concentration of suspended sediment, $\bar{c}_b$ denotes a near-bed values of $\bar{c}$, H is water depth, b is a distance taken to be close to the bed, z is

vertical distance above the bed, and κ denotes the von Kármán constant and Z denotes the dimensionless Rouse number (García, 1999).

When Z is set as 0.5 in the Rousean distribution, the Rousean profile shows a similar trend with signal strength profiles. According to Equation (3.2), we could recalculate sediment diameters vary between 9 μm and 42 μm, depending on the local time value of the shear velocity. This range overlaps with the range of sediment sizes discussed in the Chapter 2.

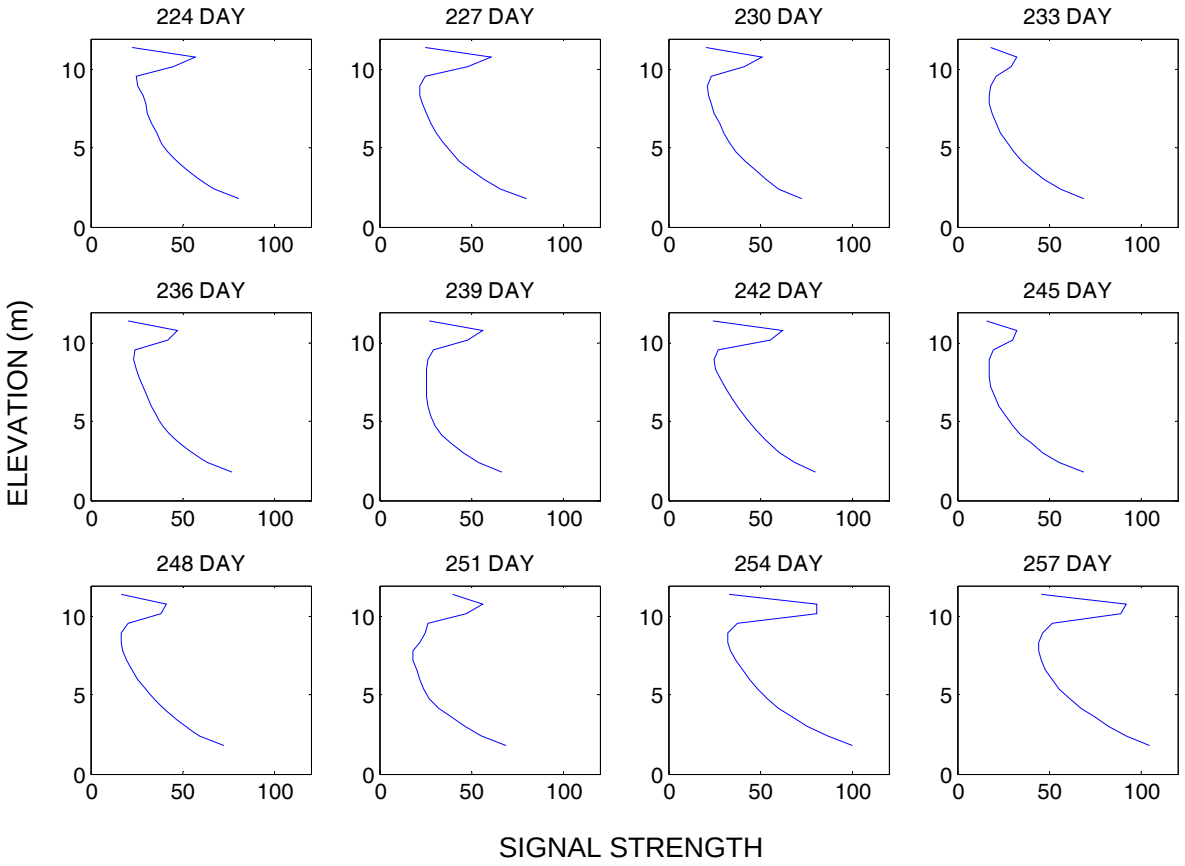

Figure 3.13 Comparison of daily averaged signal strength (counts) profiles at every 3 days from August 12, 2005 (224 day) to September 14, 2005 (257 day)

Wave data from the AWAC consist of significant wave height (Hs), which is the average height of the highest one-third waves in a wave record (Earle, 1996); mean 1/10 wave height (H10); maximum wave height (Hmax); mean period (Tm); peak period (Tp), which is period corresponding to the frequency band with the maximum value of spectral density in the non-directional wave spectrum (NOAA, 2006); mean zero crossing period (Tm0) closely approximating time domain mean period which would be obtained from zero-crossing analysis of a wave elevation record (Earle, 1996); peak direction (PDir); and mean direction (MDir). All heights are in meters, periods in seconds, and direction in

degrees. Mean wave direction corresponding to energy of the dominant period (DOMPD) and the units are degrees from true North just like wind direction.

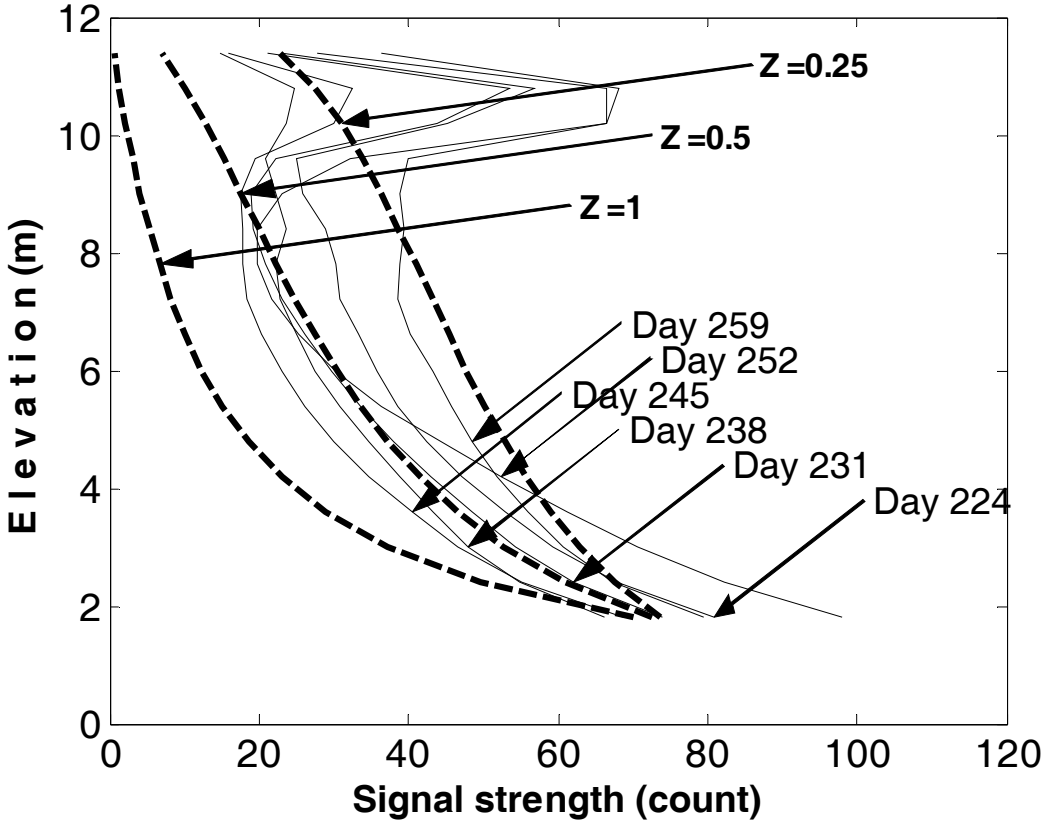

Figure 3.14 Comparison between daily averaged signal strength (count) profiles and the Rousean distribution: thin black lines are signal strength profiles observed every three days from day 224 to 257 and the dashed lines represent the Rousean distribution. Large values of the signal strength on the upper part of the depth can be attributed to side lobe interference, as reported in the AWAC User guide (2004) (Nortek, 2004).

Wave height, period and wave direction data of the AWAC from August 4, 2005 to November 29, 2005 are shown in Figure 3.18. Wave data are also compared with hourly wind data of CIMIS Station 128. Wave height peaks in Figure 3.18 are concurrent with higher wind speed data, especially at days 250 – 260, days 281 – 285, days 288 – 292, and days 298 – 303.

All four turbidity data sets (NTU), wind speed (m s^{-1}) and wind direction (degree) of CIMIS Station 128, wave height (m) and bottom current speed (m s^{-1}) from September 8, 2005 to September 15, 2005 are compared in Figure 3.19. There is a lag between the peaks of current speed and turbidity, but the peaks of wave height, wind intensity and turbidity are in phase.

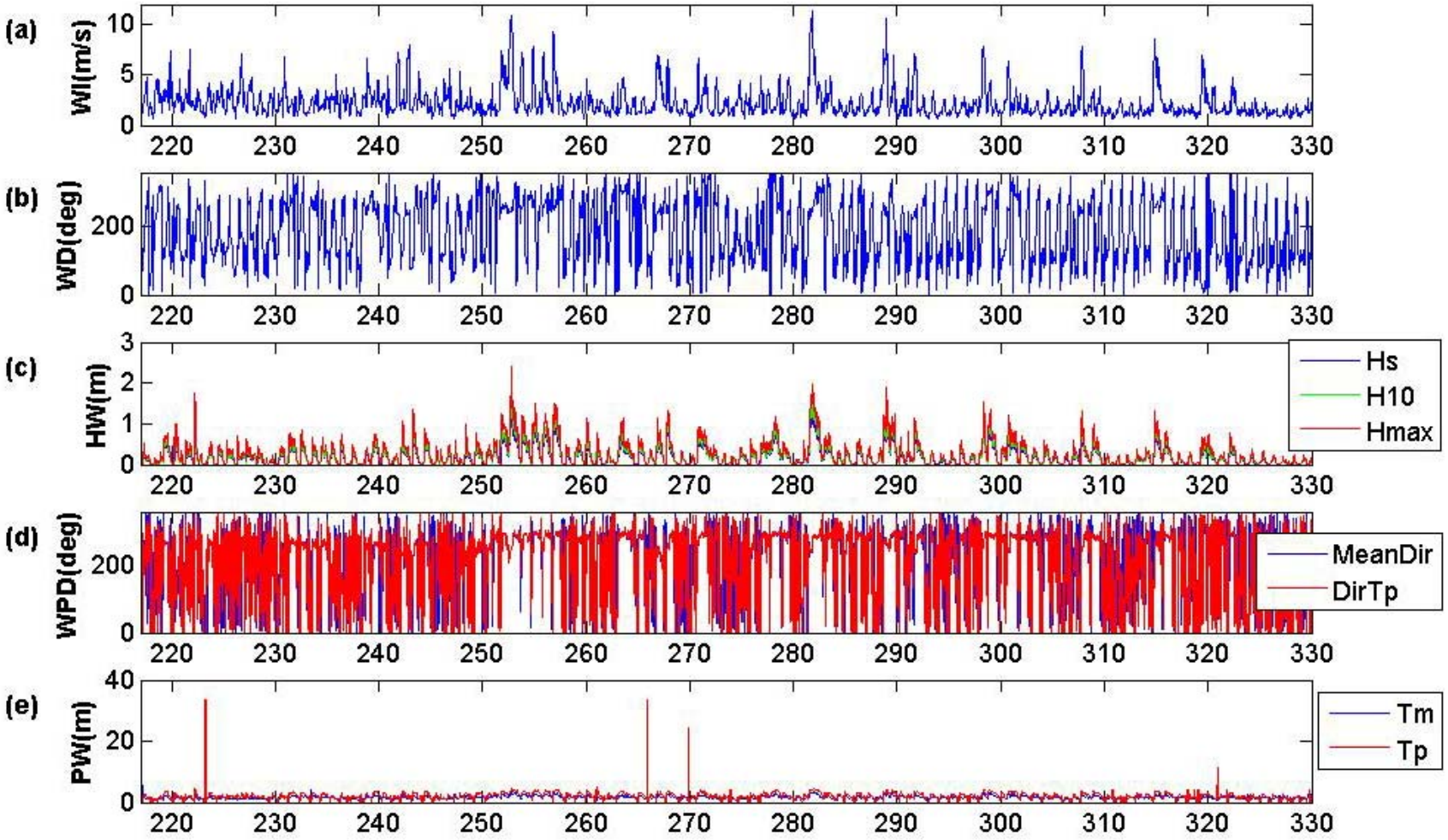

Figure 3.15 Wave height and period and wave direction of AWAC compared with hourly wind data from CIMIS Station 128 from August 4, 2005 to November 29, 2005: (a) wave height (m); (b) wave period (s); (c) wave direction (degree); (d) hourly wind speed (m s^{-1}); (e) hourly wind direction (degree).

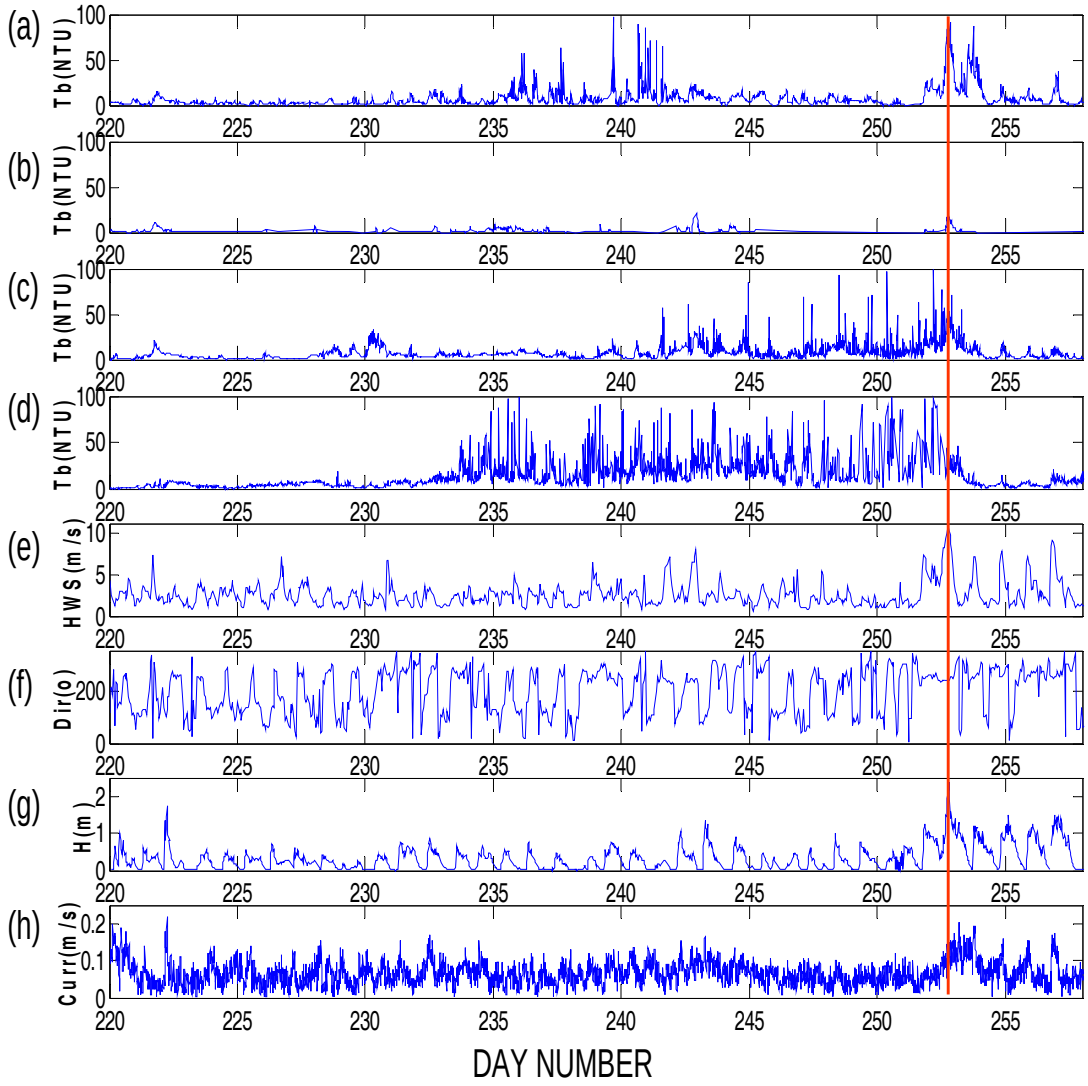

Figure 3.16 Comparison of turbidity (NTU), wind speed and wind direction from CIMIS Station 128, wave height and current from September 8, 2005 to September 15, 2005: (a) Station 4 m; (b) Station 6 m upper; (c) Station 6 m bottom; (d) Station 8 m; (e) hourly wind speed (m s^{-1}); (f) wind direction (degree); (g) wave height (m); (h) current intensity (m s^{-1}).

Turbidity at Stations 4 m, 6 m bottom, 8 m, hourly wind speed (m s^{-1}) and direction (degree) of CIMIS Station 128, wave height (m) and direction (degree), bottom current speed (m s^{-1}) and direction (degree) from August 8, 2005 to September 17, 2005 are compared in Figure 3.20. The vertical red lines in the figure show strong wind events. When a peak in turbidity occurs, there is often an associated peak in wind intensity with wind from the west and corresponding peak in the wave height. But peaks in turbidity do not always imply wind peaks or peaks in wave height, since turbidity might be increased by other factors, such as internal wave interactions and bioturbation.

Examination of Figures 3.19 and 3.20 reveals that the occurrence of peaks in wave height can be clearly associated with peaks in wind speed (within the temporal resolution of the data collection), denoting an evident cause-effect relation. However, the peaks in bottom current speed are not coincident with the peaks in wind intensity. It becomes apparent that relatively high winds with a strongly defined direction are responsible for the larger current speeds observed at the bottom; however, the larger bottom current speeds appear almost one day later. The delay is likely attributable to the time it takes to produce the large-scale gyre that characterizes the southern portion of the Salton Sea (see Cook et al., 2002). Very importantly, the peaks of wind intensity, wave heights and turbidity appear to coincide, at least after wind has been acting for some time in a specific direction. The correlation suggests that waves are likely the predominant mechanism for sediment resuspension, as expected, and that the sediment entrained comes mainly from locations nearby. In further support, OBS readings at the two different elevations of the station located at 6-m of depth follow this same trend.

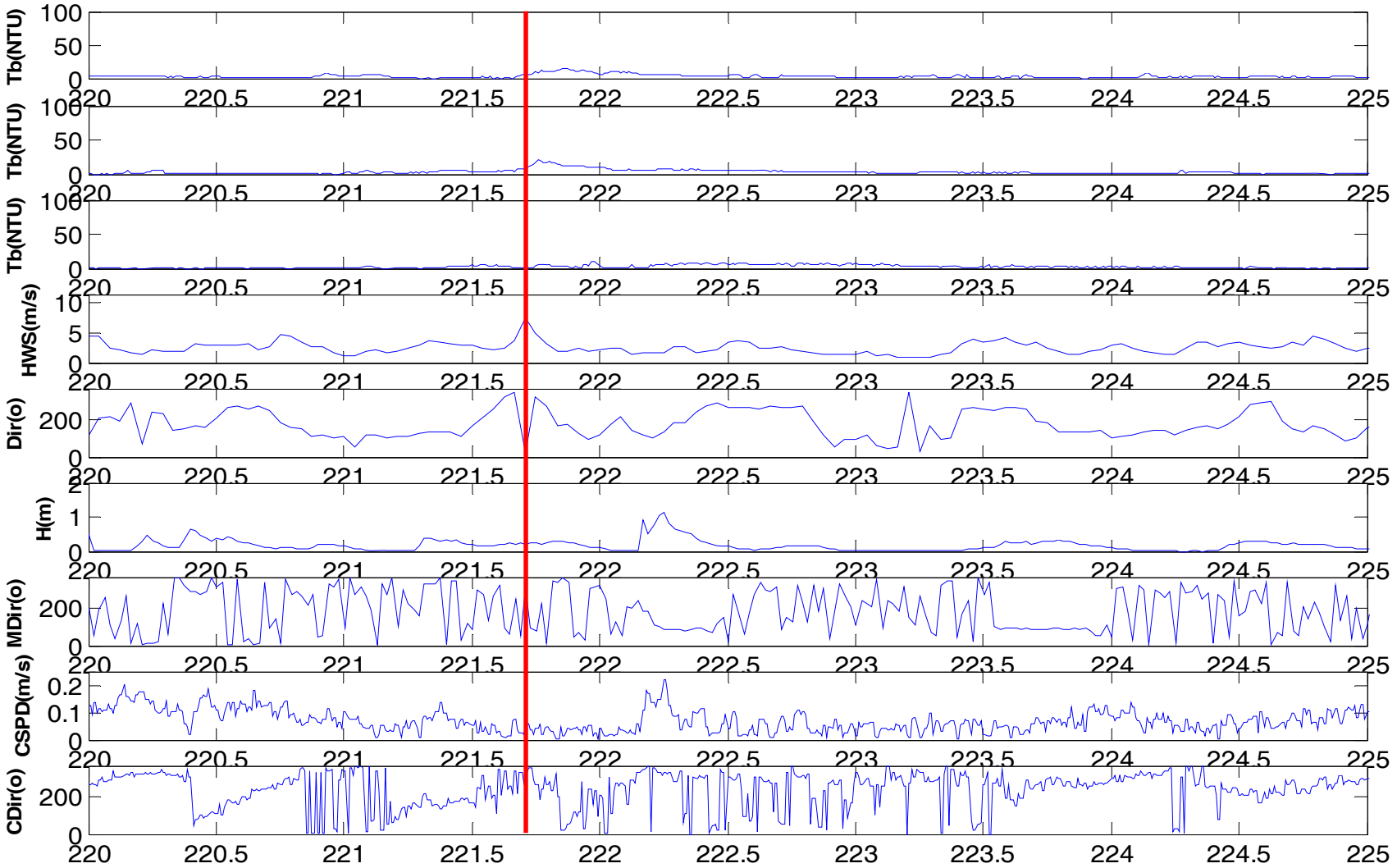

Figure 3.17 Comparison of turbidity (NTU) at Stations 4 m, 6 m bottom, 8 m, and hourly wind speed (m s^{-1}) and direction (degree) from CIMIS Station 128, wave height (m) and direction (degree), bottom current speed (m s^{-1}) and direction (degree) from August 8, 2005 to September 17, 2005.

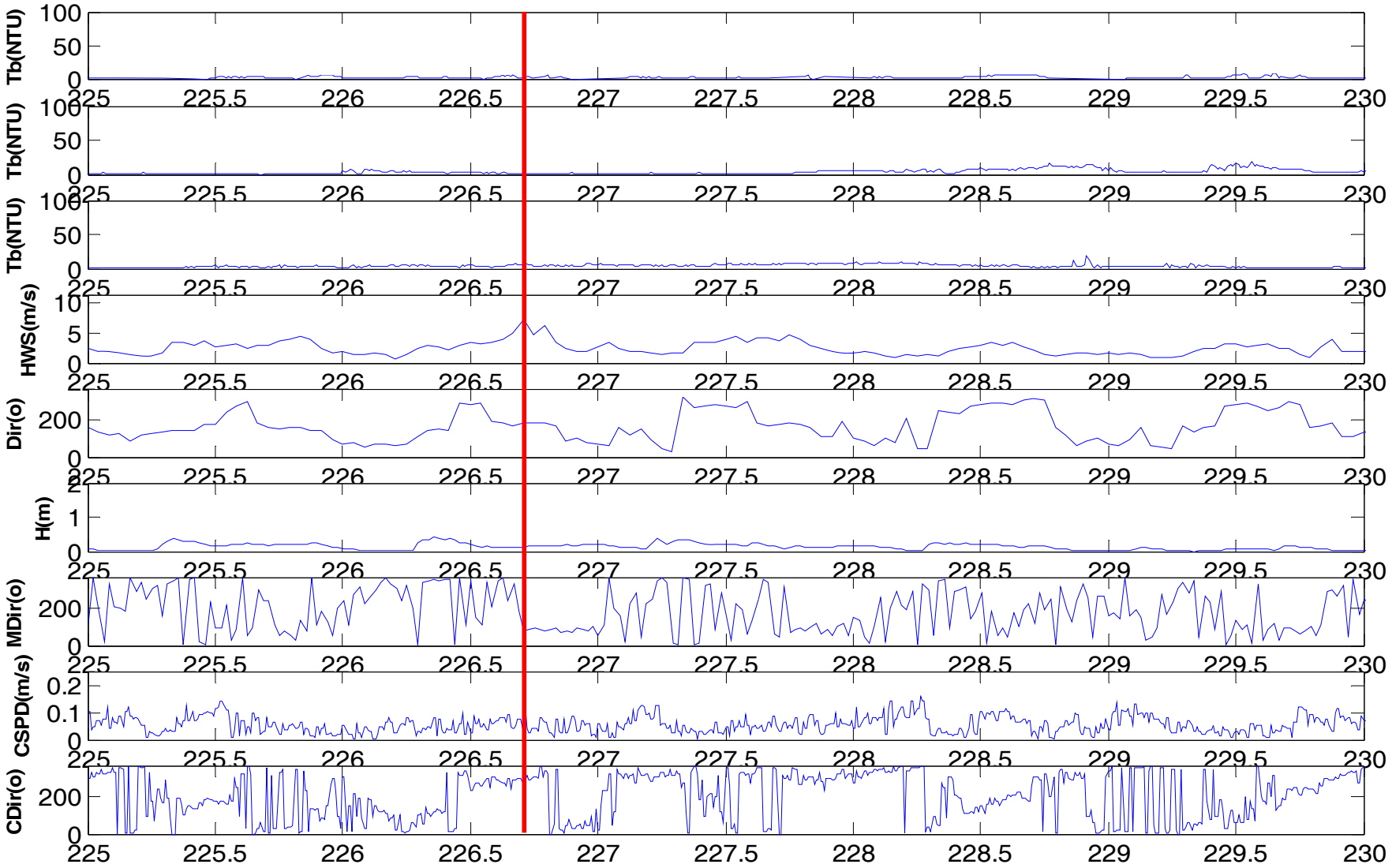

Figure 3.20 (continued) Comparison of turbidity (NTU) at Stations 4 m, 6 m bottom, 8 m, hourly wind speed (m s^{-1}) and direction (degree) from CIMIS Station 128, wave height (m) and direction (degree), bottom current speed (m s^{-1}) and direction (degree) from August 8, 2005 to September 17, 2005.

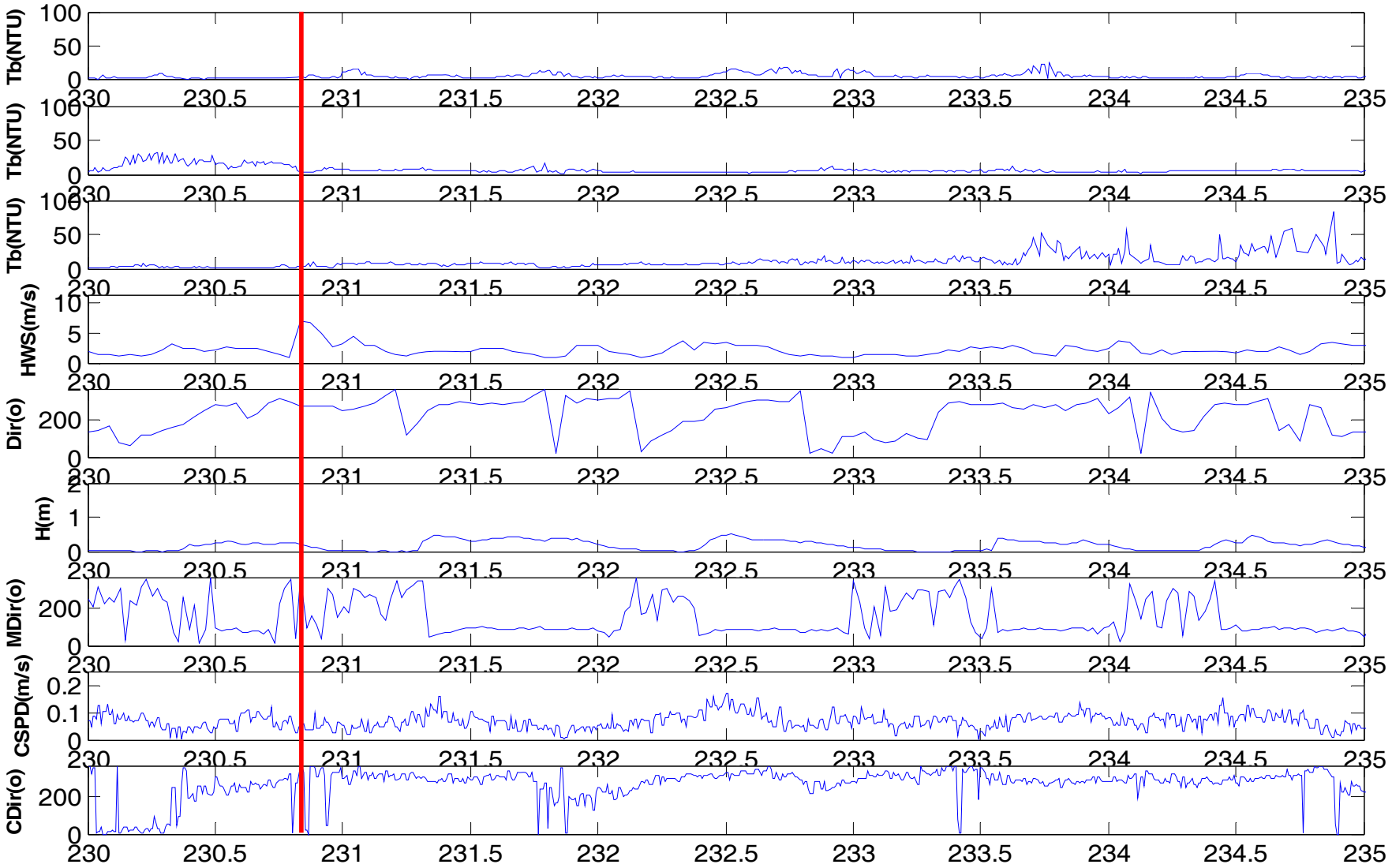

Figure 3.20 (continued) Comparison of turbidity (NTU) at Stations 4 m, 6 m bottom, 8 m, hourly wind speed (m s^{-1}) and direction (degree) from CIMIS Station 128, wave height (m) and direction (degree), bottom current speed (m s^{-1}) and direction (degree) from August 8, 2005 to September 17, 2005.

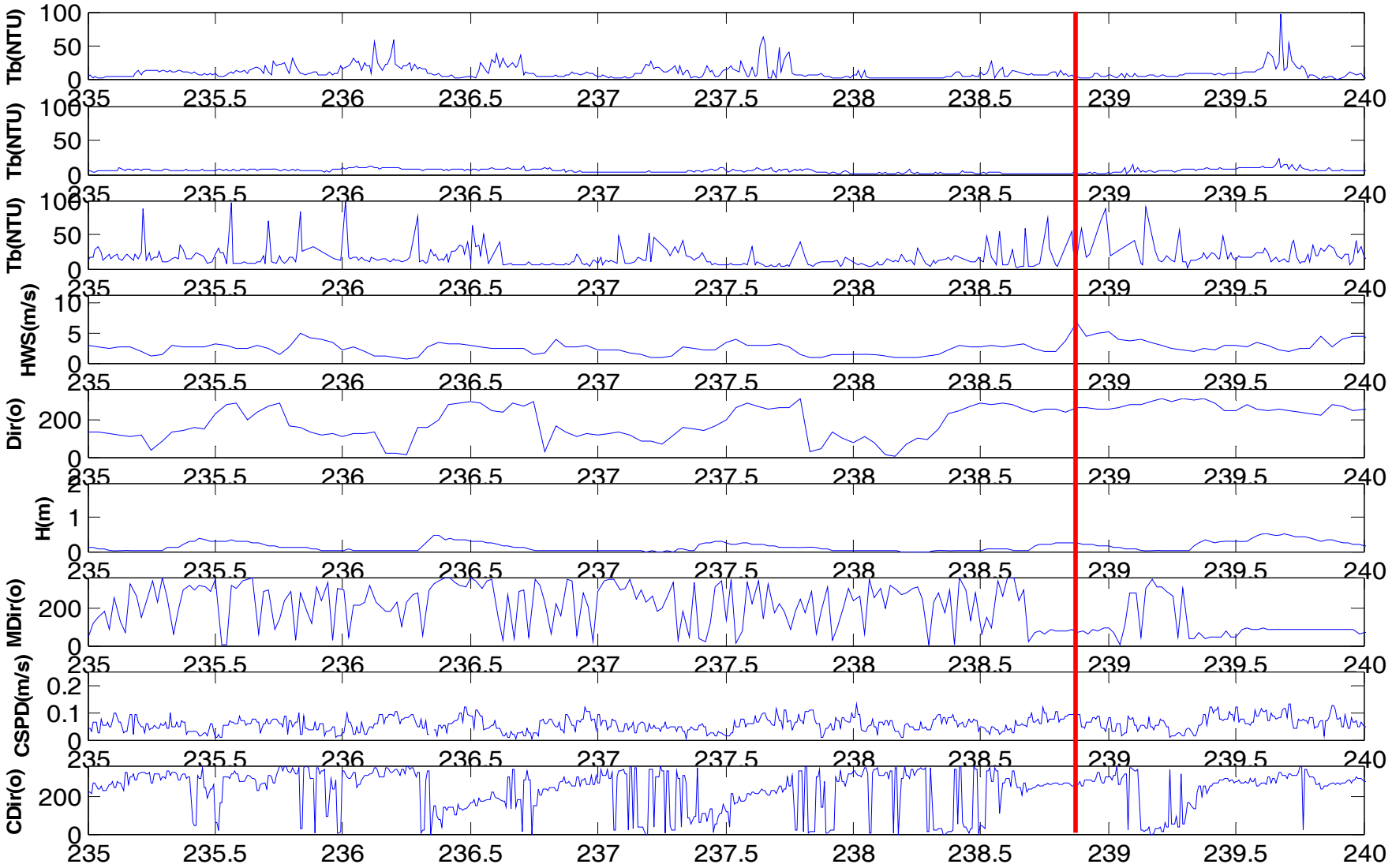

Figure 3.20 (continued) Comparison of turbidity (NTU) at Stations 4 m, 6 m bottom, 8 m, hourly wind speed (m s^{-1}) and direction (degree) from CIMIS Station 128, wave height (m) and direction (degree), bottom current speed (m s^{-1}) and direction (degree) from August 8, 2005 to September 17, 2005.

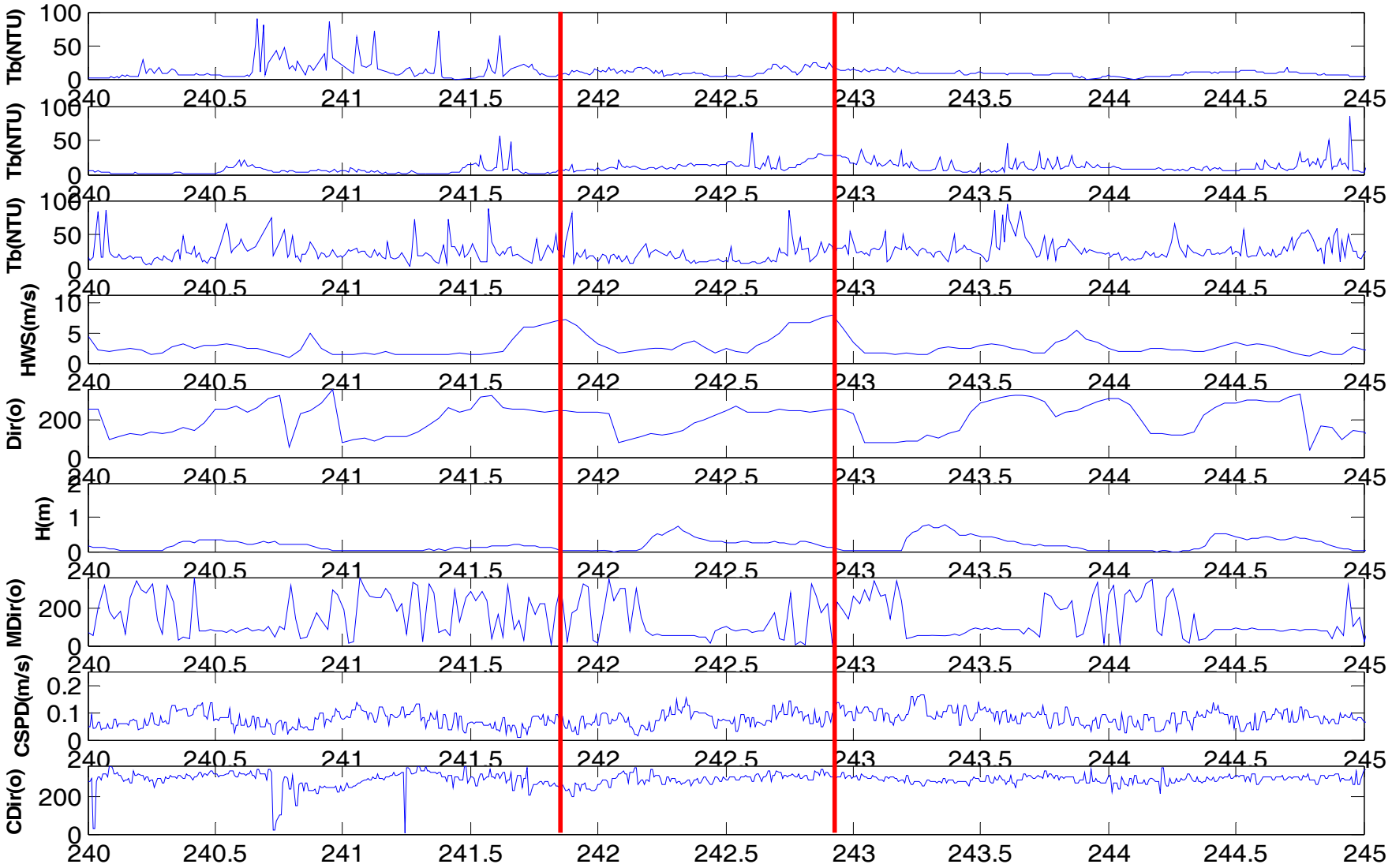

Figure 3.20 (continued) Comparison of turbidity (NTU) at Stations 4 m, 6 m bottom, 8 m, hourly wind speed (m s^{-1}) and direction (degree) from CIMIS Station 128, wave height (m) and direction (degree), bottom current speed (m s^{-1}) and direction (degree) from August 8, 2005 to September 17, 2005.

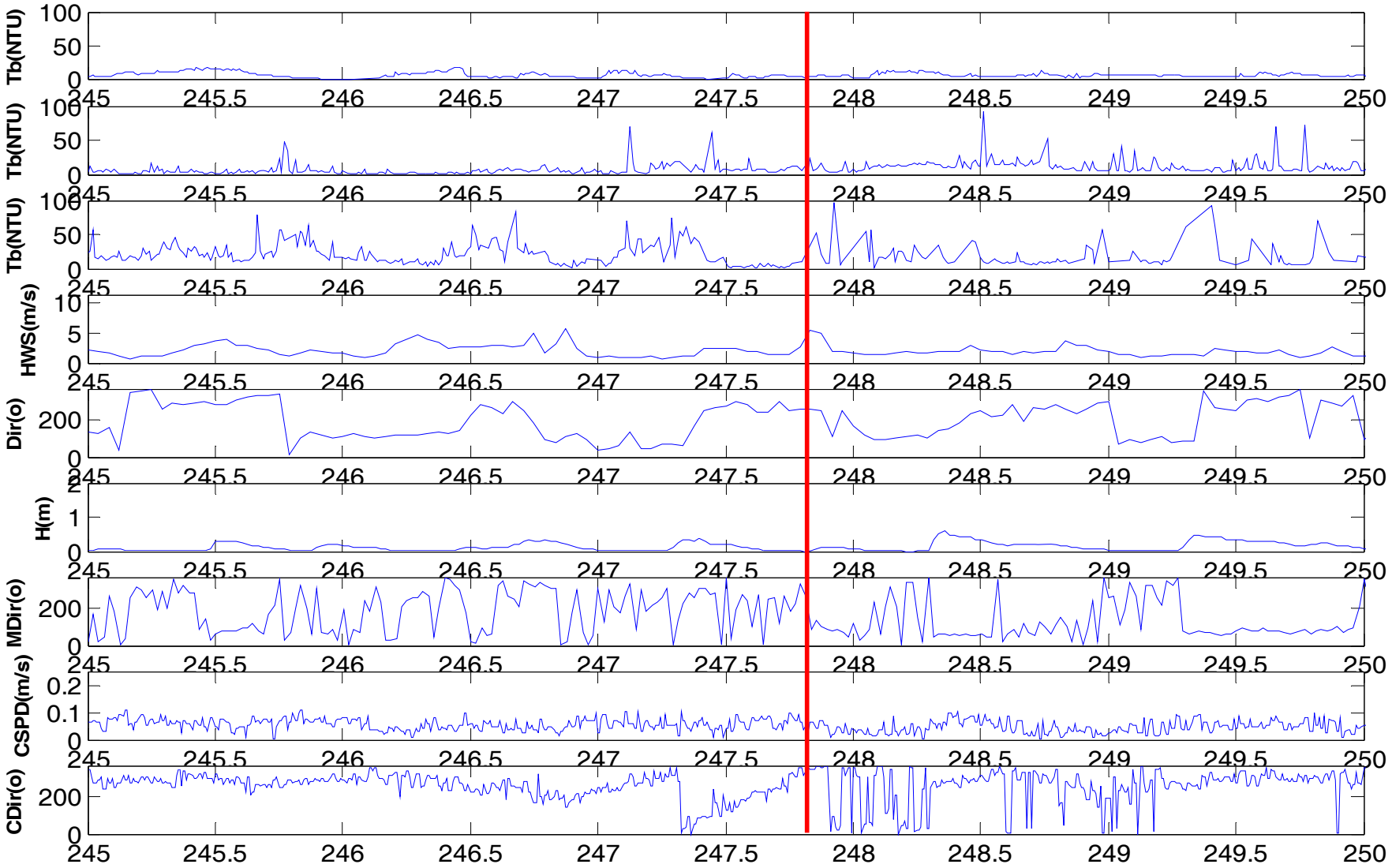

Figure 3.20 (continued) Comparison of turbidity (NTU) at Stations 4 m, 6 m bottom, 8 m, hourly wind speed (m s^{-1}) and direction (degree) from CIMIS Station 128, wave height (m) and direction (degree), bottom current speed (m s^{-1}) and direction (degree) from August 8, 2005 to September 17, 2005.

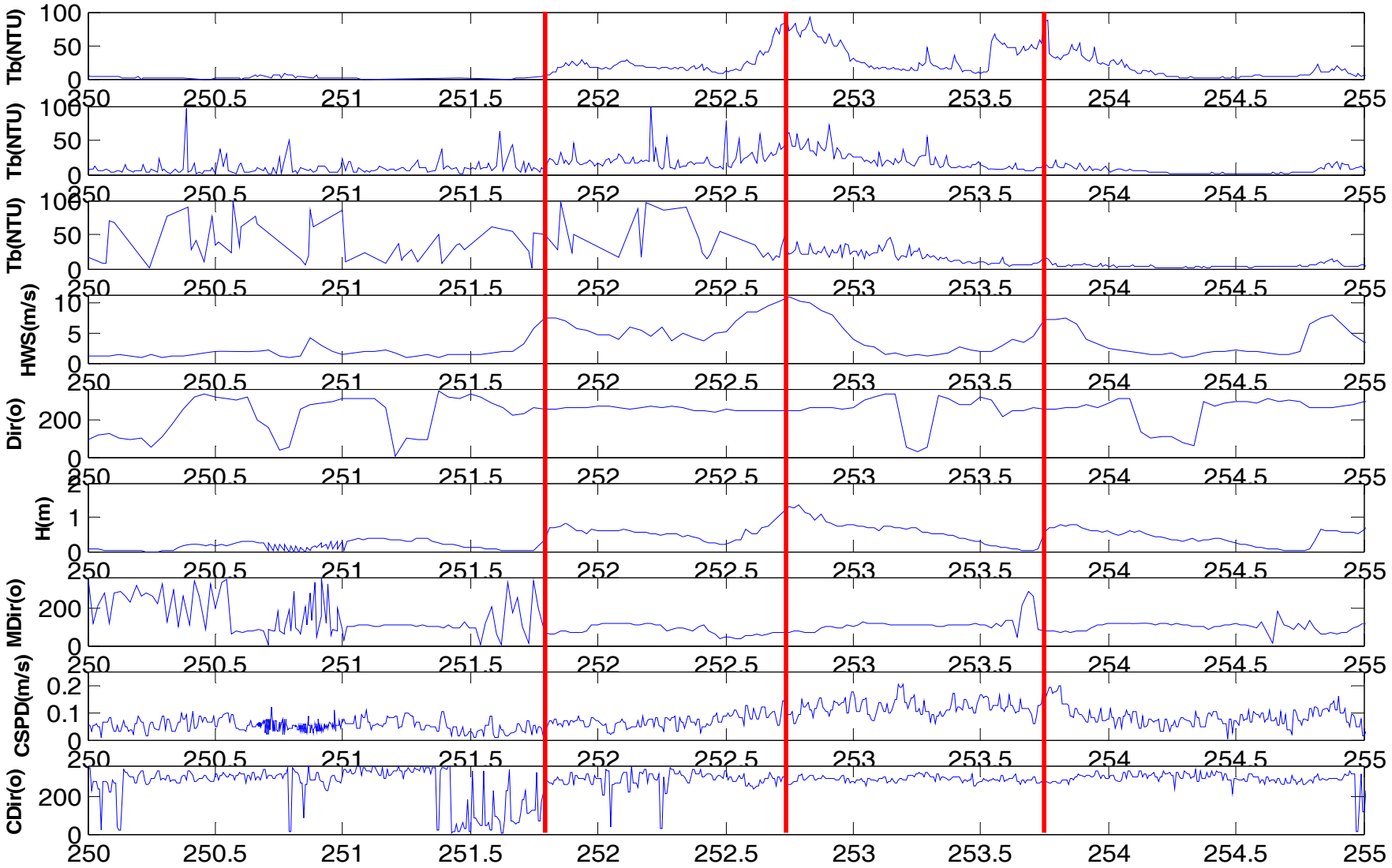

Figure 3.20 (continued) Comparison of turbidity (NTU) at Stations 4 m, 6 m bottom, 8 m, hourly wind speed (m s^{-1}) and direction (degree) from CIMIS Station 128, wave height (m) and direction (degree), bottom current speed (m s^{-1}) and direction (degree) from August 8, 2005 to September 17, 2005.

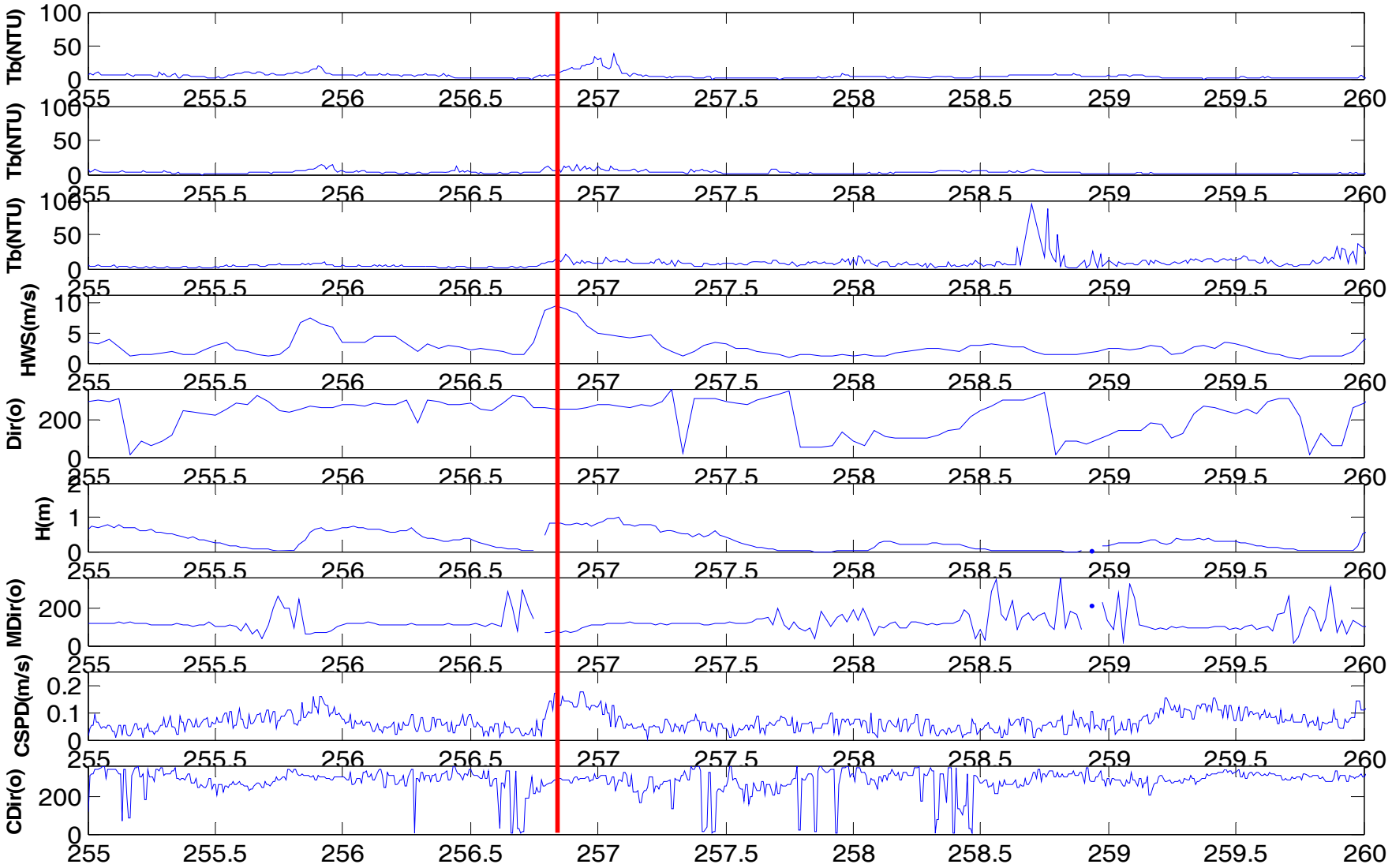

Figure 3.20 (continued) Comparison of turbidity (NTU) at Stations 4 m, 6 m bottom, 8 m, hourly wind speed (m s^{-1}) and direction (degree) from CIMIS Station 128, wave height (m) and direction (degree), bottom current speed (m s^{-1}) and direction (degree) from August 8, 2005 to September 17, 2005.

THEORETICAL ANALYSIS OF SEDIMENT ENTRAINMENT FORMULAE

Based on the measured data discussed in the preceding section, a review and analysis of previous formulae of sediment entrainment into suspension (sediment resuspension) is made. Non-linear correlations between turbidity readings near the bottom (a surrogate for suspended solids in the water columns) and wind speeds are presented in this section, even though specific knowledge on sediment properties in the Salton Sea, such as sediment density and sediment size, is quite limited. Furthermore, the turbidity data were highly scattered due to bioturbation as well as to the malfunction of the YSI instruments caused by the unique chemically and biologically rich environment of the Salton Sea.

Theoretical background

Many expressions have been proposed for non-*cohesive* sediment for prediction of equilibrium near-bed entrainment as a function of the bed shear stress. Most of them follow power relations, such as Equation (2.2), with the exponent, P, ranging from 1 to as high as 5 (García and Parker, 1991; 1993). Using scaling techniques, like the one presented in the Appendix I for the formulae by García and Parker (1991; 1993), exponents have been determined from the data for the shear stress and the wind speed for use in Equation (2.2).

While the shear stress depends on the wind speed to a fixed second power for currents (by inspection of Equation (2.8)), the exponent for the waves was also established as 2 by Kamphuis (1975). The exponent of the bed shear stress due to wind-induced waves and the wind speed was determined from the data for use in Equations (2.12) – (2.15). The log-log plot of the bed shear stress and the wind speed is shown in Figure 3.21 with the tangent linear slope estimated only when the bed shear stresses are above the critical shear stress, 6.59e-2 Pa. The relation between the bed shear stress and the wind speed is not linear, but tangent slopes of the bed shear stress curve vary according to the wind intensity. The tangent slopes are steeper as shear stresses decrease. The slope of the curve above the critical shear stress is $1.858 \approx 2.0$. Consequently, it provides confirmation that the exponent of the bed shear stress due to wind-induced wave and the wind speed is approximately 2 as well.

Non-linear (power) relations of sediment resuspension as a function of the bed shear stress and the associated shear velocity for non-*cohesive* and *cohesive* sediments as shown in Equation (2.2) are listed in Table 3.2. The exponent, K, ranges from 2 to 10 both for currents and waves depending on the formulae. The range of K values is larger for non-*cohesive* sediments (2–10) than that for *cohesive* sediments (2 – 4). Mathematical derivation of the expressions of sediment erosion rates in Table 3.2 is detailed in Appendix I.

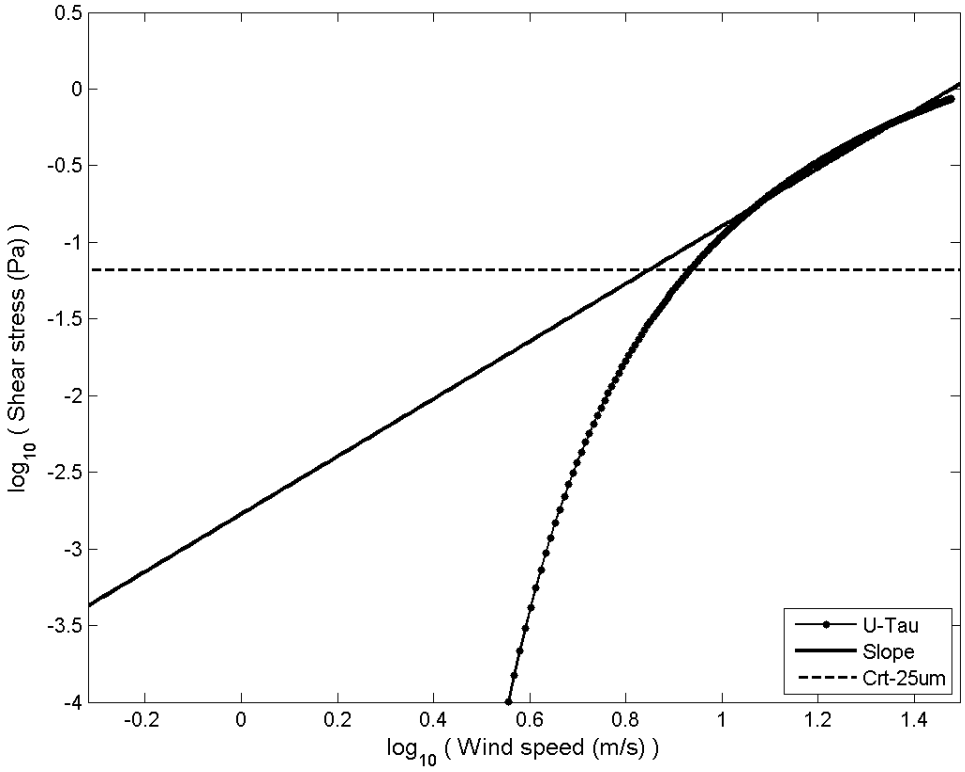

Figure 3.18 Plot of the bed shear stress (Pa) according to the wind speed (m s^{-1}) with the tangent linear slope above the critical Shields shear stress (Pa).

Table 3.2 Relationship of sediment resuspension as a function of bed shear stress and the associated shear velocity as shown in Equation (2.2) (Akiyama and Fukushima, 1986; Arulanandan, 1975; Celik and Rodi, 1984; García and Parker, 1991; 1993; Kandiah, 1974; Mehta, 1981; Mian and Yanful, 2004; Sanford and Maa, 2001; Smith and McLean, 1977; Thorn and Parsons, 1980; Van Rijn, 1984; Zyserman and Fredsoe, 1994).

Author	P	K (currents)	K (waves)
Non-*Cohesive* Sediment			
García and Parker (1991; 1993)	2.5	5	5
Smith and McLean (1977)	1	2	2
Van Rijn (1984)	1.5	3	3
Celik and Rodi (1984)	1.5	3	3
Akiyama and Fukushima (1986)	5	10	10
Zyserman and Fredsoe (1994)	1.75	3.5	3.5
Cohesive Sediment			
Mian and Yanful (2004)	2	4	4
Sanford and Maa (2001)	1	2	2
Kandiah (1974); Arulanandan (1975)	1	2	2
Mehta (1981)	1	2	2
Thorn and Parsons (1980)	1	2	2

It is interesting to compare the exponents of the formulae by García and Parker (1991; 1993) and by Mian and Yanful (2004) in Table 3.2, which are valid for non-*cohesive* and *cohesive* sediments, respectively. The exponents are very similar (5 and 4, respectively) and the exponent in Mian and Yanful (2004) appears to be much larger than those in other formulae for *cohesive* sediments. Since the García and Parker (1991; 1993) formula is valid for the fine sand-silt range (up to 100 μm), it is likely that the Mian and Yanful (2004) equation provides a transitional relationship from silt to clay. Consequently, it is assumed that this equation can be used for fine *cohesive* sediment.

Development of relations between turbidity and wind speed from observations in the Salton Sea

Relationships were derived between turbidity near the bottom and wind speed across the Sea at three observation stations. Turbidity (NTU) from Station 4 m, Station 6 m bottom and Station 8 m and hourly wind speed (m s^{-1}) from CIMIS Station 128 were analyzed using the general form of power equation is as follows:

$$f(x) = ax^b + c \tag{3.3}$$

where a, b, c are coefficients; x is independent variable; $f(x)$ denotes the estimated regression function. Data were selected from those times during which the bed shear stresses exceeded the critical shear stress.

Regressions for each station are presented in Figure 3.22 between turbidity (NTU) and hourly wind speed (m s^{-1}) from CIMIS Station 128 with their 95% prediction boundaries. The estimated powers (coefficient b) at each station were 4.76 at Station 4 m and 6.4 at Station 6 m, or 5.39 combining both stations, which overlaps the range of reviewed expressions in Table 3.2. The coefficients of the regressions with fixed exponents are shown in Table 3.3. The shear stress due to wind-induce waves might not dominate at Station 8 m, but the turbidity may be due to other causes, such as biological disturbance and physical circulation (gyres).

Table 3.3 Coefficients of power regressions between turbidity (NTU) and hourly wind speed (m s^{-1}) from CIMIS Station 128.

	a	*b*	*c*
Each station			
Station 4m	8.66e-4	4.76	10.09
Station 6m bottom	1.04e-5	6.40	9.15
Station 8m	0.689	1.13	12.58
Three stations			
Regression	1.52e-4	5.39	9.73
Power 4	3.83e-3	4	8.63
Power 5	3.79e-4	5	9.46

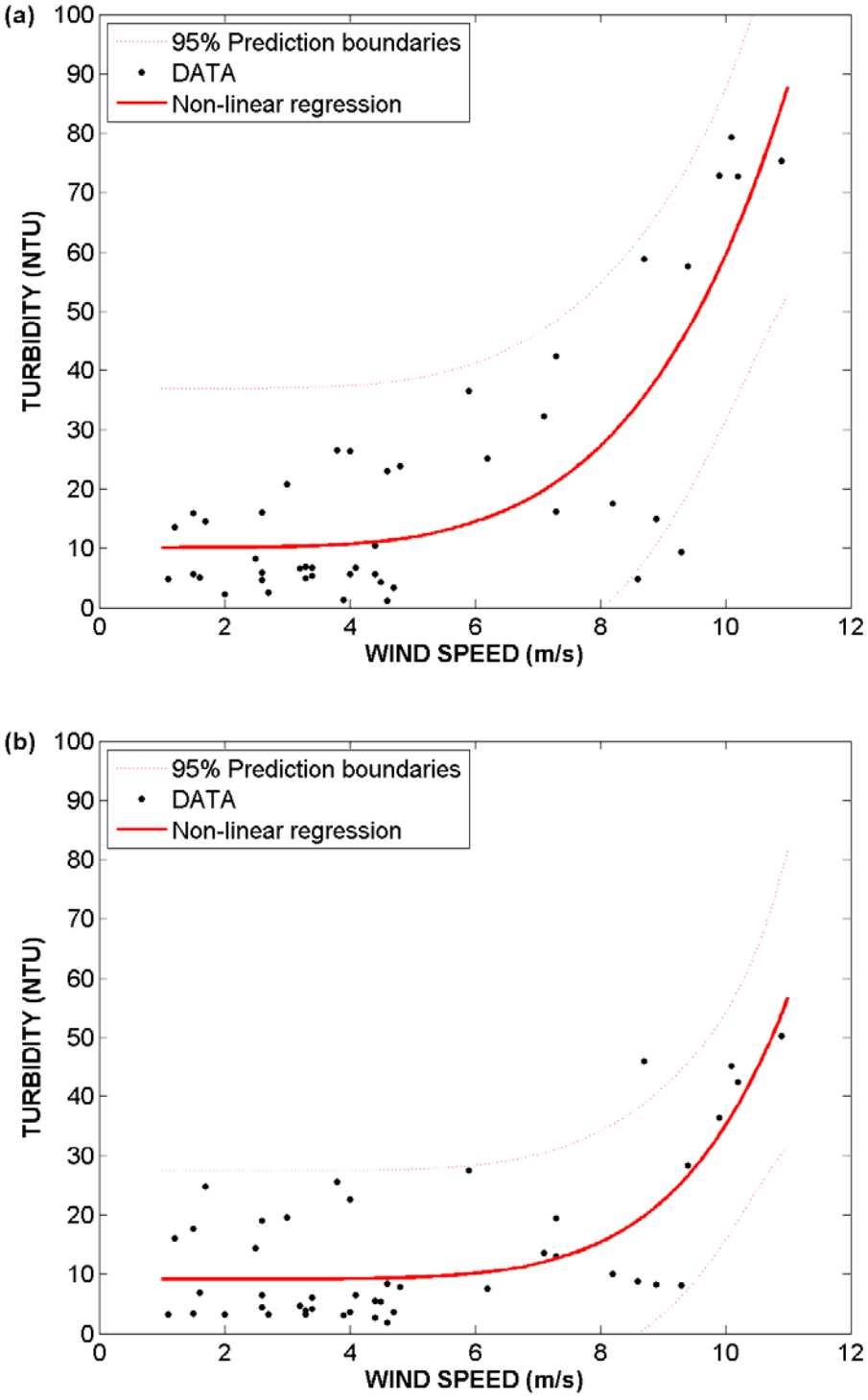

Figure 3.19 Non-linear regressions at the three stations between turbidity (NTU) and wind speed (m s^{-1}) with 95% prediction boundaries. Red lines indicate non-linear regression and black dots indicate data points: (a) Station 4 m; (b) Station 6 m bottom; (c) Station 8 m.

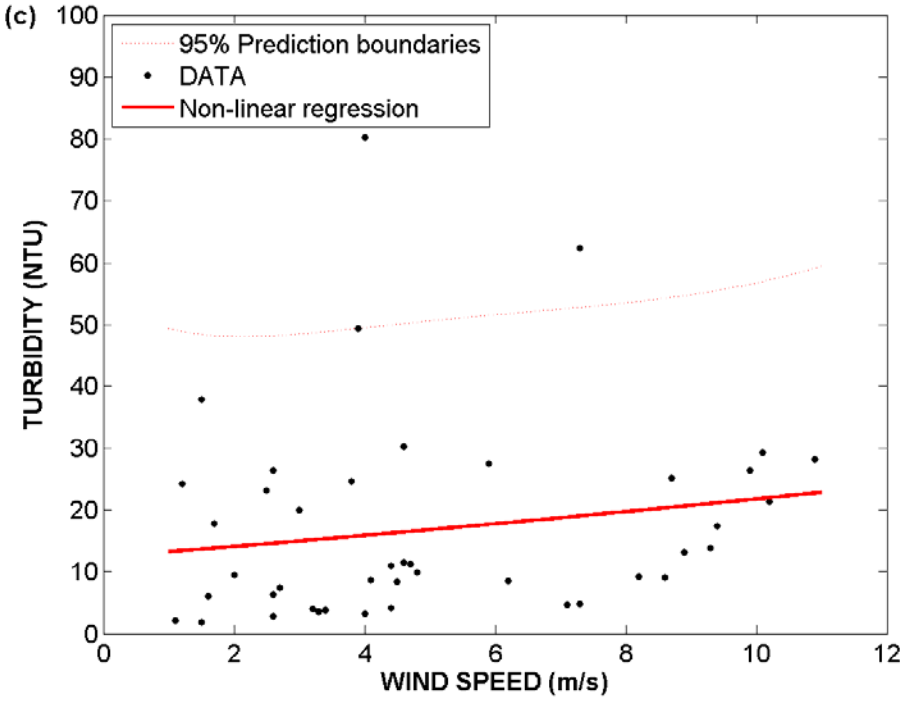

Figure 3.22 (continued) Non-linear regressions at the three stations between turbidity (NTU) and wind speed (m s^{-1}) with 95% prediction boundaries. Red lines indicate non-linear regression and black dots indicate data points: (a) Station 4 m; (b) Station 6 m bottom; (c) Station 8 m.

Data from the two stations, Station 4 m and Station 6 m bottom, and the non-linear (power) regressions are shown in Figure 3.23. Two other regressions in which the exponents are fixed at 4 and 5 reflect the powers given by the equations of Mian and Yanful (2004) and García and Parker (1991; 1993), respectively. Their formulae coefficients are listed in Table 3.3 as well. It is clear that the non-linear regression and the regression for a fixed exponent equal to 5 produce similar representations of the data points, considering the natural scatter related to sediment phenomena. The close fit suggests that the resuspended sediments due to the bed shear stress exceeding the critical shear stress in the Salton Sea behave mostly as non-*cohesive* sediments. However, sediment entrainment rates for *cohesive* sediments were also described by the power relation as a function of the excess bed shear stress (Maa et al., 1998).

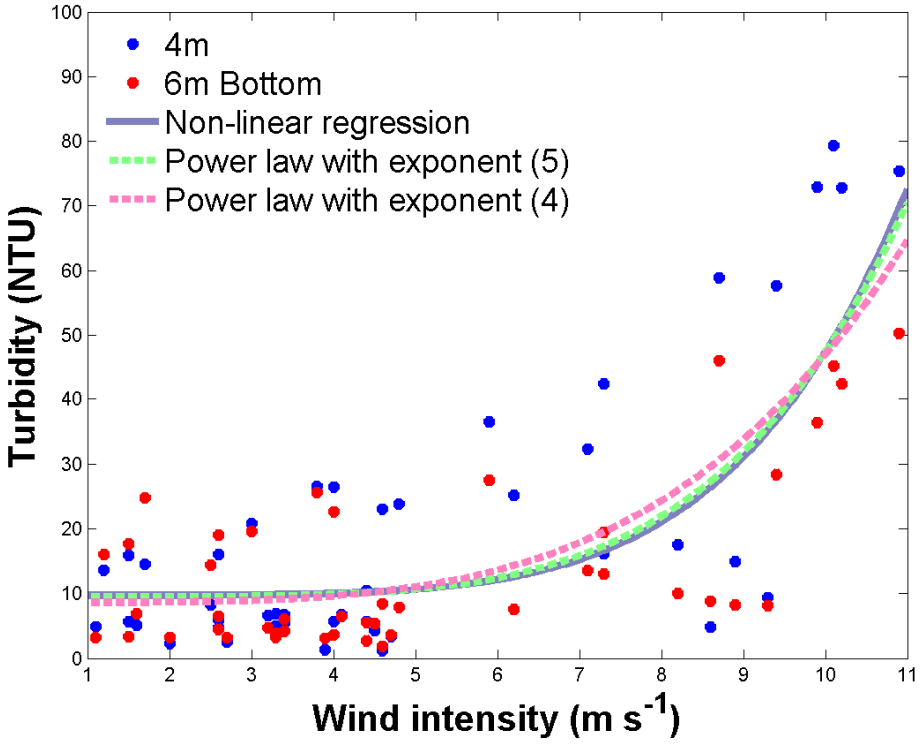

Figure 3.20 Comparison of regressions of turbidity (NTU) and hourly wind speed (m s^{-1}) from CIMIS Station 128 at two bottom stations, Stations 4 m (blue dots) and 6 m bottom (red dots), with the non-linear (power) regression (R) (gray line), the regression of power 4 (4) (pink dash line), and the regression of power 5 (5) (green dash line).

COMPUTATION OF SEDIMENT RESUSPENSION

In this section, sediment resuspension was simulated from bed shear stress using sediment resuspension models. Bed shear stresses due to wind-induced currents and waves were also calculated and examination made of the possible influence of seiches on sediment suspension. In addition, the Sverdrup-Munk-Bretschneider (SMB) method for transitional or shallow water bodies (CERC, 1984) is applied to calculate wave characteristics for the estimation of bed shear stress due to wind-induced waves.

Computation of wave characteristics

A wave model widely used for many years was applied. The SMB model was used to calculate the wave characteristics in the Salton Sea. The effective fetch for each observation station was calculated at 30 km as previously discussed (see Chapter 2). The simulated wave heights and periods, assuming water depth of the Sea as 12 m, are

compared with the observed values from August 8, 2005 to September 18, 2005 in Figure 3.24. It corroborates that the model is able to predict significant wave heights and periods accurately enough to be used for the computation of bed shear stress.

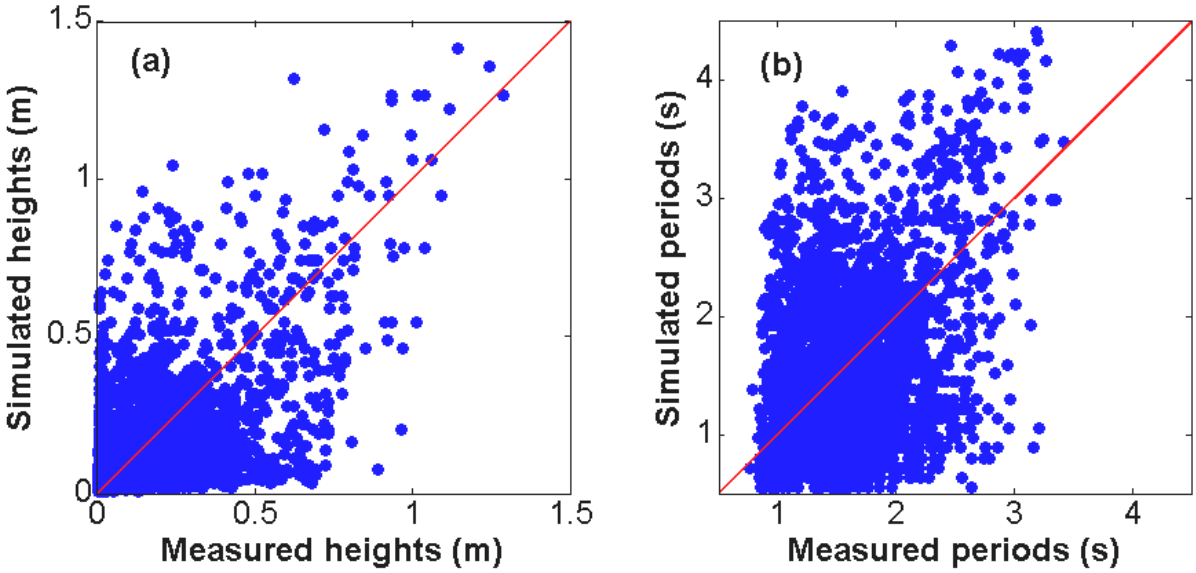

Figure 3.21 Comparison between measured and simulated wave characteristics in the observation area from August 6, 2005 to November 26, 2005: (a) significant wave height (m); (b) wave period (seconds).

Computation of bed shear stresses

Bed shear stresses due to wind-induced currents and waves are calculated using Equation (2.8) and Equation (2.9), respectively. For the computation of bed shear stresses, the density of air, water and kinematic viscosity of water values discussed in Chapter 2 were used.

Bed shear stresses (Pa) generated by wave and currents in the observation area computed from data collected are compared in Figure 3.25. Wind speeds were extrapolated from 2 m to 10 m using the semi-logarithmic velocity law (Cook, 2000). As expected, calculated shear stresses induced by waves are greater than those calculated due to currents by about 10 times. Shear stresses by waves dominating those of currents are usually found in other shallow lakes as well (Hamilton and Mitchell, 1996; Luettich et al., 1990; Mian and Yanful, 2004). Examination of Figure 3.25 also shows the critical shear stress, 6.25×10^{-2} Pa, estimated by Equations (2.5) – (2.6) for a sediment size of 25 μm.

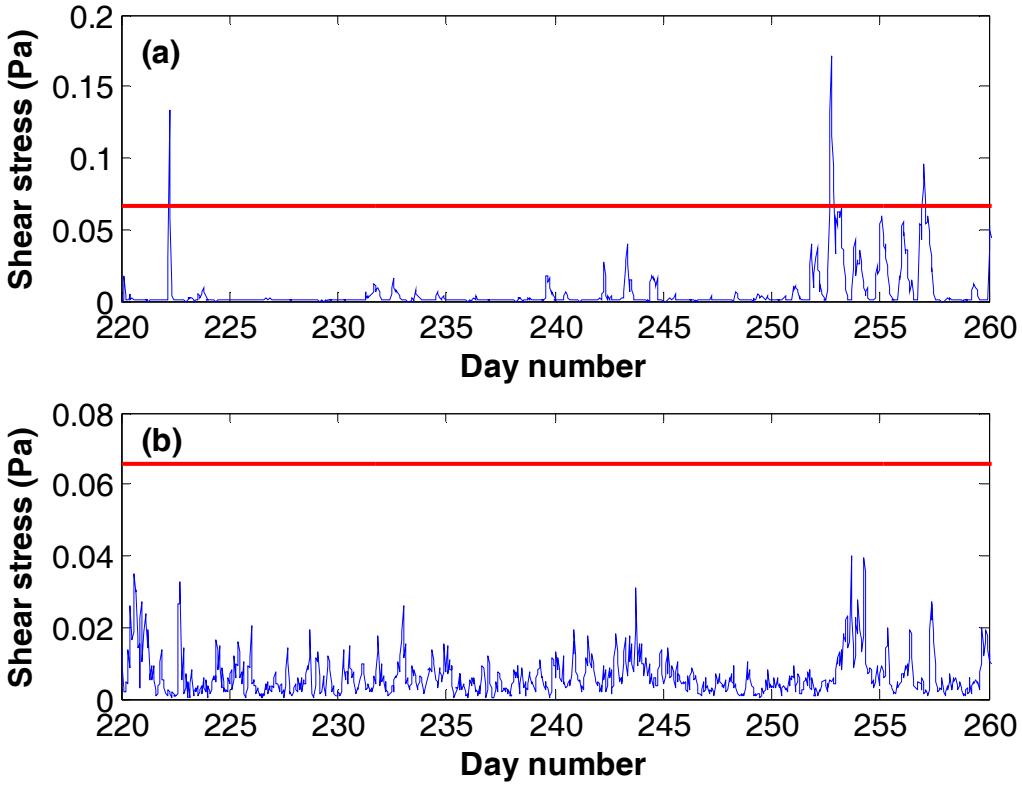

Figure 3.22 Comparison between bed shear stresses (Pa) generated by (a) wave and (b) currents in the observation area computed from data collected by AWAC. The plots also include the critical shear stress, red lines, (Pa) for incipient motion corresponding to an average particle size of 25 μm.

A comparison of the simulated to the calculated bed shear stresses generated by waves was made in Figure 3.26. The difference between the simulated and the measured wave characteristics may have an influence on the computation of the bed shear stresses; however, the simulated bed shear stress from the wave characteristics modeled by the SMB model agree well with those calculated from measured wave characteristics.

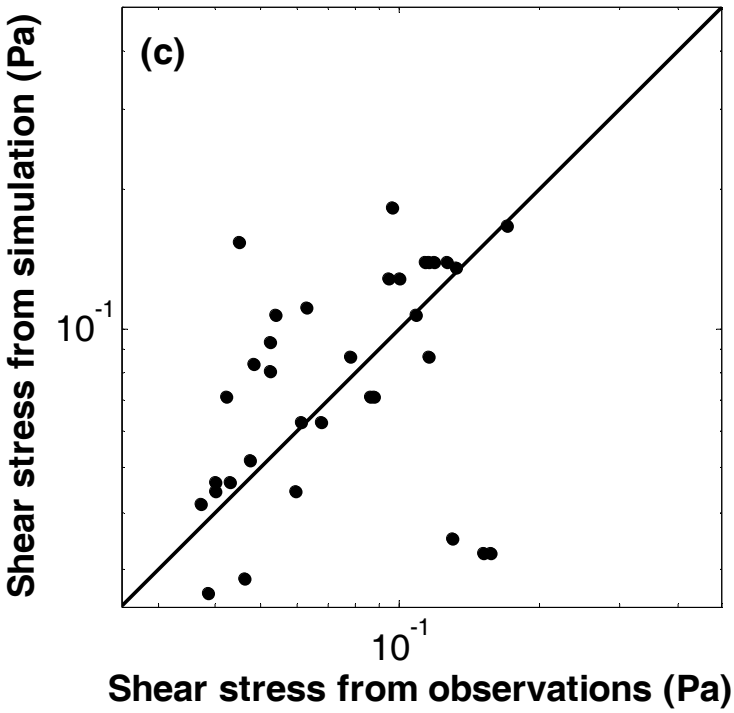

Figure 3.23 Comparison between measured and simulated shear stress induced by waves exceeding the critical shear stress.

Occurrence of surface seiches

Since there was no severe stratification during the observation period, the potential occurrence of seiches at the surface in the Salton Sea was examined. Wavelengths (λ_{Seiche}) and angular frequencies (ω_{Seiche}) of seiches in the Sea are estimated using the following simple relations, which are valid for idealized conditions (Kundu and Cohen, 2002):

$$\lambda_{Seiche} = \frac{2\,L}{n+1}; \qquad n = 0, 1, 2, ... \tag{3.4}$$

$$\omega_{Seiche} = \sqrt{\frac{\pi\ g\ (n+1)}{L}\ \tanh\left(\frac{(n+1)\,\pi\ H}{L}\right)}; \qquad n = 0, 1, 2, ... \tag{3.5}$$

where L is the length of the lake and n refers to the normal mode of the seiche; Equation (3.5) is the well-known dispersion relationship. Using the two main lengths of the lake, Equations (3.4) and (3.5) yield wavelengths of 112 and 48 km for the first mode ($n = 0$), and 56 and 24 km for the second mode ($n = 1$). These values correspond to frequencies of 8 x 10^{-5} and 2 x 10^{-4} Hz for the first mode and 1.76 x 10^{-3} and 4 x 10^{-4} Hz for the second mode, respectively.

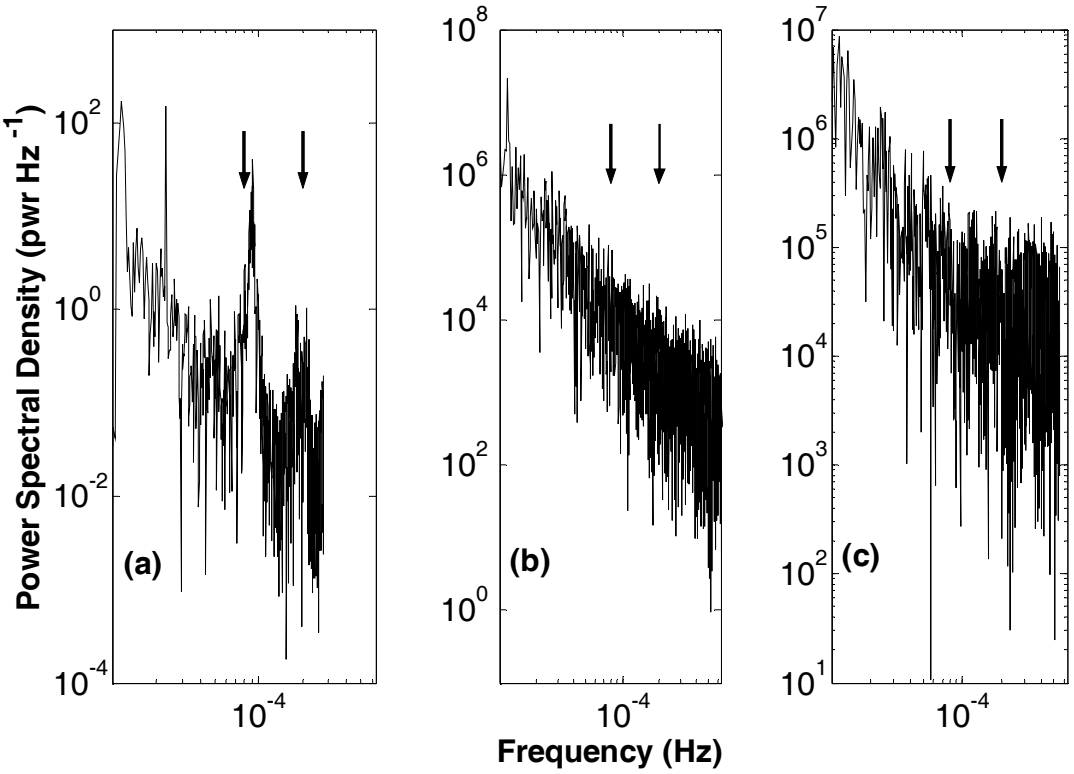

Figure 3.**27** Power spectral density (power Hz^{-1}) of diverse datasets from August 7, 2005 to September 17, 2005: (a) pressure (m); (b) signal strength (count) from AWAC at 1.8 m from the bottom; (c) turbidity (NTU) at station 4 m. We have indicated in the figure the theoretical values of frequency for the first mode of seiches. The two arrows in each subplot indicate the frequencies of 8 x 10-5 and 2 x 10-4 Hz corresponding to the first mode wavelengths calculated using Equation (3.5).

In order to assess the occurrence of seiches corresponding to the above (or even similar) frequencies, we compute the power spectrum density (PSD) for the pressure signal obtained from the AWAC for the period August 7, 2005 to September 17, 2005, and for the current speed at 1.8 m from the bottom and turbidities at Station 4 m, during the same observation period as shown as Figure 3.27. There is a obvious occurrence of peaks in the pressure signal power spectrum at frequencies similar to those computed for the first mode wavelengths, which suggests that the Salton Sea had surface seiches during the sampling period. The peaks do not appear on the power spectrum of current speed or turbidity, likely indicating a low influence of these surface seiches on currents or concentrations of suspended sediments.

Computation of sediment resuspension

The value of Re_p calculated using the approximate sediment size of 25 μm is less than 1, which is outside the limits of application of the García and Parker (1993) formula ($1 < \mathrm{Re}_p < 3$). In this research, the formula of García and Parker is extended so that it can cover the range of variables found for the Salton Sea. Toa ccomplish this, observations reported in Figure 14 of the paper by García and Parker (1993) which relates f with Re_p, to values of Re_p smaller than 1 but larger than 0.4 were extrapolated. The estimate (dashed line) is shown in Figure 3.28. The relationship: $f\left(\mathrm{Re}_p\right) = \mathrm{Re}_p^{3.75}$ (for $0.4 < \mathrm{Re}_p < 1$) was developed which provides a smooth extrapolation of the measured data.

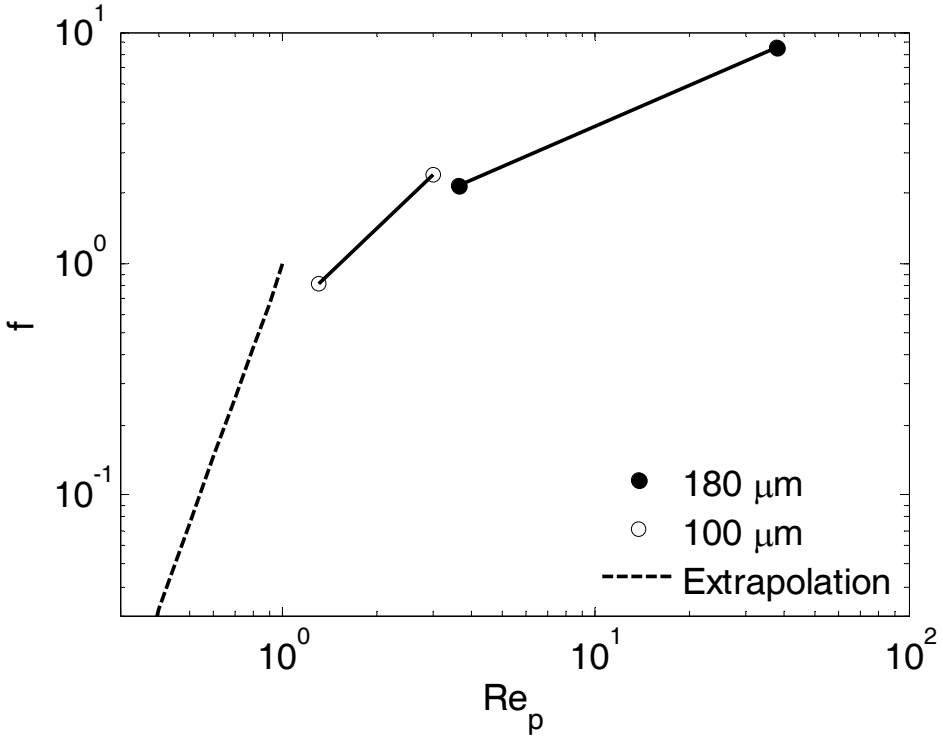

Figure 3.28 Extrapolation of measurements of García and Parker (1993) for Re_p values smaller than 1 and larger than 0.4. Circles indicate the measured points by García and Parker, and the dashed line indicates the extrapolation proposed in this paper.

Sediment entrainment rates driven by the measured wave characteristics developed from the AWAC data were calculated using Equation (2.4) and the extended García and Parker formulation, since wind-induced waves play a dominant role in the sediment resuspension. For the computation of Equation (2.4), the critical shear stress, τ_{cr}, and the exponent, m, are assumed to be the same values as 0.058 Pa and 2, respectively, from Mian and Yanful (2004), while the coefficient, α, is equal to 6.0×10^{1}.

For the Equation (2.3), the sediment size and density were selected as 25 μm and 2.65 g cm^{-3}, respectively, described in detail in Chapter 2.

Simulated sediment entrainment rates were compared with those estimated by the measured wave characteristics. Comparison is shown in Figure 3.29 of the simulated (blue lines) and the estimated sediment entrainment rates by measured data (red lines). Both the *cohesive* and non-*cohesive* sediment models show similar patterns. For example, both models simulate high sediment entrainment rates at days 252 – 253, 256 – 257, 281 – 282 and 288 – 289 although they cannot capture a peak at around day 225.

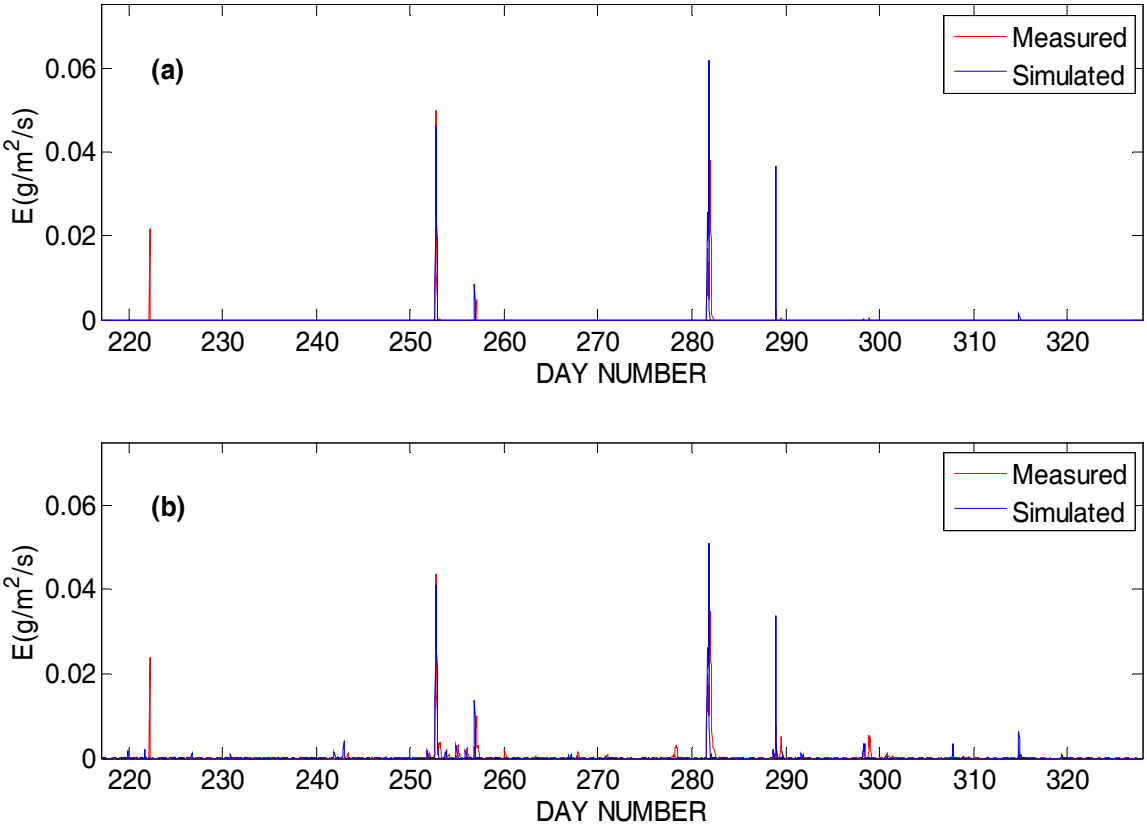

Figure 3.24 Comparison between the calculated sediment entrainment rate driven by the measured wave characteristics (red lines) and the simulated (blue lines) from August 5, 2005 to November 24, 2005: (a) Sediment entrainment rate simulated by Mian and Yanful (2004); (b) Sediment entrainment rate simulated by Garcia and Parker (1991; 1993).

Examination of Figure 3.30 (a) and (b) shows two simulated concentrations of suspended sediment using Equation (2.4) and the extended Garcia and Parker formulation. In Figure 3.30 (c) the turbidity is simulated by the non-linear regression for the case of three stations. In Figure 3.30 (d) turbidity data collected at Stations 4 m is presented. Examination of the figure reveals an acceptable agreement of all models with

the measured data showing peaks about at day 253, even though the unit of turbidity (NTU) is different from that of sediment concentration (g L^{-1}).

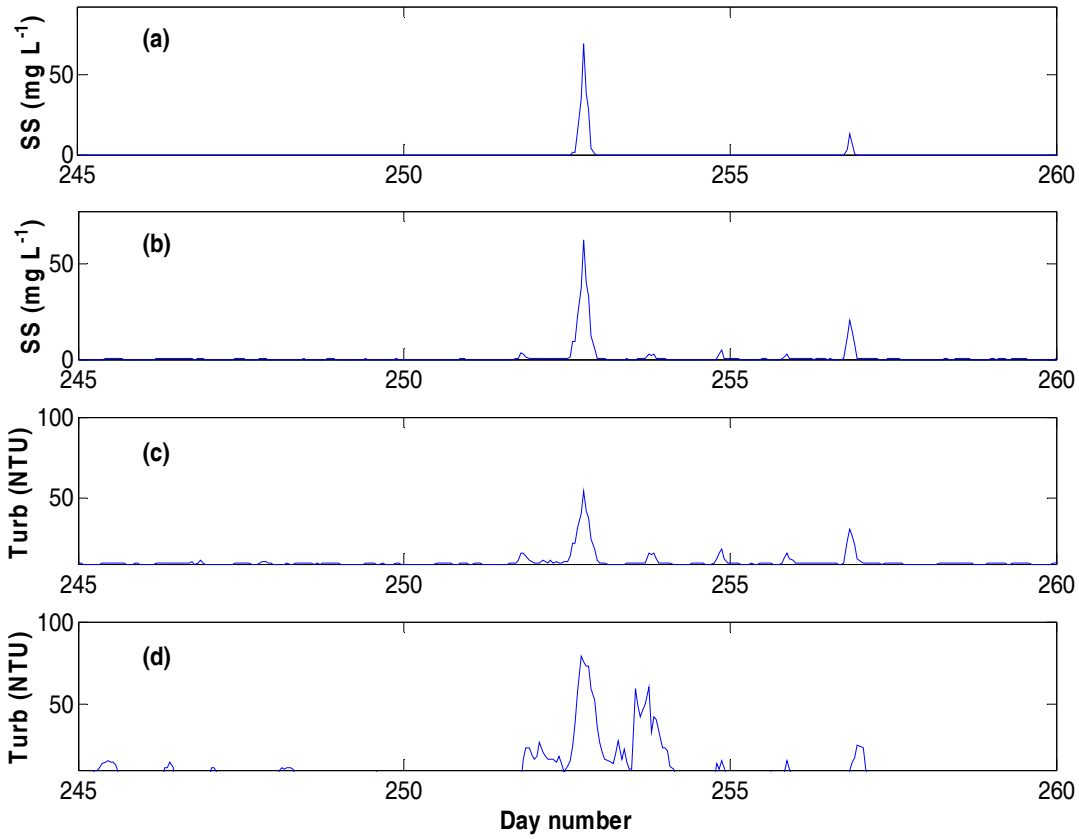

Figure 3.25 Comparison of simulated and inferred sediment entrainment into suspension at the bottom of the 4-m station: (a) Suspended sediment concentration (SS) simulated using Equation (2.4); (b) suspended sediment concentration (SS) simulated using the expression of the extended García and Parker; (c) simulated turbidity (Turb) using the non-linear regression (NTU); (d) measured turbidity (Turb) at the 4-m station (NTU).

References

Akiyama, J., and Fukushima, Y. 1986. Entrainment of noncohesive sediment into suspension, p. 804-813. *In* Wang, S. Y., Shen, H. W. and Ding, L. Z. [eds.], 3rd International Symposium on River Sedimentation.

Arulanandan, K. 1975. Fundamental Aspects of Erosion of Cohesive Soils. Journal of the Hydraulics Division-ASCE **101:** 635-639.

Celik, I., and Rodi, W. 1984. A deposition entrainment model for suspended sediment transport. Universitat Karlsruhe.

Cook, C. B. 2000. Internal dynamics of terminal basin lake: A numerical model for management of the Salton Sea. Ph.D. dissertation. University of California.

Cook, C. B., Orlob, G. T., and Huston, D. W. 2002. Simulation of wind-driven circulation in the Salton Sea: implications for indigenous ecosystems. Hydrobiologia **473:** 59-75.

Dedeckker, P., and Williams, W. D. 1988. Physicochemical Limnology of 11, Mostly Saline Permanent Lakes in Western Victoria, Australia. Hydrobiologia **162:** 275-286.

Earle, M. D. 1996. Nondirectional and Directional Wave Data Analysis Procedures. NOAA.

Freire, P., and Andrade, C. 1999. Wind-induced sand transport in Tagus estuarine beaches – First results. Aquatic Ecology **Volume 33:** 225-233.

García, M. 1999. Sedimentation and Erosion Hydraulics. *In* Mays, L. W. [ed.], Hydraulic Design Handbook. McGraw-Hill.

García, M., and Parker, G. 1991. Entrainment of Bed Sediment into Suspension. Journal of Hydraulic Engineering-Asce **117:** 414-435.

García, M., and Parker, G. 1993. Experiments on the Entrainment of Sediment into Suspension by a Dense Bottom Current. Journal of Geophysical Research-Oceans **98:** 4793-4807.

Gloor, M., Wuest, A., and Munnich, M. 1994. Benthic Boundary Mixing and Resuspension Induced by Internal Seiches. Hydrobiologia **284:** 59-68.

Hamilton, D. P., and Mitchell, S. F. 1996. An empirical model for sediment resuspension in shallow lakes. Hydrobiologia **317:** 209-220.

Hawley, N., Lesht, B. M., and Schwab, D. J. 2004. A comparison of observed and modeled surface waves in southern Lake Michigan and the implications for models of sediment resuspension. Journal of Geophysical Research-Oceans **109**.

Kamphuis, J. W. 1975. Friction factor under oscillatory waves. Journal of the Waterways Harbors and Coastal Engineering Division **101**.

Kandiah, A. 1974. Fundamental aspects of surface erosion of cohesive soils. Ph.D. dissertation. University of California, Davis.

Kundu, P. K., and Cohen, I. M. 2002. Fluid Mechanics. Academic Press.

Lohrmann, A. 2001. Monitoring Sediment Concentration with acoustic backscattering instruments, p. 5 pages. Nortek AS.

Luettich, R. A., Harleman, D. R. F., and Somlyody, L. 1990. Dynamic Behavior of Suspended Sediment Concentrations in a Shallow Lake Perturbed by Episodic Wind Events. Limnology and Oceanography **35:** 1050-1067.

Maa, J. P. Y., Sanford, L., and Halka, J. P. 1998. Sediment resuspension characteristics in Baltimore Harbor, Maryland. Marine Geology **146:** 137-145.

Mehta, A. J. 1981. Review of erosion function for cohesive sediment beds, p. 122-130. First Indian Conference on Ocean Engineering.

Mian, M. H., and Yanful, E. K. 2004. Analysis of wind-driven resuspension of metal mine sludge in a tailings pond. Journal of Environmental Engineering and Science **3:** 119-135.

NOAA. 2006. How are significant wave height, dominant period, and wave steepness calculated? http://www.ndbc.noaa.gov/wavecalc.shtml.

Nortek. 2004. AWAC User Guide.

Osborne, P. D., and Greenwood, B. 1993. Sediment Suspension under Waves and Currents - Time Scales and Vertical Structure. Sedimentology **40:** 599-622.

Robarts, R. D., Zohary, T., Jarvis, A. C., Paismadeira, C. M., Sephton, L. M., and Combrink, S. 1992. Phytoplankton and Zooplankton Population-Dynamics and Production of a Recently Formed African Reservoir. Hydrobiologia **237:** 47-60.

Sanford, L. P., and Maa, J. P. Y. 2001. A unified erosion formulation for fine sediments. Marine Geology **179:** 9-23.

Schladow, S. G., Robertson, D. M., Hook, S. J., Chung, E. G., Losada, J. P., Cardona, B. M., Palmarsson, S. O., Steissberg, T. E., and Fleenor, W. E. 2004. Salton Sea Nutrients TMDL Modeling Studies. Colorado River Basin Regional Water Quality Control Board.

Sheng, Y. P., and Lick, W. 1979. Transport and Resuspension of Sediments in a Shallow Lake. Journal of Geophysical Research-Oceans and Atmospheres **84:** 1809-1826.

Smith, J. D., and McLean, S. R. 1977. Spatially Averaged Flow over a Wavy Surface. Journal of Geophysical Research-Oceans and Atmospheres **82:** 1735-1746.

Strehlow, K., Davis, J., Sim, L., Chambers, J., Halse, S., Hamilton, D., Horwitz, P., McComb, A., and Froend, R. 2005. Temporal changes between ecological regimes in a range of primary and secondary salinised wetlands. Hydrobiologia **552:** 17-31.

Thorn, M. F. C., and Parsons, J. G. 1980. Erosion of cohesive sediments in estuaries: An engineering guide, p. 349-358. *In* Stephens, H. S. [ed.], 3rd International Symposium on Dredging Technology, BHRA.

Van Rijn, L. C. 1984. Sediment Transport .2. Suspended-Load Transport. Journal of Hydraulic Engineering-ASCE **110:** 1613-1641.

Zyserman, J. A., and Fredsoe, J. 1994. Data-Analysis of Bed Concentration of Suspended Sediment. Journal of Hydraulic Engineering-ASCE **120:** 1021-1042.

CHAPTER 4: DYNAMIC LAKE MODEL – WATER QUALITY (DLM-WQ)

DML-WQ is a one-dimensional model that simulates the vertical distribution of temperature, salinity and water quality in small- to medium-size lakes and reservoirs (Hamilton and Schladow, 1997; Losada, 2001; McCord, 1999; Schladow and Hamilton, 1997). It is based on an earlier series of reservoir models, DYRESM, developed at the Centre for Water Research (CWR) at the University of Western Australia (Hamilton and Schladow, 1997; Imberger and Patterson, 1981; Imberger, 1978). The assumption of one dimensionality means that variations in density, temperature, and water quality parameters in the lateral directions are assumed to be small when compared with variations in vertical directions. The water quality model, DLM-WQ, couples the hydrodynamic processes, such as the transport and mixing, to a set of biological and chemical processes that describe the growth of phytoplankton, the cycling of nutrients and the fate of particulate material.

MODEL STRUCTURE

The vertical profile of the lake is represented as a set of Lagrangian layers, which are free to move vertically and to contract and expand in response to inflows, outflows, and surface-mass fluxes. The Lagrangian formulation avoids the need to calculate vertical velocities, greatly decreasing computational time and minimizing numerical diffusion, as compared with a fixed-grid Eulerian approach. Each layer is homogeneous, and property differences between layers represent the vertical distribution (Figure 4.1). Layer thickness is adjusted within the model according to the resolution required to represent the vertical density gradient. Each layer in the model is initialized with measured data.

Mixing is represented by the amalgamation of layers. Thus, for example, when wind mixing has produced sufficient turbulent kinetic energy to overcome the potential energy difference (density stratification) of the two upper layers, the two layers are simply combined. Properties of the amalgamated layer are volumetrically averaged, and the total number of model layers is decreased accordingly. Amalgamated layers may be split according to a specified maximum-layer thickness criterion, thereby maintaining the desired spatial resolution. Conversely, when a layer size falls below a specified minimum criterion, as may occur when there is withdrawal of water from the lake, then the layer is amalgamated with the smaller of the two bounding layers. Inflows are inserted at their level of neutral buoyancy after allowance for entrainment has been made. In the case of the Salton Sea, where the tributary flows are much fresher than the Sea water, the inflow spreads on the surface until it is mixed with the bulk of the surface layer (Schladow et al., 2004).

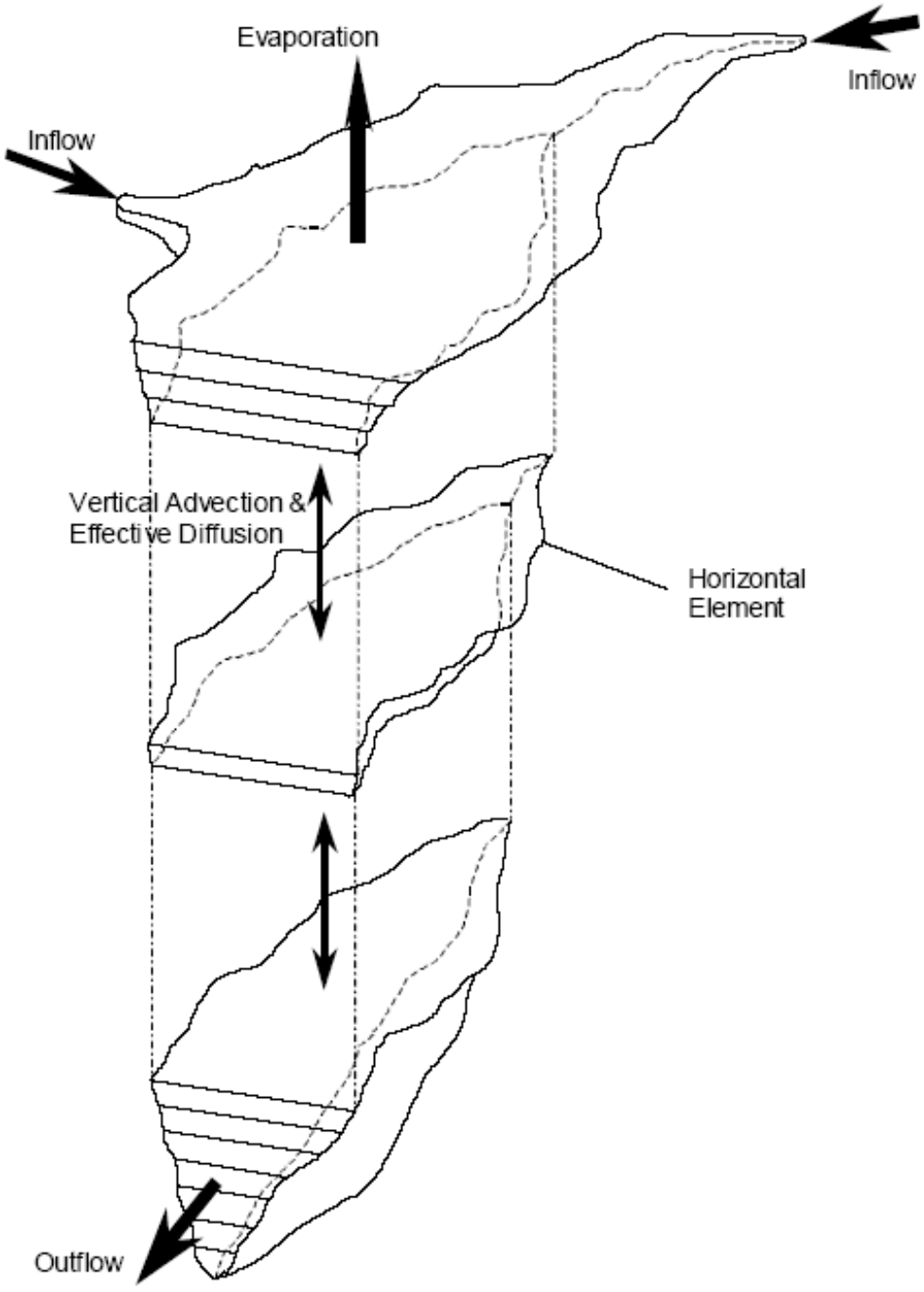

Figure 4.1 Schematic model structure of one-dimensional DLM-WQ model showing horizontal layers and the major internal and external forcing functions used in the model, such as inflow, outflow, evaporation and vertical advection and diffusion.

PHYSICAL PROCESSES

The basic model is driven by five processes, including surface heat, mass and momentum exchange, convective overturn, stirring, shear production and billowing. Additional processes (for example, sediment resuspension in the case of the Salton Sea model) are included for shallow lakes.

Surface heat, mass, and momentum exchange

The surface inputs of mass, heat and momentum play a major role in determining the vertical distribution of properties in a water body. The model relies on the bulk aerodynamic formulae to calculate these transfers based on measured meteorological data. These are stress, τ , sensible heat transfer, H , and evaporative heat transfer, E :

$$\tau = \rho C_D U^2 \tag{4.1}$$

$$H = -\rho C_P C_H (T_A - T_S) \tag{4.2}$$

$$E = -\rho L_V C_W (q_A - q_S) \tag{4.3}$$

where U is wind speed; T is air temperature; q denotes specific humidity, with the subscript A referring to the air value, and S to the surface value; C_D, C_H, and C_V are bulk aerodynamic transfer coefficients; C_P and L_V denotes specific heat of water at constant pressure and the latent heat of evaporation of water, respectively. Density of the Salton Sea is calculated using the UNESCO equation for seawater, which is applicable up to a salinity of between 42 and 50 parts per thousand (Poisson et al., 1991). Although the Salton Sea has a different chemical composition from seawater, deviations in density are likely to be insignificant (Schladow et al., 2004).

Radiative heat transfers are also an important component of the heat budget at the surface. The model considers short wave (wavelength 100 nm to 4000 nm), and long wave (wavelength greater than 4000 nm) radiation. Short wave radiation is usually measured directly, and the long wave LW_I either measured directly or estimated from cloud cover, air temperature, and humidity. Back radiation from the water surface is given by the Stefan-Boltzmann black body radiation law:

$$LW_O = \sigma T_K^4 \tag{4.4}$$

where T_K is water temperature in ^{o}K and σ is Stefan-Boltzmann constant.

Some of the incoming short wave radiation is reflected from the surface, with a reflection coefficient, or albedo, determined by the angle of the sun, the color of the water, or the state of the water surface. The shortwave radiation penetrates the water surface and is absorbed by the water column. In general, the absorption is determined by an attenuation coefficient which will depend on the wavelength, water clarity and color. This absorption is often calculated in DLM-WQ by a Beer's Law formulation:

$$Q(z) = Q_0 e^{-\eta z} \tag{4.5}$$

where Q_0 is radiation intensity at the surface, and $Q(z)$ is intensity at depth z and η denotes attenuation coefficient. The attenuation coefficient may be related to the Secchi Disk depth, d_S, (Chapra, 1997):

$$\eta \sim \frac{1.8}{d_S} \tag{4.6}$$

In DLM-WQ, the attenuation coefficient is related to the chlorophyll *a* concentration, suspended sediment concentration and a background attenuation coefficient (to allow for absorption by water and particle scattering). The long wave radiation is all absorbed in the first few mm of the water column.

In the context of the layer structure of DLM-WQ, the heat budget may be expressed as shown in Figure 4.2. Only the top layer is affected by evaporative heat losses, sensible heat losses or gains, and long wave input and emission. Short wave radiation enters and provides a source of heat for lower layers, following Beer's Law.

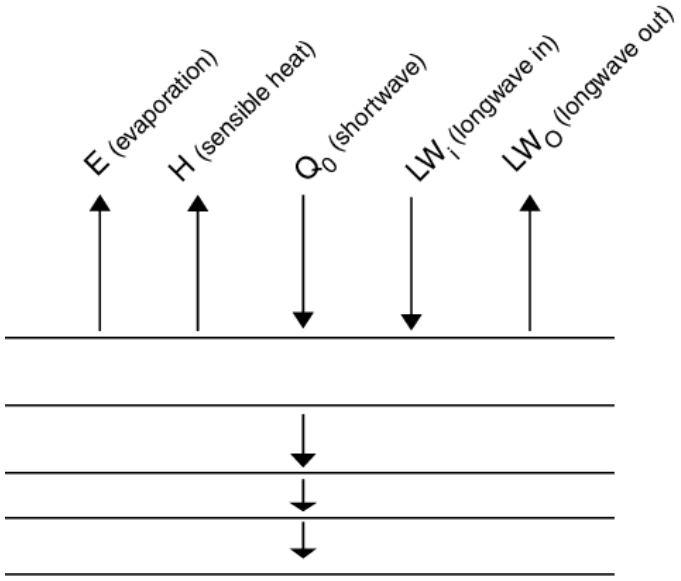

Figure 4.1 Schematic of heat flux through DLM-WQ layers.

If all of the fluxes are specified in units of Joules m^{-2} sec^{-1}, the net temperature increase of the top layer is given by:

$$\Delta T \frac{\left[A_S\left(LW_I - LW_o - E - H + Q_0\right) - A_{S-1} Q_0 e^{-\eta d_s}\right]\Delta t}{\rho V_S C_P} \tag{4.7}$$

where A_S and A_{S-1} are areas of the surface and penultimate layers, respectively; V_S is surface layer volume; d_S is upper layer thickness; Δt denotes time step in seconds. The time step for the model is specified in the initial menu; in particular, a 3 hour timestep was found to be satisfactory in the case of the Salton Sea.

After a single time step, the temperature structure will change as the result of the surface heat exchanges, as shown in Figure 4.3. Note that after cooling, the surface layer is cooler than the underlying layer, an unstable configuration. This will be dealt with by the mixed layer algorithm. The cooling profile shown also has sub-surface heating, corresponding to the absorption of shortwave radiation. Night cooling would leave the underlying layers unchanged.

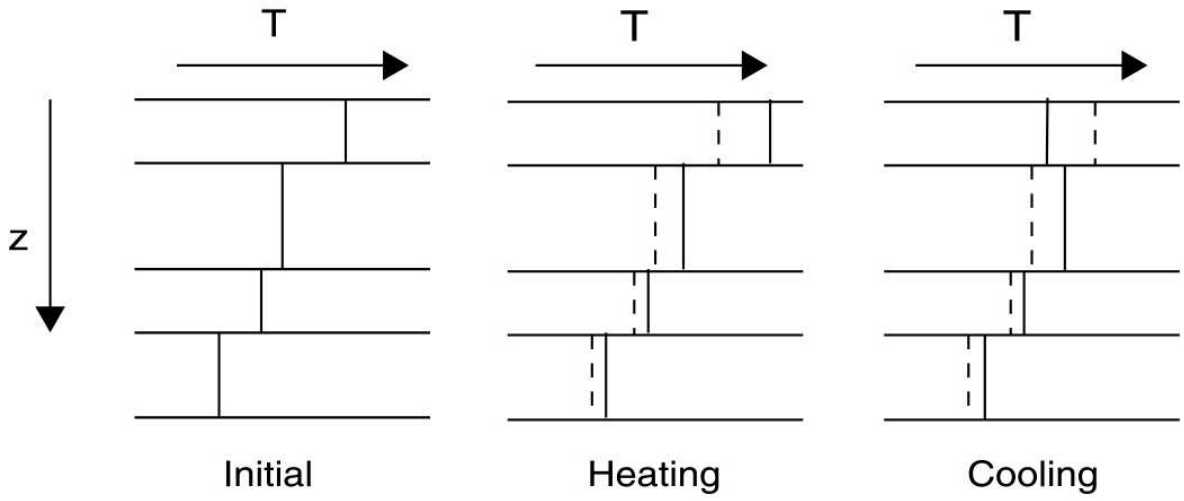

Figure 4.2 Schematic of the effects of heating and cooling on layer stability.

The algorithm which describes the deepening of the surface layer is based on an integral model of the turbulent kinetic energy budget. Here, a certain fraction of the energy made available at the surface and at the interface between the mixed layer and the underlying water is made available to lift and accelerate the quiescent and relatively heavy water below the interface into the mixed layer. This may be achieved in several ways, e.g. convective overturn, stirring, shear production and billowing.

Convective overturn

Cooling of the surface, as described above, leaves the temperature profile in an unstable state, with cooler water overlying warmer water. In reality, this cool and dense water will plunge in a turbulent plume, mixing with the water beneath. This process is modeled by a simple readjustment of the profile; that is, the surface layer density is compared with the density of the layer below and the two are mixed if gravitational instability exists. The resultant layer density is checked against the next layer, and the process repeated until the profile is stable, as shown in Figure 4.4. In making this

adjustment, the center of mass has been moved downwards, which implies that additional energy becomes available for further mixing. This may be expressed in terms of a velocity scale, w_*. This energy is retained for the next process.

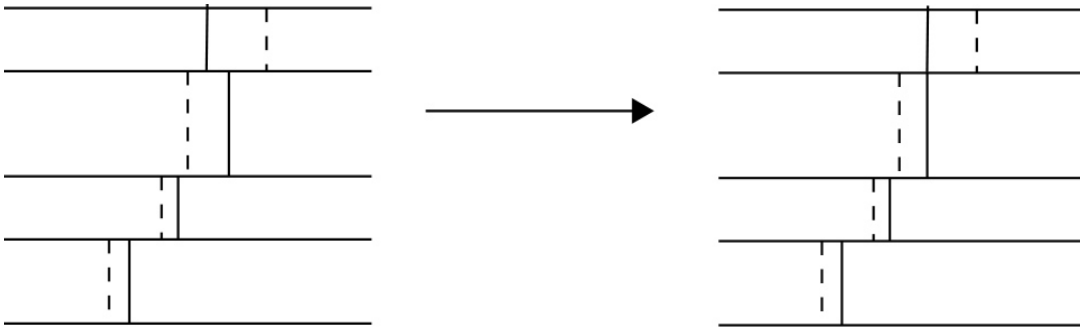

Figure 4.3 Schematic of the effects of surface layer deepening by cooling.

Stirring

Some fraction of the energy input to the surface by wind at the surface is available at the interface for mixing. The surface stress is given by

$$\tau = \rho_a C_D U^2 = \rho u_*^2 \tag{4.8}$$

which provides a means of calculating the energy input. The work per unit area by the wind is then

$$\tau u_* \Delta t = \rho u_*^3 \Delta t \tag{4.9}$$

The energy input from the convective overturn component discussed above may be included, to give

$$AKE = \frac{C_K}{2} \rho \left(w_*^3 + \eta^3 u_*^3 \right) \Delta t \tag{4.10}$$

where AKE denotes available turbulent kinetic energy; η is a parameter which reflects the relative efficiencies of the convective overturn and wind stirring mechanisms; C_K is a parameter which reflects the efficiency of the stirring process relative to other processes.

Shear production

The action of the surface wind field, in addition to providing energy for deepening of the mixed layer, generates a shear velocity u_1 at the interface. As the interface deepens over δh, conservation of momentum requires that the new shear velocity becomes

$$u_2 = \frac{hu_1}{h+\delta h} \tag{4.11}$$

In the change from u_1 to u_2, the total kinetic energy reduces by an amount

$$hu_1^2 - (h+\delta h)u_2^2 \tag{4.12}$$

where the small change in density is negligible. This energy becomes available for further mixing, and is added into the AKE generated by stirring. Thus, the energy per unit mass is

$$AKE = \frac{C_K}{2}\left(w_*^3 + \eta^3 u_*^3\right)\Delta t + \frac{C_S}{2}u_1^2\delta h \tag{4.13}$$

where C_S is a parameter which reflects the relative efficiency of the shear production mechanism.

To operate the shear production mechanism, a value for the shear velocity is required. This is obtained from the simple model:

$$\begin{aligned} u_1 &= \frac{u_*^2 t}{h} + u_{1_0} \qquad t < t_{eff} \\ &= 0 \qquad\qquad\quad t > t_{eff} \end{aligned} \tag{4.14}$$

where t_{eff} is time beyond which shear production is no longer operative. The cut off time assumes use of only the energy produced by shear at the interface during the first wave period T_i, determined from the stratification, and modified to account for damping. The cut off time may extend beyond one model time step, and the wind stress may change over the period of t_{eff}. The calculation of shear production is therefore a complex matter.

The energy available for mixing, S, expressed as a rate of available energy AKE, is used to deepen the mixed layer. This means lifting relatively heavy water, and accelerating stationary water, both of which require energy. Thus the simplest mixed layer model balances the energy requirement with the available energy. Consider a mixed layer of depth, h, and density, ρ_0, with a density jump of $\Delta\rho$ at the base, which becomes mixed over a distance, δh, as shown in Figure 4.5.

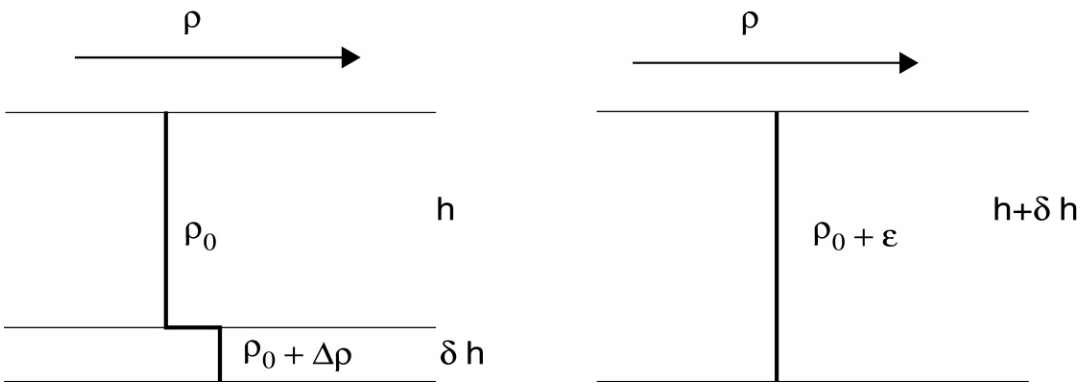

Figure 4.4 Schematic of process of deepening.

The kinetic energy requirement is therefore:

$$\frac{C_T}{2}\rho\left(w_*^3+\eta^3u_*^3\right)^{2/3}\delta h \tag{4.15}$$

The energy requirement per unit mass is therefore:

$$SPE=\left[\frac{C_T}{2}\left(w_*^3+\eta^3u_*^3\right)^{2/3}+\frac{g\Delta\rho h}{2\rho_0}\right]\delta h \tag{4.16}$$

Billowing

The presence of shear at the interface may lead to a shear instability providing additional mixing. The effect of this is the formation of Kelvin-Helmholtz billows, which smear out the sharp interface generated by stirring and shear production. The scale of the billows is given by

$$\delta=\frac{0.3\rho_0u_1^2}{g\Delta\rho} \tag{4.17}$$

These provide both a source and a sink for energy, and therefore should appear on both sides of the energy balance.

$$AKE=\frac{C_K}{2}\left(w_*^3+\eta^3u_*^3\right)\Delta t+\frac{C_S}{2}\left[u_1^2+\frac{u_1^2d\delta}{6\,dh}+\frac{u_1\delta du_1}{3\,dh}\right]\delta h \tag{4.18}$$

$$SPE=\left[\frac{C_T}{2}\left(w_*^3+\eta^3u_*^3\right)^{2/3}+\frac{g\Delta\rho h}{2\rho_0}+\frac{g\delta^2\,d(\Delta\rho)}{24\rho_0\,dh}+\frac{g\Delta\rho\delta}{12\rho_0}\frac{d\delta}{dh}\right]\delta h \tag{4.19}$$

Energy balance

In general, the balance between the available energy, AKE, and the required energy, SPE, provides an equation for the deepening rate dh/dt. In the context of DLM-WQ, where the time step, Δt, is determined elsewhere and δh is constrained to be a layer thickness, the following procedure is applied in simplified form. For each time step, AKE is calculated, based on the existing mixed layer of depth, h, and w_* and u_* determined as above, after adjustment of the profile following surface cooling. Required SPE is then calculated to mix in the next layer, of thickness, δh, and density, $\rho_0 + \Delta\rho$. If $AKE > SPE$, the layer is mixed, the mixed layer properties adjusted, AKE reduced by an amount SPE, and the next layer considered. If $AKE < SPE$, the energy AKE is not utilized, but is stored for use in the following time step. As the model takes each process in turn, the actual procedure is slightly more complex, but essentially follows the same path.

Mixing below the surface layer

Mixing in the hypolimnion of lakes is patchy and sporadic, with individual events occupying relatively small volumes and occurring relatively quickly. However, in the context of all models of the DLM type, these events are modeled by a diffusive like process, with the actual events being parameterized by an eddy diffusivity, K_Z. The formulation in DLM-WQ follows the premise that the diffusivity depends on the dissipation of turbulent kinetic energy and inversely depends on the stratification. Thus:

$$K_Z = \alpha \frac{\varepsilon}{N^2 + k_0^2 u^2} \tag{4.20}$$

where k_O is wave number of the turbulent eddies; u denotes turbulent velocity scale; ε denotes dissipation; α is a constant related to the efficiency of the conversion of turbulent kinetic energy to mixing. In the hypolimnion, this diffusivity is applied to the diffusion equation, after calculation of ε, k_O and u from the energy inputs of wind and inflow.

Sediment resuspension model

Sediment resuspension is known to greatly influence water quality in shallow water bodies (Hamilton and Mitchell, 1997). A sediment resuspension model has been included in the current Salton Sea version of DLM-WQ, the most recent modeling of the Salton Sea (Schladow et al., 2004). As very little is known about the sediment characteristics, such as sediment diameter and density, or sediment fluxes at the Salton Sea, a simple modeling approach of Somlyody (1986) was specifically adopted. Here, the sediment resuspension rate, E, is described as follows:

$$E = kw^m \tag{4.21}$$

where w is the wind speed, and k and m are calibration parameters. A threshold velocity was set, below which resuspension was assumed not to be occurring. Once resuspended, particles are allowed to resettle at a prescribed velocity.

In this research, we combined three other sediment resuspension models with DLM-WQ, and then applied them to the Salton Sea (Chung et al., in press; Hamilton and Schladow, 1997; Losada, 2001; Schladow and Hamilton, 1997). The three sediment models represent different sediment characteristics. The models include Mian and Yanful (2004) (i.e. Equation (2.4)) for *cohesive* sediments and the extended García and Parker for non-*cohesive* sediments, which are described in detain in Chapter 3. In addition, a simple linear relationship is achieved by setting m = 1 in Equation (2.4) and frequently used as follows (Gowland et al., 2007; Hawley and Lesht, 1992; Mei et al., 1997; Sanford and Halka, 1993; Sanford and Maa, 2001):

$$E = M\left[\tau_b - \tau_{cr}\right] \qquad \text{for } \tau_b \geq \tau_{cr} \tag{4.22}$$

where M is an empirical coefficient. In this research, we used two forms of the sediment resuspension model for cohesive sediments in order to combine them with DLM–WQ. All models are formulated in terms of the bed shear stress exerted by wind-induced waves and currents. The output of each water quality model is compared with measured data.

ECOLOGICAL PROCESSES

Chemical and biological components in DLM-WQ are modeled to be analogous to the physical components (e.g. temperature and salinity) in the mixing processes which are described in the preceding section. When layers merge, the new concentration in the merged layer is a volumetric average of the component layers. If water is removed from a layer by an outflow, the concentration of the water quality components in the layer remains unchanged and only the layer volume is adjusted. Mixing of chemical and biological components is therefore done in conjunction with modeling of temperature, salinity and density, and uses the same sub-daily timestep based on surface layer dynamics or a set, constant timestep. The effect of biochemical reactions on water quality is modeled over the sub-daily timestep.

Modeling phytoplankton dynamics

Phytoplankton biomass is modeled using chlorophyll *a* concentration, the standard biomass measurement (OECD, 1982). Phytoplankton growth rate limited by environmental factors is modeled by multiplying the maximum potential phytoplankton

growth rate (G_{max}; d^{-1}) by a temperature adjustment factor and a growth limiting fraction with a value between zero and one. This fraction is the minimum value determined from equations for limitation by light, nitrogen and phosphorus concentrations.

Light limitation fraction in layer i, $f(I_i)$, is determined from the Steele (1974) function. The light response function assumes that phytoplankton responds to various light conditions instantaneously and with no light history effect. The nutrient functions in layer i, such as phosphorus fraction, $f(P_i)$, and nitrogen fraction, $f(N_i)$, are based on the Michaelis-Menten kinetics, and assume that the external concentrations of available nutrients determine the growth rate of phytoplankton (Bowie et al., 1985; Losada, 2001).

$$f(I_i) = \frac{I}{I_{sat}} EXP\left(1 - \frac{I}{I_{sat}}\right) \tag{4.23}$$

$$f(P_i) = \frac{SRP}{k_{SRP} + SRP} = \frac{OP}{k_{op} + OP} \tag{4.24}$$

$$f(N_i) = \frac{(NO_3 + NH_4)}{k_{NO_3+NH_4} + (NO_3 + NH_4)} \tag{4.25}$$

where I and I_{sat} denote the ambient light intensity (irradiance level, not PAR) and the saturation light intensity, respectively; SPR_i is the concentrations of the bio-available phosphorus in layer i; k_{SRP} denotes the half saturation constants; NO_{3i} and NH_{4i} denote the concentrations of the nitrate and the ammonia in layer i, respectively; $k_{NO_3+NH_4}$ is the half saturation constants. Beer's equation is used to determine light intensity at depth, z, in the water column as described in Equation (4.3).

Phytoplankton biomass is lost through respiration and mortality after the appropriate growth increment has been applied to the chlorophyll *a* concentration. Phytoplankton is assumed to settle a fixed amount each day, although hydrodynamic mixing processes are capable of resuspending them. The equation of the phytoplankton dynamic process in layer i over the sub-time step is as follows:

$$\frac{\partial Chla_i}{\partial t} = \sum \dot{I} - \sum \dot{O}$$
$$= \left[G_{MAX} \theta_{Chla}^{T-20} Chla_i Min\left\{ f(I_i), f(P_i) f(N_i) \right\} \right]$$
$$- \left[K_{RESP} \theta_{Chla}^{T-20} Chla_i + K_{MORT} \theta_{Chla}^{T-20} Chla_i + \frac{W_{Chla} Chla_i}{H_i} \right] \quad (4.26)$$

where $Chla_i$ is the concentration of chlorophyll *a* in layer i; G_{MAX} is the maximum growth rate of phytoplankton; θ_{Chla}^{T-20} is the non-dimensional temperature multipliers of chlorophyll *a*; K_{RESP} denotes the respiration rate of chlorophyll *a*; K_{MORT} denotes the mortality of chlorophyll *a*; W_{Chla} is the settling velocity of IP; H_i is the depth of layer i.

Modeling nutrient dynamics

The conceptual models of nutrients have been developed specifically for the Salton Sea based on a balance between what are considered to be the best present understanding of nutrient dynamics in the Salton Sea, and the extremely limited data set available for model calibration.

Phosphorus

Figure 4.6 shows the conceptual model of phosphorus that has been developed specifically for the Salton Sea. The phosphorus model consists of ortho-phosphate (OP), particulate phosphorus (PP) and internal phosphorous (IP) in the biomass. IP is assumed to be mainly composed of phytoplankton.

The OP pool is added through inflows, sediment flux release and mechanical release induced by sediment resuspension, such as entrainment of OP in the pore water into the water column. The OP is biologically taken up and chemically sequestered by precipitation and/or adsorption to PP. Rate constants are used to describe the rate at which these processes occur. The addition of OP by the inflows is described by the model input data. A mixing depth is calculated internally by DLM-WQ. Both sediment flux release and mechanical release are assumed to occur over this depth, but not to exceed 6 m, below which OP is assumed to be chemically transformed to PP immediately and so negligible at the first-order kinetics. Enhanced sediment nutrient release under anoxic conditions is not assumed in the model. The equation describing OP dynamics is as follows:

$$\frac{\partial OP_i}{\partial t} = \sum \dot{I} - \sum \dot{O}$$

= (Inflow + Sediment release + Mechanical Release)

– (Uptake + Precipitation (+ Adsorption))

$$= \left[S_p \theta_{SED}^{T-20} \frac{AS_i}{V_i} + OP_S \frac{\phi}{1-\phi} \frac{k_1 W^{m1}}{H} \right]$$
$$- \left[G_{\max} \theta_{Chla}^{T-20} a_P Chla_i \cdot Min\{ f(I_i), f(P_i), f(N_i) \} + k_{PREC} \theta_{RXN}^{T-20} OP_i \right] \quad (4.27)$$

where OP_i is the ortho-phosphate concentration in layer i; a_P is the constant ratio of phosphorus to chlorophyll *a*; θ_{SED}^{T-20} and θ_{RXN}^{T-20} denote the non-dimensional temperature multipliers of sediment release and precipitation (or adsorption) reaction, respectively; S_P is the sediment release rate of OP; AS_i is the area of sediments in contact with layer i; V_i is the volume of water in layer i; OP_S is the ortho-phosphate concentration in the pore water of the sediment; H denotes water depth; ϕ indicates porosity, defined $\phi = 1 - \frac{\rho_b}{\rho_s}$ where ρ_s is sediment density and ρ_b is bulk density; k_1 and m_1 are the constants of sediment resuspension, respectively; W is the wind speed if $W > W_C$; with W_C is the critical speed to resuspension; k_{PREC} is the precipitation (and/or sorption) rate constants.

PP is assumed to be the difference between total phosphorus (TP) and OP. If TP < OP, PP is assumed to be zero. PP pool is increased through algal respiration and mortality and sediment resuspension, and lost by settling. The equation of PP dynamics is as follows:

$$\frac{\partial PP_i}{\partial t} = \sum \dot{I} - \sum \dot{O}$$

= (Inflow + Respiration + Mortality + Sediment Resuspension

+ Precipitation (+ Sorption)

– (Settling)

$$= \left[K_{RESP} \theta_{Chla}^{T-20} a_P Chla_i + k_{MORT} \theta_{Chla}^{T-20} a_P Chla_i + r_{PS} \frac{k_1 W^{m1}}{H_i} + k_{PREC} \theta_{SS}^{T-20} OP_i \right]$$
$$- \left[\frac{W_{PP} PP_i}{H_i} \right] \quad (4.28)$$

where PP_i denotes the particulate phosphorus in layer i; W_{PP} denotes the settling velocity of PP_i; H_i is the depth of layer i; r_{PS} is the ratio of particulate phosphorous of the suspended solids.

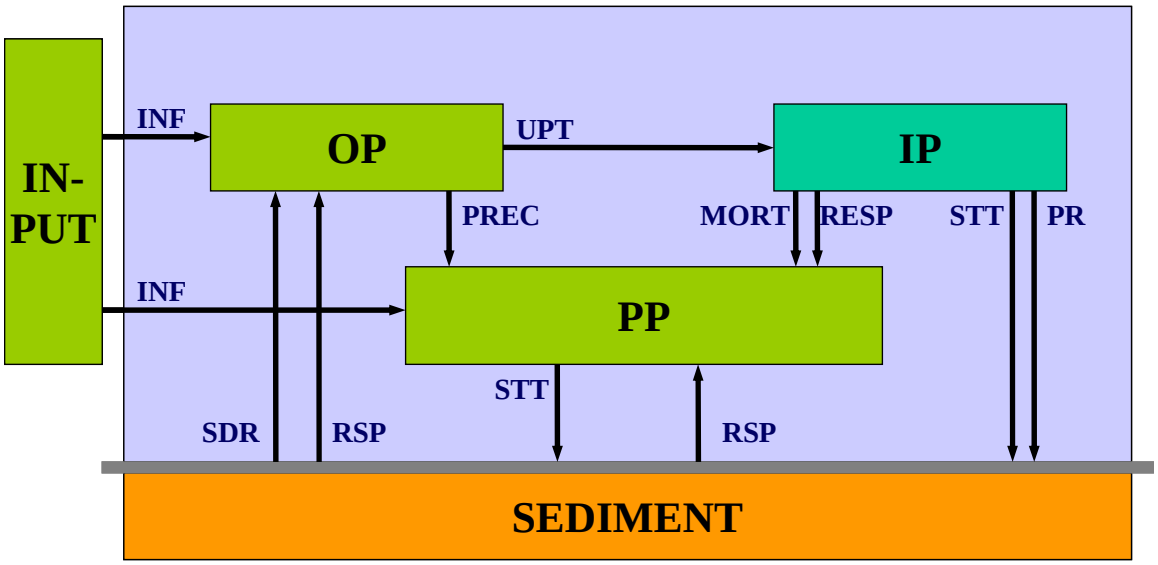

Figure 4.5 Conceptual model of phosphorous of the Salton Sea: INF=Inflow, RESP=Respiration, UPT=Uptake, MORT= Mortality, PR=Permanent Removal, PREC=Precipitation, STT=Settling, RSP=Resuspension, SDR=Sediment Release.

IP is assumed to be all the phosphorus in the biomass in the water column. The IP pool is only increased with the uptake of OP, and consumed by respiration and by mortality and by settling (via phytoplankton settling) and permanently lost to the sediments. Grazing is not considered in the IP loop. The equation for IP is as follows:

$$\begin{aligned}\frac{\partial IP_i}{\partial t} &= \sum \dot{I} - \sum \dot{O} \\ &= (\text{ Uptake of OP }) \\ &- (\text{ Respiration + Mortality + Settling + Permanent removal }) \\ &= \left[G_{MAX}\theta_{Chla}^{T-20} a_P Chla_i \cdot Min\{f(I_i), f(P_i), f(N_i)\}\right] \\ &- \left[K_{RESP}\theta_{Chla}^{T-20} a_P Chla_i + K_{MORT}\theta_{Chla}^{T-20} a_P Chla_i + \frac{W_{Chla} a_P Chla_i}{H_i} + K_{PR}\theta_{Chla}^{T-20} a_P Chla_i\right]\end{aligned} \quad (4.29)$$

where IP_i denotes the internal phosphorus concentration in layer i; W_{Chla} is the settling velocity of chlorophyll *a*; K_{RESP} denotes the respiration rate of chlorophyll *a*; K_{MORT} denotes the mortality of chlorophyll *a*; K_{PR} denotes the coefficient of permanent removal of phosphorus.

Nitrogen

The nitrogen conceptual model developed specifically for the Salton Sea consists of nitrate (NO3), ammonium (NH4), particulate nitrogen (PN) and internal nitrogen (IN) in the biomass as shown in Figure 4.7.

Nitrate (NO3) is provided with inflow and nitrification of ammonium (NH4), but consumed by the uptake of IN and by denitrification. Reactions to describe the rate at which these processes occur are assumed to be the first-order kinetics. The nitrification reaction depends on ammonium concentration and sufficient oxygen levels (greater than 1 to 2 mg L^{-1}). The nitrification inhibition factor, f_{NIT}, is expressed as a function of the concentration of dissolved oxygen (DO) as follows (Chapra, 1997):

$$f_{NIT} = 1 - \exp(-k_{nitr} \times DO) \tag{4.30}$$

where DO_i denotes the dissolved oxygen concentration in layer I; k_{nitr} denotes first-order nitrification inhibition coefficient (≈0.6 L mg^{-1}).

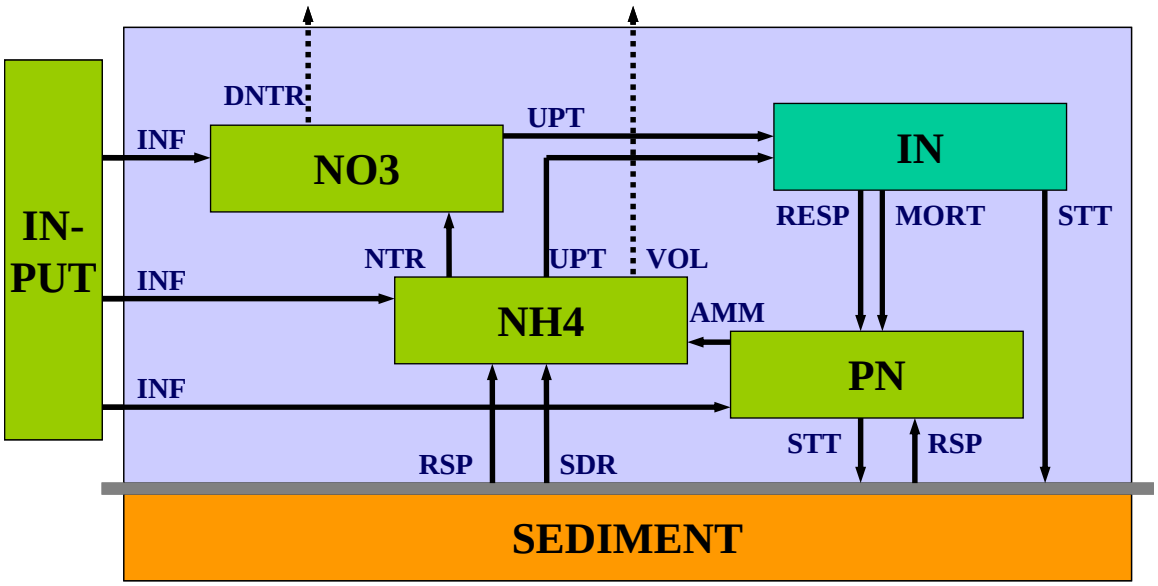

Figure 4.6 Conceptual model of nitrogen of the Salton Sea: INF=Inflow, RESP=Respiration, UPT=Uptake, MORT= Mortality, NTR=Nitrification, DNTR=Denitrification, VOL=Volatilization, AMM=Ammonification, STT=Settling, RSP=Resuspension, SDR=Sediment Release.

The ammonia preference factor, $\beta_{NH3} = \frac{NH_3}{NH_3 + NO_3}$, is used in this conceptual model and assumes that there is no preference for either form of nitrogen, but only the relative proportions of the concentrations of ammonia and nitrate in the water column (Bowie et al., 1985). The equation of NO3 dynamics is as follows:

$$\frac{\partial NO3_i}{\partial t} = \sum \dot{I} - \sum \dot{O}$$

$$= (\text{ Inflow} + \text{Nitrification })$$

$$
\begin{aligned}
&-(\text{ Uptake + Denitrification }) \\
&= \left[k_{NIT} \theta_{RXN}^{T-20} NH4_i \, f_{NIT} \right] \\
&- \left[(1-\beta_{NH3}) G_{\max} \theta_{Chla}^{T-20} a_N Chla_i \cdot Min\left\{ f(I_i), f(P_i), f(N_i) \right\} + k_{DNT} \theta_{RXN}^{T-20} NO3_i \right]
\end{aligned} \tag{4.31}
$$

where $NO3_i$ and $NH4_i$ denote nitrate concentration in layer i and ammonium concentration in layer i, respectively; k_{NIT} is the nitrification rate of $NH4_i$; a_N is the constant ratio of nitrogen to chlorophyll *a*; k_{DNT} is the denitrification rate of $NO3_i$; θ_{RXN}^{T-20} is the non-dimensional temperature multipliers of reaction.

Ammonium (NH4) sources include inflows, sediment flux releases and mechanical releases and with ammonification of PN, but it is consumed by nitrification, volatilization of ammonia and the uptake by IN. Ammonification process, which is the mineralization of N from decomposing materials, begins with the release of NH4+ by heterotrophic microbes (Schlesinger, 1991).

Volatilization is considered only for the surface layer, and can occur only as a form of ammonia (NH_3). Since the concentrations of NH_3 and NH_4^+ vary considerably over the range of pH and temperature found in natural waters, we need to know pH of the Salton Sea for the ammonia association. Each can be calculated assuming that equilibrium conditions exist (Bowie et al., 1985). The range of the temperature in the Salton Sea is roughly from 14 °C to 30 °C and the range of pH is shown in Table 4.1. As the percent un-ionized ammonia is about 3% to 6% based on these measurements, the percent of un-ionized ammonia is assumed to be 4.5% in the model.

Table 4.1 The range of pH in the Salton Sea (Holdren and Montaño, 2002)

	Average	Min.	Max.
Alamo River	7.692	7.47	7.91
New River	7.518	7.11	7.7
Whitewater River	7.656316	7.36	7.88
Station 1 in the Sea	8.068367	6.81	8.69
Station 2 in the Se	8.134661	7.39	8.66
Station 3 in the Se	8.080069	7	8.56

Mass transfer coefficient of ammonia, $K_{l,NH3}$, in the volatilization is expressed by temperature and wind velocity as follows (Jellison et al., 1993):

$$
K_{L,NH3} = 0.5107 + 0.2554 \cdot U(8) + 0.03944 \cdot U(8)^2 \tag{4.32}
$$

where T denotes absolute temperature (K), and V denotes wind velocity [m s^{-1}]. If an average value for atmospheric concentration is assumed to be 2 ppb ($2e^{-9}$ atm), according to Henry's Law, the saturation concentration of NH_3 in water, c, is as follows (Ni, 1999):

$$
c = \frac{p}{H_e} = \frac{2e-9}{1.1561 \exp(-4151/T_a)} = \frac{atm}{atm \diagup mg/L} \tag{4.33}
$$

where H denotes Henry's constant; P denotes atmospheric concentration of ammonia. The equation of NH4 dynamics is as follows:

$$\frac{\partial NH4_i}{\partial t} = \sum \dot{I} - \sum \dot{O}$$

= (Inflow + Sediment release + Mechanical Release + Ammonification)

– (Uptake + Nitrification + Volatilization)

$$= \left[S_N \theta_{SD}^{T-20} \frac{AS_i}{V_i} + NH4_S \frac{\phi}{1-\phi} \frac{k_1 W^{m1}}{H} + k_{AMM} \theta_{RXN}^{T-20} PN_i \right]$$

$$- \left[\beta_{NH3} G_{\max} \theta_{Chla}^{T-20} a_N Chla_i \cdot Min\{ f(I_i), f(P_i), f(N_i) \} + k_{NIT} \theta_{RXN}^{T-20} NH4_i \, f_{NIT} \right]$$

$$- \left[K_{L,NH3} \frac{A_{ns}}{V_{ns}} (NH3_{ns} - NH3_{WS}) \right] \qquad (4.34)$$

where S_N denotes the sediment release rate of NH4; $NH4_S$ denotes the ammonium concentration in the pore water of the sediment; k_{AMM} is the ammonification rate of SS_i into NH4; PN_i denotes the particulate phosphorous concentration in layer i; $K_{l,NH4}$ is the mass-transfer velocity of NH3 in the liquid laminar layer; A_{ns} is the surface area; V_{ns} is the volume of water in first layer; $NH3_{WS}$ denotes saturation ammonia concentration; $NH3_{ns}$ denotes the dissolved ammonia concentration in first layer.

IN is all the nitrogen in the biomass in the water column. IN is assumed to be mainly composed of phytoplankton. Grazing of phytoplankton is not considered in the IN loop. IN is provided with the uptake of NO3 and NH4, but consumed by respiration and mortality and by settling (via phytoplankton settling). The equation of IN dynamics is as follows:

$$\frac{\partial IN_i}{\partial t} = \sum \dot{I} - \sum \dot{O}$$

= (Uptake of NO3 and NH4)

– (Respiration + Mortality + Settling)

$$= \left[G_{\max} \theta_{Chla}^{T-20} a_N Chla_i \cdot Min\{ f(I_i), f(P_i), f(N_i) \} \right]$$

$$- \left[k_{RESP} \theta_{Chla}^{T-20} a_N Chla_i + k_{MORT} \theta_{Chla}^{T-20} a_N Chla_i + \frac{W_{Chla} a_N Chla_i}{H_i} \right] \qquad (4.35)$$

where IN_i denotes the internal nitrogen concentration in layer i.

The source of PN is respiration and mortality, and from sediment resuspension, but consumed by ammonification and settling. The equation of PN is as follows:

$$\frac{\partial PN_i}{\partial t} = \sum \dot{I} - \sum \dot{O}$$

= (Inflow + Respiration + Mortality + Resuspension)

– (Ammonification + Settling)

$$= \left[k_{RESP} \theta_{Chla}^{T-20} a_N Chla_i + k_{MORT} \theta_{Chla}^{T-20} a_N Chla_i + r_{NS} \frac{k_1 W^{m1}}{H_i} \right]$$

$$- \left[k_{AMM} \theta_{RXN}^{T-20} PN_i + \frac{W_{PN} PN_i}{H_i} \right] \qquad (4.36)$$

Dissolved Oxygen (DO)

DO conceptual model is developed specifically for the Salton Sea with several processes, such as oxygen reaeration across the air-water interface, biochemical oxygen demand (BOD) for organic decomposition, nitrogenous biochemical oxygen demand (NBOD) for nitrification and sediment oxygen demand (SOD) for benthic sediment and organisms as shown in Figure 4.8. Sources of DO include inflow, reaeration and photosynthesis, while sinks are respiration, BOD, NBOD and SOD. Reactions to describe the rate at which these processes occur are assumed to be the first-order.

Oxygen reaeration occurs only for the surface layer, where gas transfer is liquid-film controlled (Chapra, 1997). The saturation of dissolved oxygen in the surface layer is affected by temperature and salinity. The following equation can be used to establish the dependence of oxygen saturation on temperature and salinity, respectively (Chapra, 1997):

$$\ln O_{SF} = -139.34411 + \frac{1.575701e5}{T_a} - \frac{6.642308e7}{T_a^2} + \frac{1.243800e10}{T_a^3} - \frac{8.621949e11}{T_a^4}$$

$$\ln O_{SS} = \ln O_{SF} - S\left(1.7674e-2 - \frac{1.0754e1}{T_a} + \frac{2.1407e3}{T_a^2} \right) \qquad (4.37)$$

where O_{SF} denotes saturation concentration of dissolved oxygen in fresh water at 1atm (mg L^{-1}); T_a is absolute temperature (K); O_{SS} denotes saturation concentration of dissolved oxygen in saltwater at 1atm (mg L^{-1}); S is salinity (g L^{-1} = ppt, ‰). The oxygen-transfer coefficient, $K_{l,O}$, of the oxygen reaeration for lakes can be estimated as a function of wind speed by Broecker et al. (1978) (Chapra, 1997).

$$K_{l,O} = 0.864 U_w \qquad (4.38)$$

where U_w denotes wind speed measured 10m above the water surface (m s^{-1}).

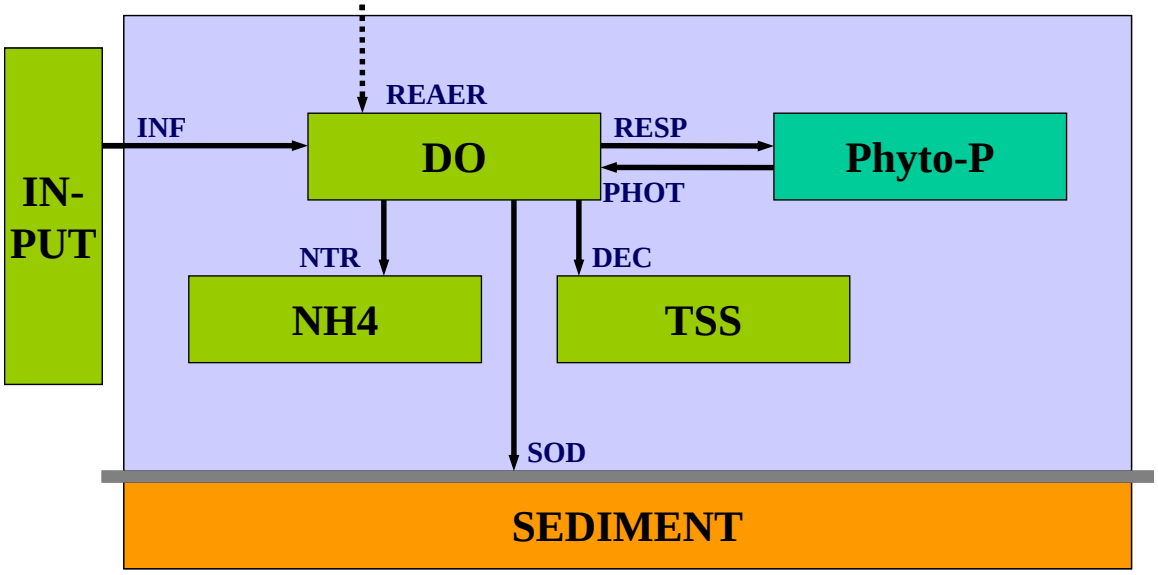

Figure 4.7 Conceptual model of dissolved oxygen of the Salton Sea: INF=Inflow, REAER=Reaeration, RESP=Respiration, SOD=Sediment Oxygen Demand, NTR=Nitrification, PHOT=Photosynthesis, DEC=Decomposition.

SOD is due to the oxidation of organic matter in the bottom sediment and occurs only in the bottom layer. SOD is affected by the organic content of the sediments and the oxygen concentration of the overlying waters. In DLM-WQ, SOD is assumed to be the constant areal SOD rate at 20 °C and affected by temperature (Chapra, 1997). The DO equation is as follows:

$$\frac{\partial DO_i}{\partial t} = \sum \dot{I} - \sum \dot{O}$$

$$= (\text{ Inflow + Reaeration + Photosynthesis })$$

$$- (\text{ Respiration + Nitrification + SOD + Decomposition })$$

$$= \left[K_{l,O} \frac{A_{ns}}{V_{ns}} (O_S - DO_{ns}) + G_{\max} \theta_{Chla}^{T-20} r_{OC} a_C Chla_i \cdot Min\{ f(I_i), f(P_i), f(N_i) \} \right]$$

$$- \left[k_{RESP} \theta_{Chla}^{T-20} r_{OC} a_C Chla_i + k_{NIT} \theta_{RXN}^{T-20} r_{ON} NH4_i \, f_{NIT} + S'_{B,20} \theta_{SD}^{T-20} \frac{AS_i}{V_i} + k_{DEC} \theta_{DO}^{T-20} r_{OC} r_{CSS} SS_i \right] \quad (4.39)$$

where DO_i denotes the dissolved oxygen concentration in layer i; O_S denotes saturation oxygen concentration; DO_{ns} denotes the dissolved oxygen concentration in first layer; r_{OC} is the ratio of mass of oxygen consumed per mass of carbon assimilated (= 2.67 mgO mg^{-1}C); a_C is the ratio of carbon of chlorophyll *a*; r_{ON} is the amount of oxygen consumed per unit mass of nitrogen oxidized in the total process of nitrification (= 4.57 gO g^{-1}N); $S'_{B,20}$ denotes areal SOD rate at 20 °C; θ_{SD}^{T-20} and θ_{DO}^{T-20} denote the non-dimensional temperature multipliers of reaction; r_{CS} is the ratio of carbon of suspended solids; and k_{DEC} is the decomposition rate.

Suspended solids

Figure 4.9 shows the conceptual model of SS developed specifically for the Salton Sea. SS is provided with sediment resuspension, with precipitation of OP and ammonification of NH4, and respiration and mortality of phytoplankton, but lost by settling. The ratios of P and N to SS are estimated by Holdren and Montano (2002) as follows:

SS_P ≅ P/TSS ≅ (TP-OP)/TSS = 0.0025
SS_N ≅ T/TSS ≅ (TKN-NH4)/TSS = 0.11

where TKN is Total Kjeldahl Nitrogen, a measure of ammonia and organic nitrogen.

The equation of SS is as follows:

$$\begin{aligned}\frac{\partial SS_i}{\partial t} &= \sum \dot{I} - \sum \dot{O} \\ &= (\text{ Inflow + Resuspension + Precipitation of OP + Mortality }) \\ &\quad -(\text{ Settling + Ammonification }) \\ &= \left[\frac{k_1 W^{m1}}{H_i} + \frac{k_{PREC}\theta_{SS}^{T-20} OP}{r_{PSS}}_i + k_{MORT}\theta_{Chla}^{T-20} a_C Chla_i\right] \\ &\quad -\left[\frac{W_{SS} SS_i}{H_i} + \frac{k_{AMM}\theta_{RXN}^{T-20} PN_i}{r_{NSS}}\right]\end{aligned} \tag{4.40}$$

where SS_i denotes the suspended solid concentration in layer i.

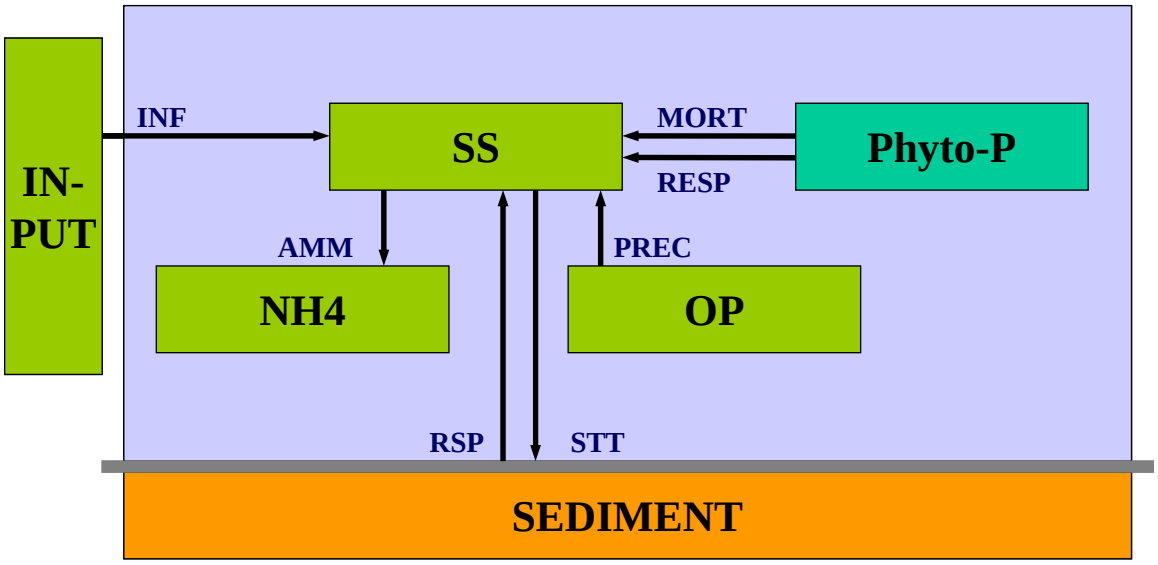

Figure 4.8 Conceptual model of suspended solids of the Salton Sea: INF=Inflow, MORT=Mortality, RESP=Respiration, AMM=Ammonification, PREC=Precipitation, STT=Settling, RSP=Resuspension.

MODEL EVALUATION METHODS

There has been much debate on the subject of evaluation and/or validation of numerical models of natural systems, with disagreement on whether model validation is essential or impossible (Arhonditsis and Brett, 2005; Mayer and Butler, 1993; Oreskes et al., 1994; Rykiel, 1996). Here we use statistical evaluation/validation techniques to compare each calibrated sediment model with the measured data. We use both statistical and graphical model evaluation methods (Abraham and Ledolter, 1983; Jørgensen et al., 1986; Loague and Green, 1991; Power, 1993; Reckhow, 1980; Reckhow et al., 1990).

Many goodness of fit statistics, such as analysis of residual errors (i.e. the difference between observed/measured and predicted values), are available for evaluating deterministic model performance (Abraham and Ledolter, 1983; Jørgensen et al., 1986; Loague and Green, 1991; Reckhow and Chapra, 1983; Reckhow et al., 1990; Stow et al., 2003). For model comparison, we used four kinds of statistical methods, including root mean squared error (*RMSE*) and a general standard deviation (*STD*) for measures of errors, sample autocorrelation of errors for checking assumption of uncorrelated errors, *t*–test for model adequacy, and box plots for graphically comparing orders of statistics. We calculated these statistics for each sediment model as follows:

Root mean squared error (*RMSE*);

$$RMSE = \sqrt{\frac{\sum_{i=1}^{n} (P_i - O_i)^2}{n}} \frac{1}{\overline{O}}$$

General standard deviation (*STD*);

$$STD = \frac{\sqrt{\sum_{i=1}^{n} (P_i - O_i)^2}}{n\,\overline{O}}$$

Sample autocorrelation of residual errors;

$$r_k = \frac{\sum_{i=k+1}^{n} (P_i - O_i)(P_{i-k} - O_{i-k})}{\sum_{i=1}^{n} (P_i - O_i)^2} \qquad k = 1,2,\ldots$$

t–test

$$t = \frac{\sqrt{n}}{s} \frac{\sum_{i=1}^{n} (P_i - O_i)}{n}$$

where P_i is the predicted values; O_i is the observed/measured values; n is the number of compared pairs; $\overline{O}$ and $\overline{P}$ are the mean of observation/measurement and prediction, respectively; k is the chosen number of lags for which the sample autocorrelation of the residual errors; and s is sample standard deviation from observed/measured values, $s^2 = \frac{\sum_{i=1}^{n} (P_i - O_i)^2}{n - p - 1}$. The significance of the calculated sample autocorrelations is determined by comparing each of the r_k values with twice its standard error. We questioned the assumption of uncorrelated errors whenever $|r_k| > 2/\sqrt{n}$ (Abraham and Ledolter, 1983).

A graphical method using box plots provides information on the median, spread or variability, skew, size of data set, and statistical significance of the median. Specifically, the notches around the median in the box estimate the uncertainty about the

box-to-box comparison. If the notches about two medians do not overlap, the medians significantly differ at approximately a 95% confidence level (McGill et al., 1978; Reckhow, 1980; Reckhow and Chapra, 1983).

MODEL APPLICATION, COMPARISON AND SIMULATION RESULTS

Only 2 partial years of data were available for the Salton Sea. For instance, during 1997, Cook (2000) collected water temperature data for several periods using thermistors at four elevations within the Sea. In 1999, the U.S. Department of Interior's Bureau of Reclamation (USBR) collected water quality profiles at 2 – 4 week intervals at three locations in the Sea (Holdren and Montaño, 2002). During that same year, San Diego State University (SDSU) also collected chlorophyll *a* data (Hurlbert et al., San Diego State University, unpubl. raw data). Thereby, lack of data precludes the possibility of performing a complete calibration and separate validation with an independent set of data. However, we calibrated the water temperature model of DLM-WQ using Cook's data and then validated it using Holdren and Montaño's data. Based on the validated model for water temperature, we performed a calibration of the water quality characteristics of DLM-WQ.

Data inputs

DLM–WQ requires four kinds of input data: descriptive data for the lake (bathymetric data), hydrodynamic forcing data (meteorological data and inflow and outflow data), water quality data of stream inflows and initial conditions for all the modeled variables. Bathymetric data of the Salton Sea are surface areas and cumulative volumes as a function of elevation, which were calculated based on a Hydrographic GPS survey of the Sea conducted by the U.S. Bureau of Reclamation (USBR) in 1995 (Cook et al., 2002). The slope and cross section of the stream inflows were estimated from topographical maps.

The daily meteorological data are solar short wave radiation, long wave radiation, air temperature, relative humidity, wind speed and precipitation. CIMIS provided the meteorological data at several stations located around the Salton Sea (Figure 3.1(a)).

Flow rates of the three main inflows were measured by the U.S. Geological Survey (USGS). We used the water quality data of Holdren and Montaño (2002) and Hurlbert et al. (San Diego State University, unpubl. raw data) for calibrations of water quality state variables of DLM–WQ with sediment models.

Thermal and hydrodynamic calibration and validation

Because thermal stratification and the meteorology largely control the physical mixing and many of the biogeochemical processes in the Sea, 1997 data were used to perform a calibration of the temperature model, and 1999 data were used to validate the temperature model. DLM-WQ without the ecological model was run for the water temperature with the light extinction coefficient, η, as 2.1 m^{-1}, which was estimated from the average Secchi disk reading of the Salton Sea in 1999 of 0.85 m as described in Equation (4.6). Meteorological data from CIMIS Station 127, including solar radiation, daily average air temperature, relative humidity, wind speed, and precipitation, were used, and daily wind data were modified by multiplying a factor of 1.1 for both year calibrations.

The simulated and measured (Cook, 2000) water temperatures for 1997 are shown in Figure 4.10. The data set extends from May 20 (day 140) to July 27 (day 208), and includes the time when the Sea was stratified. The data set was collected from thermistors at elevations 1m, 7.3m, 10.9m and 12.3m from the bottom. The surface and bottom thermistors were not operational during this period.

The overall trends between simulated and measured data agree well (Figure 4.10). The maximum difference between daily averaged temperatures was 1.9 °C. Both data sets show a deep thermocline initially, which breaks down around day 162. The weaker stratification that persists after day 165, as well as the near-isotherm conditions at the end of the period is resolved reasonable well by the model. The coarse spacing of instruments (up to 6 m) with no surface thermistor and the interpolation required to produce contours yield the appearance of more gradual changes than the simulated results, which has a vertical resolution of 0.1 – 0.2 m.

Direct comparisons between the actual thermistor traces and the temperatures at the corresponding elevations in the model are shown in Figure 4.11. Simulated and measured data are in relatively good agreement. The differences of mean temperatures between simulated and measured at 1m, 7.3m, 10.9m and 12.3m from the bottom are only 1.40 °C, 0.38 °C, 0.04 °C, and 0.06 °C, respectively.

The water temperature component of DLM-WQ was validated using the 1999 data. Measured temperature data (sampled at 2– to 4–week intervals) are compared with the DLM-WQ simulations run for the period from January 22, 1999 (day 22) to December 15, 1999 (day 349) in Figure 4.12. These dates mark the first and last days of the USBR data sampling for 1999. These data are in good agreement, particularly considering the crude measurement intervals. Both data sets show unstratified initial and final conditions and stratification between days 160 and 210.

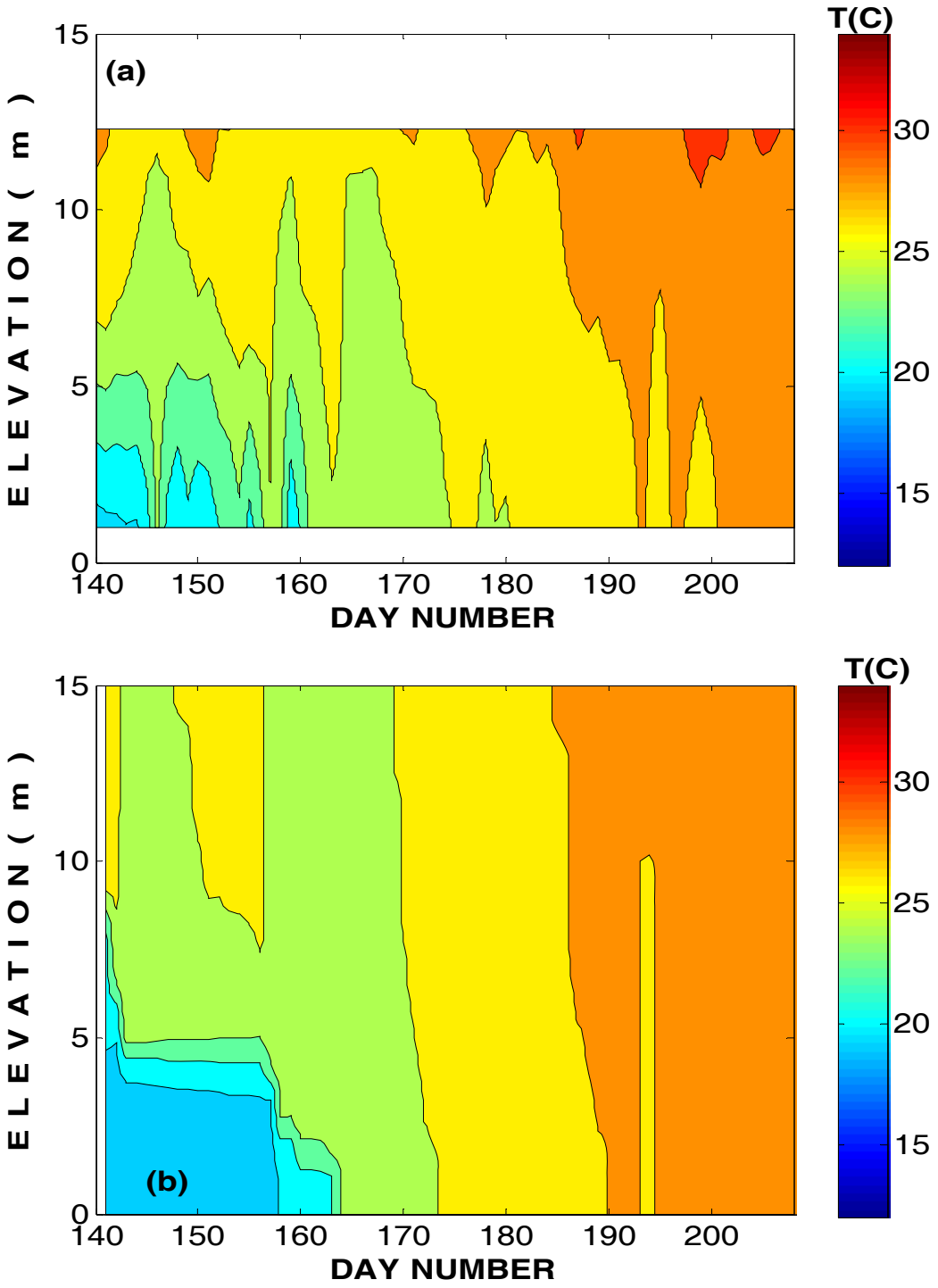

Figure 4.9 Depth-time contours of temperature of the Salton Sea from May 20, 1997 to July 27, 1997: (a) Measured temperature data from a station near the center of the Salton Sea. No data were available at the surface and bottom since temperature loggers were placed near the top (10%), upper-quarter (25%), mid (50%), bottom (90%) points of the water column (Cook, 2000); (b) Modeled temperature distribution using DLM-WQ.

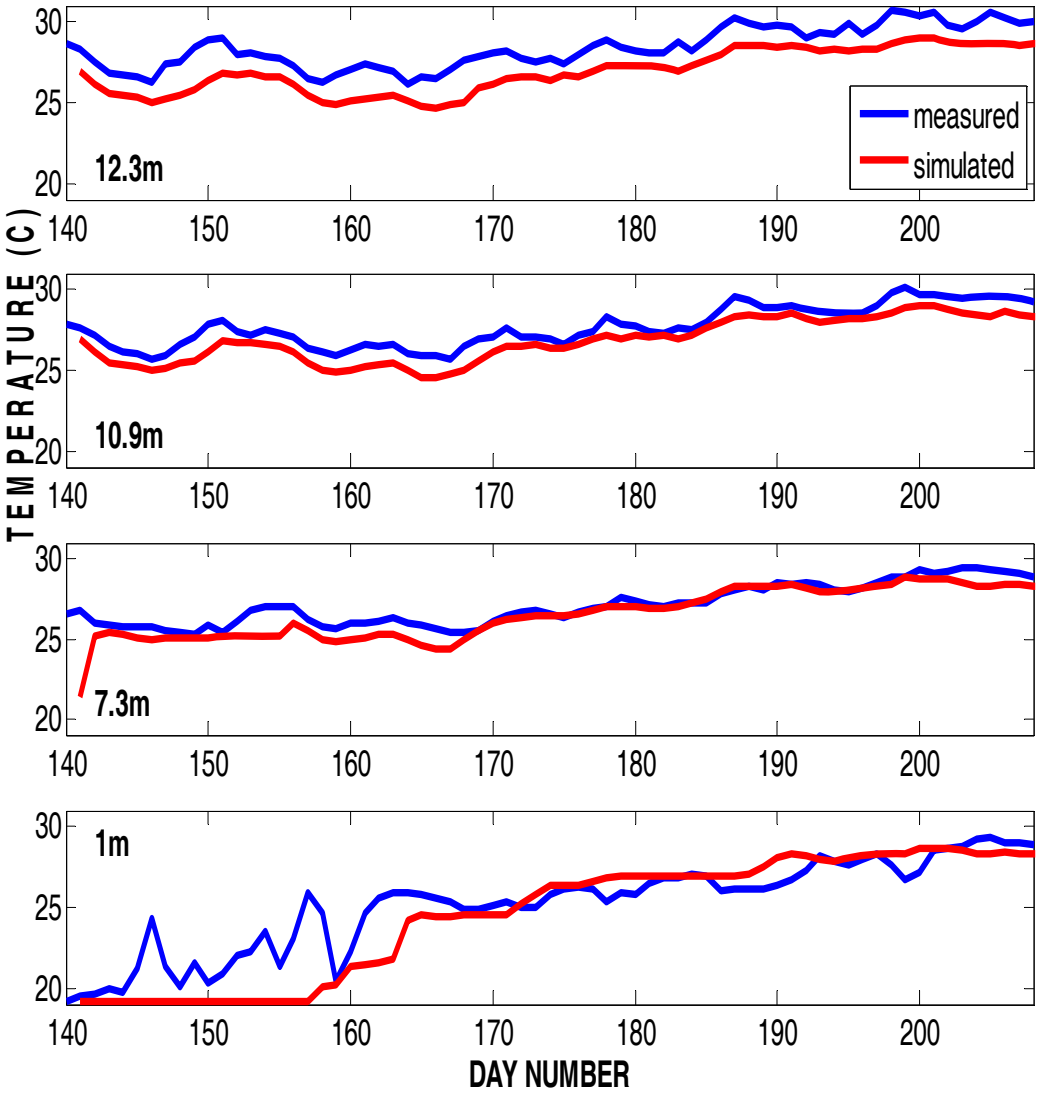

Figure 4.11 Temperature traces of the Salton Sea at four elevations. Blue line shows measurement near the center of the Salton Sea with a depth of 15 m, and red line shows DLM-WQ simulation from May 20, 1997 to July 27, 1997.

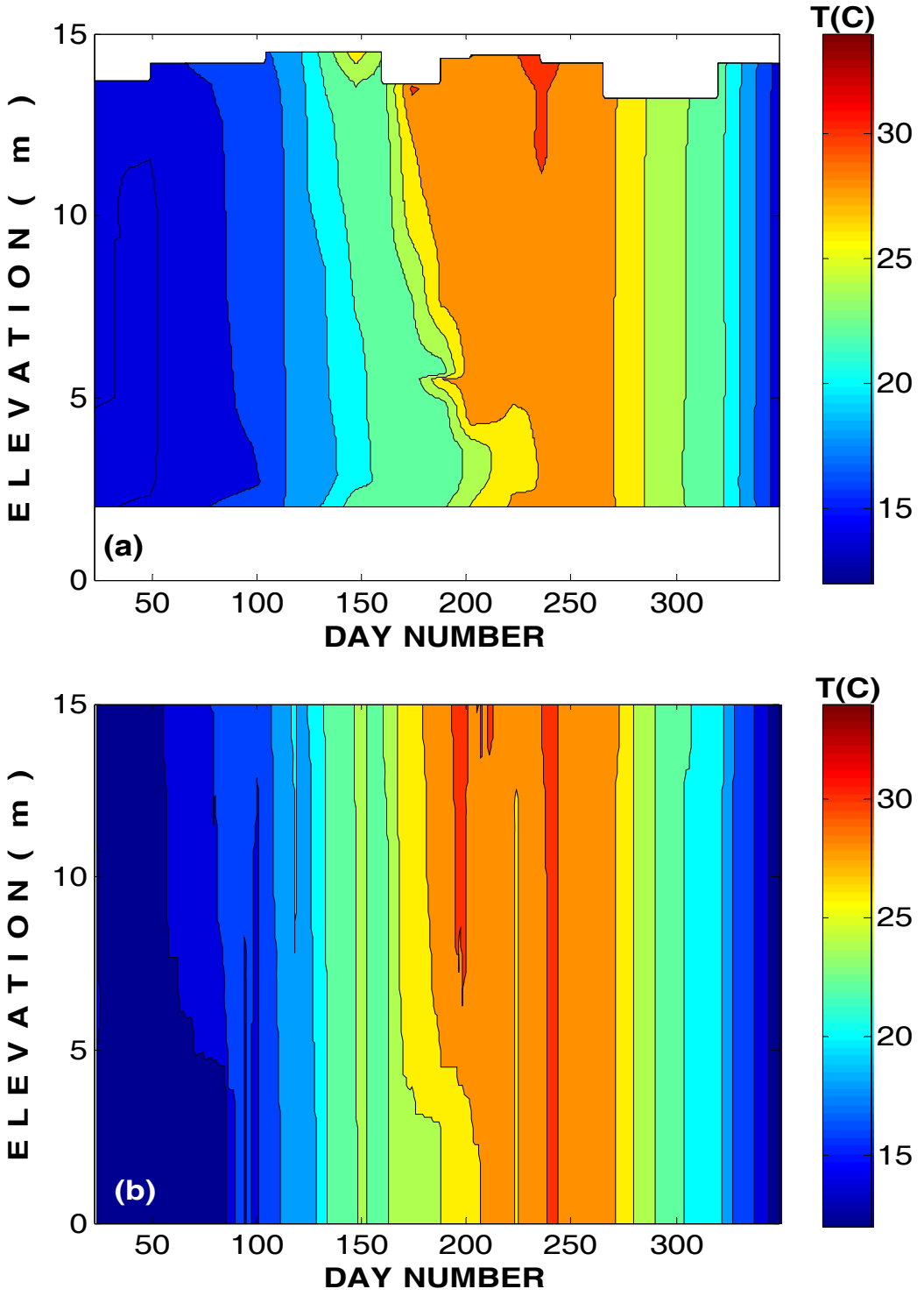

Figure 4.12 Depth-time contours of temperature of the Salton Sea in 1999 for DLM-WQ validation: (a) measured temperature data in 1999. No data were available at the surface and bottom; (b) model simulation of temperature in 1999.

Comparison between sediment resuspension models

The remainder of the water quality parameters was calibrated using 1999 data by adjusting rate coefficients and parameters; a true validation will have to await the availability of a future, suitable data set. The existing DLM-WQ model incorporated the sediment resuspension model of Somlyody (1986). Three other sediment resuspension models, including Mian and Yanful (2004), the linear relation, and the extended García and Parker were also added to DLM-WQ and then calibrated. The calibrated DLM-WQ with sediment models were compared to one another by using statistical evaluation methods to determine the best model describing the measured data of the Salton Sea.

The calibrated model output includes chlorophyll *a*, DO, OP, PP, NO3, NH4, PN, and SS. The coefficients, constants and forcing parameters of DLM-WQ with each sediment model are shown in Table 4.2 – 4.5.

Table 4.2 The coefficients, constants and forcing parameters of DLM–WQ with the sediment resuspension model of Somlyody (Bowie et al., 1985; Losada, 2001).

Symbols	Description	Calibrated Value	Units
Phytoplankton			
G_{MAX}	Maximum growth rate of phytoplankton	6.0	day^{-1}
k_{RESP}	Respiration rate of phytoplankton	0.15	day^{-1}
k_{MORT}	Mortality of phytoplankton	0.03	day^{-1}
θ_{Chla}^{T-20}	Non-dimensional temperature multipliers of phytoplankton	1.068	-
a_P	Constant ratio of phosphorous to chlorophyll *a*	0. 75	-
a_N	Constant ratio of nitrogen to chlorophyll *a*	13.0	-
a_C	Constant ratio of carbon to chlorophyll *a*	61.0	-
$k_{NO3+NH4}$	Half saturation constant of nitrogen	55.0	$\mu g\ L^{-1}$
k_{OP}	Half saturation constant of phosphorous	3.0	$\mu g\ L^{-1}$
I_{SAT}	Saturation light intensity	60.0	Watt m^{-2}
Light attenuation coefficients			
etca	Light attenuation coefficient for chlorophyll *a*	0.017	m^{-1}
etpart	Light attenuation coefficient for particules	0.025	m^{-1}
Settling velocity			
W_{Chla}	Settling velocity of chlorophyll *a*	1.0	m day^{-1}
W_{PN}	Settling velocity of PN	1.0	m day^{-1}
W_{PP}	Settling velocity of PP	3.0	m day^{-1}
W_{SS}	Settling velocity of SS	4.0	m day^{-1}
Chemical constants			
$S_{B,20}$	Areal SOD rate at 20°C	0.2	mg L^{-1}
θ_{SD}^{T-20}	Non-dimensional temperature multipliers of SOD	1.065	-
k_{DEC}	Decomposition rate constant	1.5e-2	day^{-1}
r_{OC}	Ratio of mass of oxygen consumed per mass of carbon assimilated	2.67	$mgO\ mgC^{-1}$

r_{ON}	Amount of oxygen consumed per unit mass of nitrogen oxidized in the total process of nitrification	4.57	gO gN^{-1}
k_{nitr}	Nitrification inhibition coefficient	0.6	L mg^{-1}
θ_{DO}^{T-20}	Non-dimensional temperature multipliers of reactions	1.08	-
k_{AMM}	Ammonification rate constant	3.5e-2	day^{-1}
k_{NIT}	Nitrification rate constant of NH4	7.5e-2	day^{-1}
k_{DNT}	Denitrification rate constant of NO3	9.5e-3	day^{-1}
θ_{RXN}^{T-20}	Non-dimensional temperature multipliers of reactions	1.08	-
k_{PREC}	Rate constant of OP -> PP	1.0e-1	day^{-1}
k_{PR}	Coefficient of permanent removal of P	1.09e-5	day^{-1}
Sediments			
OP_S	OP concentration in the pore water of sediment	9.1e5	mg L^{-1}
$NH4_S$	NH4 concentration in the pore water of sediment	3.2e7	mg L^{-1}
r_{PSS}	Constant ratio particulate P of SS	2.5e-3	-
r_{NSS}	Constant ratio particulate N of SS	1.1e-1	-
r_{CSS}	Constant ratio particulate C of SS	4.17e-1	-
r_{PS}	Constant ratio P of Sediment	9.6e-4	-
r_{NS}	Constant ratio N of Sediment	2.1e-2	-
ρ_s	Sediment density	2.65e3	kg m^{-3}
S_P	Sediment release rate of OP	4.8	μg m^{-2} d^{-1}
S_N	Sediment release rate of NH4	17.5	μg m^{-2} d^{-1}
θ_{SED}^{T-20}	Non-dimensional temperature multipliers of sediment	1.08	-
Dpref	Mixing depth threshold	6	m
ρ_b	Bulk density	1.2e3	kg m^{-3}
Sediment model			
F	Fetch	30	km
k_1	Sediment resuspension constant	4.5e-4	-
m_1	Sediment resuspension exponent	1.2	-
Wc	Critical wind speed	2.0	m s^{-1}

Table 4.3 The coefficients, constants and forcing parameters of DLM–WQ with the sediment resuspension model of Mian and Yanful (2004) (Bowie et al., 1985; Losada, 2001).

Symbols	Description	Calibrated Value	Units
Phytoplankton			
G_{MAX}	Maximum growth rate of phytoplankton	6.1	day^{-1}
k_{RESP}	Respiration rate of phytoplankton	0.12	day^{-1}
k_{MORT}	Mortality of phytoplankton	0.02	day^{-1}
θ_{Chla}^{T-20}	Non-dimensional temperature multipliers of phytoplankton	1.068	-
a_P	Constant ratio of phosphorous to chlorophyll *a*	0. 75	-
a_N	Constant ratio of nitrogen to chlorophyll *a*	13.0	-
a_C	Constant ratio of carbon to chlorophyll *a*	61.0	-
$k_{NO3+NH4}$	Half saturation constant of nitrogen	55.0	μg L^{-1}
k_{OP}	Half saturation constant of phosphorous	3.0	μg L^{-1}
I_{SAT}	Saturation light intensity	60.0	Watt m^{-2}
Light attenuation coefficients			

etca	Light attenuation coefficient for chlorophyll *a*	0.017	m^{-1}
etpart	Light attenuation coefficient for particules	0.025	m^{-1}
Settling velocity			
W_{Chla}	Settling velocity of chlorophyll *a*	1.0	m day^{-1}
W_{PN}	Settling velocity of PN	1.0	m day^{-1}
W_{PP}	Settling velocity of PP	2.5	m day^{-1}
W_{SS}	Settling velocity of SS	3.0	m day^{-1}
Chemical constants			
$S_{B,20}$	Areal SOD rate at 20°C	0.2	mg L^{-1}
θ_{SD}^{T-20}	Non-dimensional temperature multipliers of SOD	1.065	-
k_{DEC}	Decomposition rate constant	3.0e-2	day^{-1}
r_{OC}	Ratio of mass of oxygen consumed per mass of carbon assimilated	2.67	mgO $_1$mgC^{-}
r_{ON}	Amount of oxygen consumed per unit mass of nitrogen oxidized in the total process of nitrification	4.57	gO gN^{-1}
k_{nitr}	Nitrification inhibition coefficient	0.6	L mg^{-1}
θ_{DO}^{T-20}	Non-dimensional temperature multipliers of reactions	1.08	-
k_{AMM}	Ammonification rate constant	5.5e-2	day^{-1}
k_{NIT}	Nitrification rate constant of NH4	2.5e-2	day^{-1}
k_{DNT}	Denitrification rate constant of NO3	8.5e-3	day^{-1}
θ_{RXN}^{T-20}	Non-dimensional temperature multipliers of reactions	1.08	-
k_{PREC}	Rate constant of OP -> PP	1.0e-2	day^{-1}
k_{PR}	Coefficient of permanent removal of P	1.09e-5	day^{-1}
Sediments			
OP_S	OP concentration in the pore water of sediment	7.2e2	mg L^{-1}
$NH4_S$	NH4 concentration in the pore water of sediment	1.5e4	mg L^{-1}
r_{PSS}	Constant ratio particulate P of SS	2.5e-3	-
r_{NSS}	Constant ratio particulate N of SS	1.1e-1	-
r_{CSS}	Constant ratio particulate C of SS	4.17e-1	-
r_{PS}	Constant ratio P of Sediment	9.2e-4	-
r_{NS}	Constant ratio N of Sediment	3.25e-2	-
ρ_s	Sediment density	2.65e3	kg m^{-3}
S_P	Sediment release rate of OP	9.2	µg m^{-2} d^{-1}
S_N	Sediment release rate of NH4	35	µg m^{-2} d^{-1}
θ_{SED}^{T-20}	Non-dimensional temperature multipliers of sediment	1.08	-
Dpref	Mixing depth threshold	6	m
ρ_b	Bulk density	1.2e3	kg m^{-3}
Sediment model			
F	Fetch	30	km
α	Sediment resuspension constant	2.35	-
n	Sediment resuspension exponent	2.0	-
τ_{cr}	Critical shear stress	4.0e-2	Pa

Table 4.4 The coefficients, constants and forcing parameters of DLM–WQ with the sediment resuspension model of a linear relation (Bowie et al., 1985; Losada, 2001).

Symbols	Description	Calibrated Value	Units
Phytoplankton			
G_{MAX}	Maximum growth rate of phytoplankton	6.1	day^{-1}
k_{RESP}	Respiration rate of phytoplankton	0.125	day^{-1}
k_{MORT}	Mortality of phytoplankton	0.02	day^{-1}
θ_{Chla}^{T-20}	Non-dimensional temperature multipliers of phytoplankton	1.068	-
a_P	Constant ratio of phosphorous to chlorophyll *a*	0. 75	-
a_N	Constant ratio of nitrogen to chlorophyll *a*	13.0	-
a_C	Constant ratio of carbon to chlorophyll *a*	61.0	-
$k_{NO3+NH4}$	Half saturation constant of nitrogen	55.0	$\mu g\ L^{-1}$
k_{OP}	Half saturation constant of phosphorous	3.0	$\mu g\ L^{-1}$
I_{SAT}	Saturation light intensity	60.0	Watt m^{-2}
Light attenuation coefficients			
etca	Light attenuation coefficient for chlorophyll *a*	0.017	m^{-1}
etpart	Light attenuation coefficient for particles	0.025	m^{-1}
Settling velocity			
W_{Chla}	Settling velocity of chlorophyll *a*	1.0	m day^{-1}
W_{PN}	Settling velocity of PN	1.0	m day^{-1}
W_{PP}	Settling velocity of PP	2.0	m day^{-1}
W_{SS}	Settling velocity of SS	3.5	m day^{-1}
Chemical constants			
$S_{B,20}$	Areal SOD rate at 20°C	0.2	$mg\ L^{-1}$
θ_{SD}^{T-20}	Non-dimensional temperature multipliers of SOD	1.065	-
k_{DEC}	Decomposition rate constant	3.0e-2	day^{-1}
r_{OC}	Ratio of mass of oxygen consumed per mass of carbon assimilated	2.67	$mgO\ mgC^{-1}$
r_{ON}	Amount of oxygen consumed per unit mass of nitrogen oxidized in the total process of nitrification	4.57	$gO\ gN^{-1}$
k_{nitr}	Nitrification inhibition coefficient	0.6	$L\ mg^{-1}$
θ_{DO}^{T-20}	Non-dimensional temperature multipliers of reactions	1.08	-
k_{AMM}	Ammonification rate constant	6.9e-2	day^{-1}
k_{NIT}	Nitrification rate constant of NH4	4.0e-2	day^{-1}
k_{DNT}	Denitrification rate constant of NO3	2.5e-1	day^{-1}
θ_{RXN}^{T-20}	Non-dimensional temperature multipliers of reactions	1.08	-
k_{PREC}	Rate constant of OP -> PP	7.5e-2	day^{-1}
k_{PR}	Coefficient of permanent removal of P	1.09e-5	day^{-1}
Sediments			
OP_S	OP concentration in the pore water of sediment	1.5e3	$mg\ L^{-1}$
$NH4_S$	NH4 concentration in the pore water of sediment	2.55e4	$mg\ L^{-1}$
r_{PSS}	Constant ratio particulate P of SS	2.5e-3	-
r_{NSS}	Constant ratio particulate N of SS	1.1e-1	-
r_{CSS}	Constant ratio particulate C of SS	4.17e-1	-
r_{PS}	Constant ratio P of Sediment	6.41e-4	-
r_{NS}	Constant ratio N of Sediment	3.2e-2	-
ρ_s	Sediment density	2.65e3	$kg\ m^{-3}$
S_P	Sediment release rate of OP	1.66	$\mu g\ m^{-2}\ d^{-1}$

S_N	Sediment release rate of NH4	30	$\mu g\ m^{-2}\ d^{-1}$
θ_{SED}^{T-20}	Non-dimensional temperature multipliers of sediment	1.08	-
Dpref	Mixing depth threshold	6	m
ρ_b	Bulk density	1.2e3	$kg\ m^{-3}$
Sediment model			
F	Fetch	30	km
M	Sediment resuspension constant	7.5e-2	-
n	Sediment resuspension exponent	1.0	-
τ_{cr}	Critical shear stress	4.0e-2	Pa

Table 4.4 The coefficients, constants and forcing parameters of DLM–WQ with the sediment resuspension model of an extended García and Parker (Bowie et al., 1985; Losada, 2001)**.**

Symbols	Description	Calibrated Value	Units
Phytoplankton			
G_{MAX}	Maximum growth rate of phytoplankton	6.0	day^{-1}
k_{RESP}	Respiration rate of phytoplankton	0.12	day^{-1}
k_{MORT}	Mortality of phytoplankton	0.03	day^{-1}
θ_{Chla}^{T-20}	Non-dimensional temperature multipliers of phytoplankton	1.068	-
a_P	Constant ratio of phosphorous to chlorophyll *a*	0. 75	-
a_N	Constant ratio of nitrogen to chlorophyll *a*	13.0	-
a_C	Constant ratio of carbon to chlorophyll *a*	61.0	-
$k_{NO3+NH4}$	Half saturation constant of nitrogen	55.0	$\mu g\ L^{-1}$
k_{OP}	Half saturation constant of phosphorous	3.0	$\mu g\ L^{-1}$
I_{SAT}	Saturation light intensity	86.0	$Watt\ m^{-2}$
Light attenuation coefficients			
etca	Light attenuation coefficient for chlorophyll *a*	0.015	m^{-1}
etpart	Light attenuation coefficient for particles	0.02	m^{-1}
Settling velocity			
W_{Chla}	Settling velocity of chlorophyll *a*	1.0	$m\ day^{-1}$
W_{PN}	Settling velocity of PN	1.0	$m\ day^{-1}$
W_{PP}	Settling velocity of PP	2.75	$m\ day^{-1}$
W_{SS}	Settling velocity of SS	3.5	$m\ day^{-1}$
Chemical constants			
$S_{B,20}$	Areal SOD rate at 20°C	0.2	$mg\ L^{-1}$
θ_{SD}^{T-20}	Non-dimensional temperature multipliers of SOD	1.065	-
k_{DEC}	Decomposition rate constant	2.8e-2	day^{-1}
r_{OC}	Ratio of mass of oxygen consumed per mass of carbon assimilated	2.67	$mgO\ mgC^{-1}$
r_{ON}	Amount of oxygen consumed per unit mass of nitrogen oxidized in the total process of nitrification	4.57	$gO\ gN^{-1}$
k_{nitr}	Nitrification inhibition coefficient	0.6	$L\ mg^{-1}$
θ_{DO}^{T-20}	Non-dimensional temperature multipliers of reactions	1.08	-
k_{AMM}	Ammonification rate constant	6.5e-2	day^{-1}
k_{NIT}	Nitrification rate constant of NH4	3.0e-2	day^{-1}
k_{DNT}	Denitrification rate constant of NO3	5.5e-1	day^{-1}

θ_{RXN}^{T-20}	Non-dimensional temperature multipliers of reactions	1.08	-
k_{PREC}	Rate constant of OP -> PP	2.5e-2	day^{-1}
k_{PR}	Coefficient of permanent removal of P	1.09e-5	day^{-1}
Sediments			
OP_S	OP concentration in the pore water of sediment	1.1e3	$mg\ L^{-1}$
$NH4_S$	NH4 concentration in the pore water of sediment	6.5e4	$mg\ L^{-1}$
r_{PSS}	Constant ratio particulate P of SS	2.5e-3	-
r_{NSS}	Constant ratio particulate N of SS	1.1e-1	-
r_{CSS}	Constant ratio particulate C of SS	4.17e-1	-
r_{PS}	Constant ratio P of Sediment	1.2e-3	-
r_{NS}	Constant ratio N of Sediment	3.95e-2	-
ρ_s	Sediment density	2.65e3	$kg\ m^{-3}$
S_P	Sediment release rate of OP	4.5	$\mu g\ m^{-2}\ d^{-1}$
S_N	Sediment release rate of NH4	16	$\mu g\ m^{-2}\ d^{-1}$
θ_{SED}^{T-20}	Non-dimensional temperature multipliers of sediment	1.08	-
Dpref	Mixing depth threshold	6	m
ρ_b	Bulk density	1.2e3	$kg\ m^{-3}$
Sediment model			
F	Fetch	30	km
SD	Sediment diameter	25	μm

The output of DLM–WQ with each of the four sediment resuspension models was compared against the measured data based on the statistical evaluation methods described previously. Results are presented in Tables 4.6 and 4.7 of the model evaluation of simulated water quality state variables, including chlorophyll *a*, DO, OP, PP, NO3, NH4, PN, and TSS at the surface (14 m from bottom) and at the bottom (1 m from bottom except chlorophyll *a* whish is 7 m from the bottom, the only data available for the Sea).

DLM–WQ using the sediment resuspension of Somlyody (1986) shows the lowest values of *RMSE* and *STD* of five state variables at the surface (DO, OP, NH4, PN, and TSS) and four at the bottom (DO, NH4, PN, and TSS), as indicated by the least residual errors in model performance for these water quality variables. However, sample autocorrelations of the residual errors are positive for some variables, such as chlorophyll *a* and NH4 at the surface and chlorophyll *a*, PP, and TSS at the bottom, which means that the model results violate the assumption of uncorrelated residual errors. Furthermore, the values of *t*–tests indicate a statistically significant predictive bias in OP and NH4 at the surface as well as PP and TSS at the bottom (i.e. $|t| > 2.11$). The statistics indicate that the model using Somlyody (1986) is not able to capture all of the significant features of water quality since residual errors are correlated and predictive biases are significant.

DLM–WQ using the sediment resuspension of Mian and Yanful (2004) shows the highest values of *RMSE* and *STD* of six state variables at the surface (e.g. chlorophyll *a*, DO, PP, NH4, PN, and TSS) and four at the bottom (e.g. DO, OP, PN, and TSS), as indicated by high residual errors in the model performance. Sample autocorrelations of the residual errors also indicate positive for several variables, including NH4 and PN at the surface and chlorophyll *a* at the bottom. Moreover, the *t*–test indicates statistically

significant predictive bias in NH4 and PN at the surface. Therefore, the model performed more poorly than other models in terms of *RMSE* and *STD* . Sample autocorrelations and *t*–tests also indicate that the model performance is not able to capture all the significant features of water quality.

Table 4.6 Statistical comparison of DLM–WQ with sediment resuspension models, based on the 2–4 weekly values (1999) of chlorophyll ***a*** (Chl-***a***), dissolved oxygen (DO), ortho phosphate (OP), particulate phosphorus (PP), nitrate (NO3), ammonium (NH4), particulate nitrogen (PN) and total suspended sediment (TSS) of the epilimnion of the Salton Sea.

	Chl-*a*	DO	OP	PP	NO3	NH4	PN	TSS
Somlyody								
RMSE	0.572	0.399	1.564	0.927	0.947	0.832	0.351	0.696
STD	0.131	0.097	0.379	0.225	0.230	0.202	0.085	0.169
Autocorrelation	YES	NO	NO	NO	NO	YES	NO	NO
t–test	-0.759	1.714	2.178	-0.786	0.159	2.378	-0.245	0.168
Mian & Yanful								
RMSE	0.672	0.547	1.600	1.074	0.800	0.952	0.586	1.019
STD	0.154	0.133	0.388	0.261	0.194	0.231	0.142	0.247
Autocorrelation	NO	NO	NO	NO	NO	YES	YES	NO
t–test	0.934	1.634	2.087	1.145	1.805	2.539	2.313	1.337
Linear relation								
RMSE	0.506	0.504	1.584	0.855	1.000	0.859	0.453	0.850
STD	0.116	0.122	0.384	0.207	0.242	0.208	0.110	0.206
Autocorrelation	NO	YES	NO	NO	NO	NO	NO	NO
t–test	-0.974	1.597	2.088	0.267	-0.255	1.649	1.886	1.629
Garcia & Parker								
RMSE	0.588	0.470	1.608	1.055	0.954	0.866	0.544	0.939
STD	0.135	0.114	0.390	0.256	0.231	0.210	0.132	0.228
Autocorrelation	NO	NO	NO	NO	NO	NO	NO	NO
t–test	-0.172	1.344	2.046	0.499	-0.793	0.786	1.279	1.738

DLM–WQ with the linear relation for cohesive sediments produces the smallest values of *RMSE* and *STD* in several water quality variables, such as chlorophyll *a* and NO3 at the surface as well as chlorophyll *a*, OP and PP at the bottom. Sample autocorrelations of the residual errors indicate positive values only for DO at the surface. The *t*–tests indicate no statistically significant predictive bias for any of the water quality variables. Therefore, the calibrated model with the linear relation performed better than with Mian and Yanful (2004) for cohesive sediments.

DLM–WQ with the extended relation of García and Parker shows the greatest values of *RMSE* and *STD* for three water quality variables (e.g. OP at the surface and chlorophyll *a* and PP at the bottom). However, these values are not much different than the lowest values of *RMSE* and *STD* of these variables. For example the differences are 0.044, 0.12 and 0.192 for OP at the surface and chlorophyll *a* and PP at the bottom, respectively. The residual errors in the model performance also show that all variables are

uncorrelated. In addition, there is no statistically significant predictive bias according to the *t*–tests. Therefore, DLM–WQ combined with the extended relation of García and Parker for the Salton Sea represents the best fit to the measured data among the four models.

Table 4.7 Statistical comparison of DLM–WQ with sediment resuspension models, based on the 2–4 weekly values (1999) of chlorophyll ***a*** (Chl-***a***), dissolved oxygen (DO), ortho phosphate (OP), particulate phosphorus (PP), nitrate (NO3), ammonium (NH4), particulate nitrogen (PN) and total suspended sediment (TSS) of the hypolimnion of the Salton Sea.

	Chl-*a*	DO	OP	PP	NO3	NH4	PN	TSS
Somlyody								
RMSE	0.563	0.827	1.433	0.989	1.122	1.034	0.375	0.713
STD	0.129	0.201	0.348	0.240	0.272	0.251	0.091	0.173
Autocorrelation	YES	NO	NO	YES	NO	NO	NO	YES
t–test	0.169	-1.021	1.920	-2.140	-1.193	-0.254	-0.768	-2.265
Mian & Yanful								
RMSE	0.590	1.470	1.533	0.990	0.980	1.067	0.594	1.112
STD	0.135	0.356	0.372	0.240	0.238	0.259	0.144	0.270
Autocorrelation	YES	NO	NO	NO	NO	NO	NO	NO
t–test	1.643	-1.478	1.904	0.289	-0.107	0.499	1.838	0.159
Linear Relation								
RMSE	0.477	1.222	1.405	0.811	1.248	1.191	0.487	0.727
STD	0.109	0.296	0.341	0.197	0.303	0.289	0.118	0.176
Autocorrelation	NO	NO	NO	NO	NO	NO	NO	NO
t–test	-0.168	-0.558	1.732	-1.612	-1.709	-0.589	1.156	-0.201
Garcia & Parker								
RMSE	0.597	1.391	1.499	1.003	1.054	1.116	0.591	0.792
STD	0.137	0.337	0.363	0.243	0.256	0.271	0.143	0.192
Autocorrelation	NO	NO	NO	NO	NO	NO	NO	NO
t–test	0.393	-1.907	1.878	-0.959	-1.549	-0.580	0.931	0.649

A graphically comparison of the performances of the four models with the measured data of each water quality variable using box plots is provided in Figures 4.13 and 4.14. At the surface (Figure 4.13), Somlyody (1986) has two state variables for which the notches about the medians of the model simulations and the measured values do not overlap (e.g. OP and NH4). Mian and Yanful (2004) has four variables including OP, NH4, PN and TSS for which the notches about the medians do not overlap. The linear relation and García and Parker (1993) have two variables (e.g. OP and TSS) for which the notches about the medians do not overlap.

At the bottom (Figure 4.14), Somlyody (1986) has three state variables for which the notches about the medians of the simulation outputs and the measured data do not overlap (i.e. PP, NH4 and TSS). Mian and Yanful (2004) has two state variables for which the notches about the medians of the simulation and measured values do not overlap (i.e. OP and NH4). However, the notches about two medians overlap all the state variables of the linear relation and the extended García and Parker. Therefore, the

graphical comparison using box plots demonstrates that the performances of DLM–WQ with the linear relation and the extended García and Parker are the best among the other sediment models.

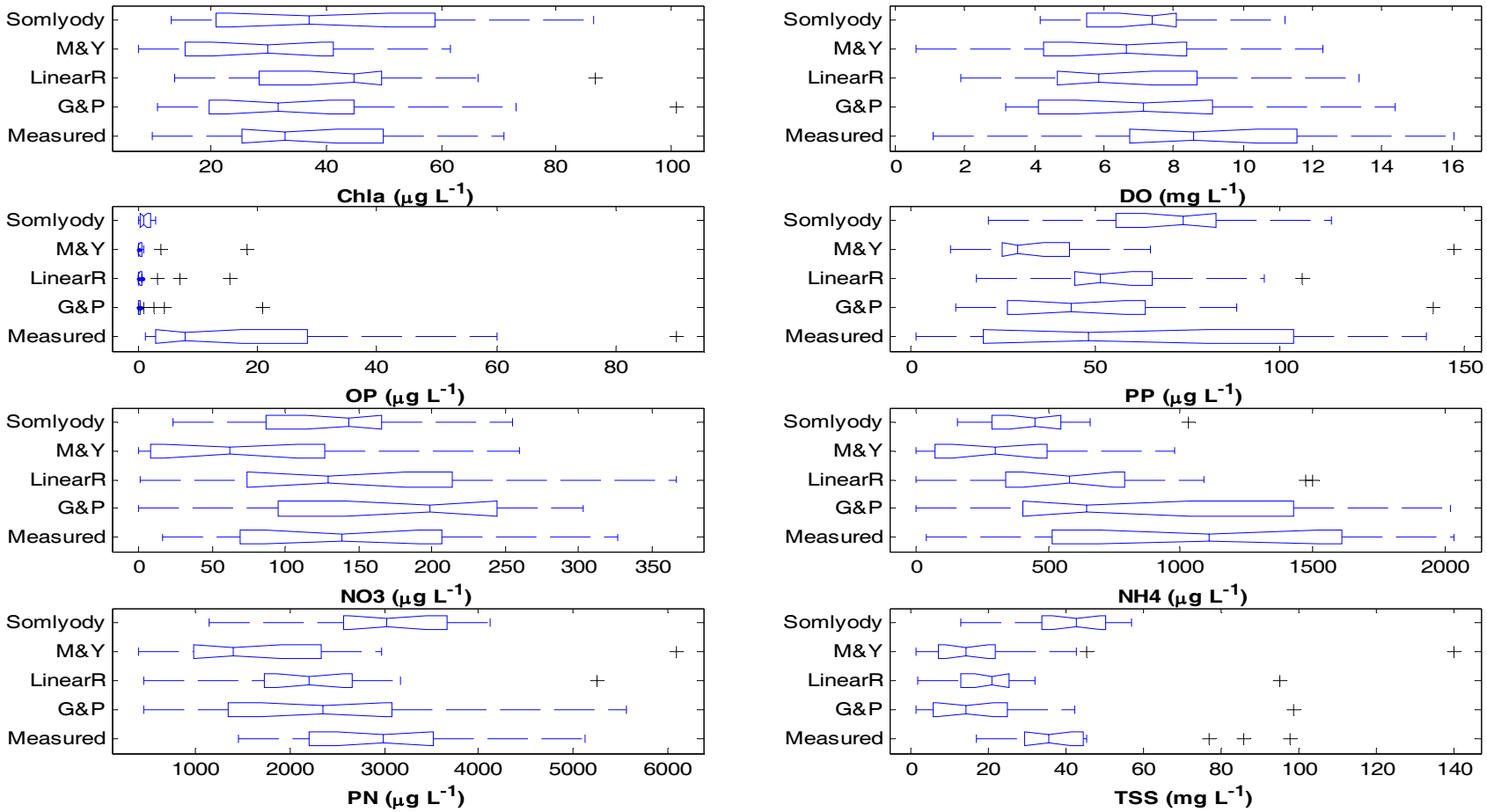

Figure 4.13 Comparison of box plots of water quality state variables, including chlorophyll ***a***, DO, OP, PP, NO3, NH4, PN, and TSS, among the measured at the surface and the simulated of the Salton Sea by DLM–WQ with Somlyody (1986), Mian and Yanful (2004), a linear relation for cohesive sediments, and the extended relation of García and Parker (1993) at surface in 1999. The upper and lower hinges present the inter-quartile ranges, a vertical line in the box indicates the median, and notches indicate the relative statistical significance of the median, and crosses denotes outliers (McGill et al., 1978; Reckhow, 1980).

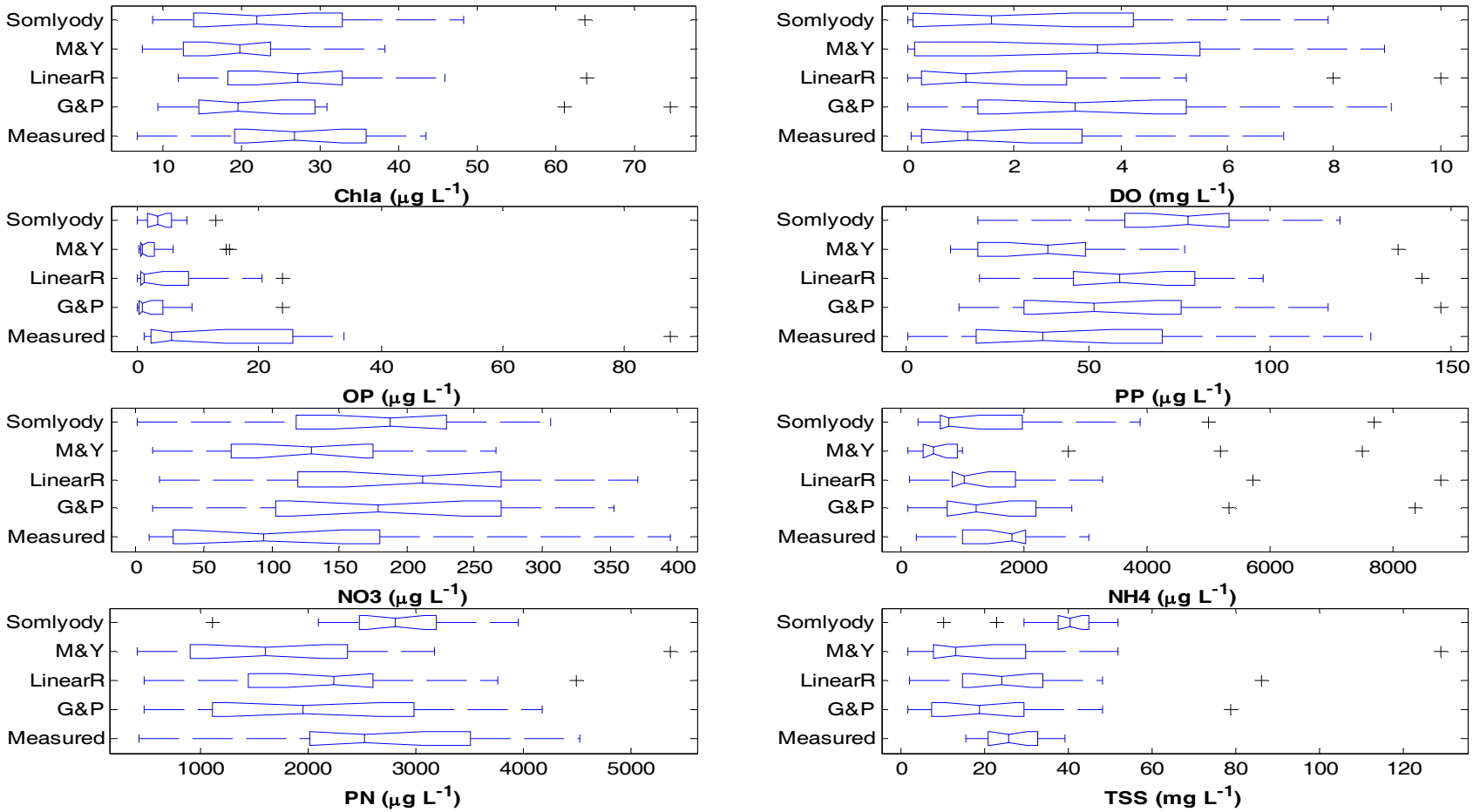

Figure 4.14 Comparison of box plots of water quality state variables, including chlorophyll ***a***, DO, OP, PP, NO3, NH4, PN, and TSS, among the measured at the bottom and the simulated of the Salton Sea by DLM–WQ with Somlyody (1986), Mian and Yanful (2004), a linear relation for cohesive sediments, and the extended relation of García and Parker (1993) at bottom in 1999. The upper and lower hinges present the inter-quartile ranges, a vertical line in the box indicates the median, and notches indicate the relative statistical significance of the median, and crosses denotes outliers (McGill et al., 1978; Reckhow, 1980)**.**

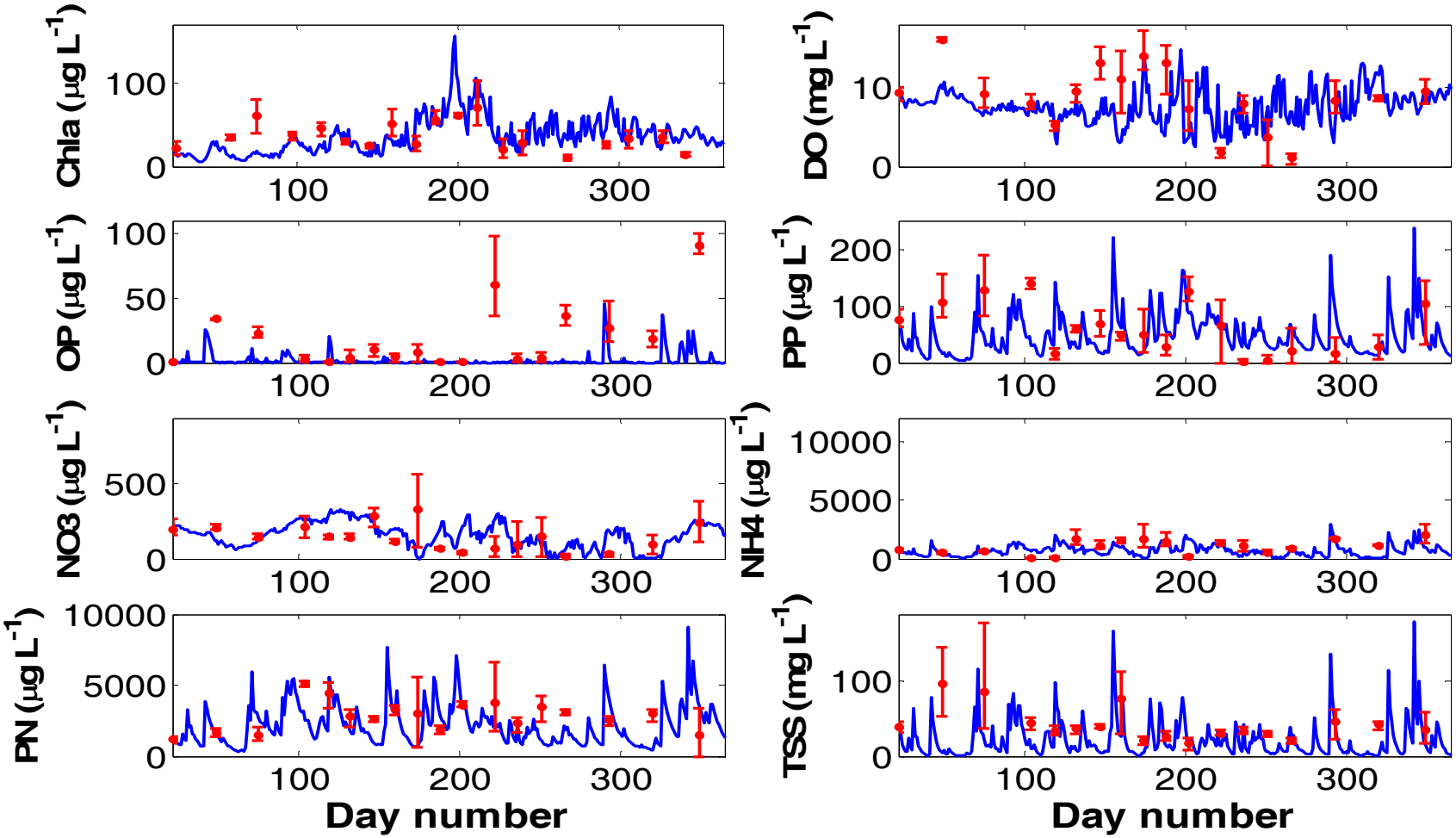

Figure 4.**10** Comparison between measured data (symbols) and simulated data (lines) of water quality state variables, including chlorophyll ***a***, DO, OP, PP, NO3, NH4, PN, and TSS, of the Salton Sea by DLM–WQ with the extended relation of García and Parker (1993) in 1999 at surface. The symbols of the measured values are the average of three stations in the Sea, and their error bars indicate the minimum and the maximum at each sampling date.

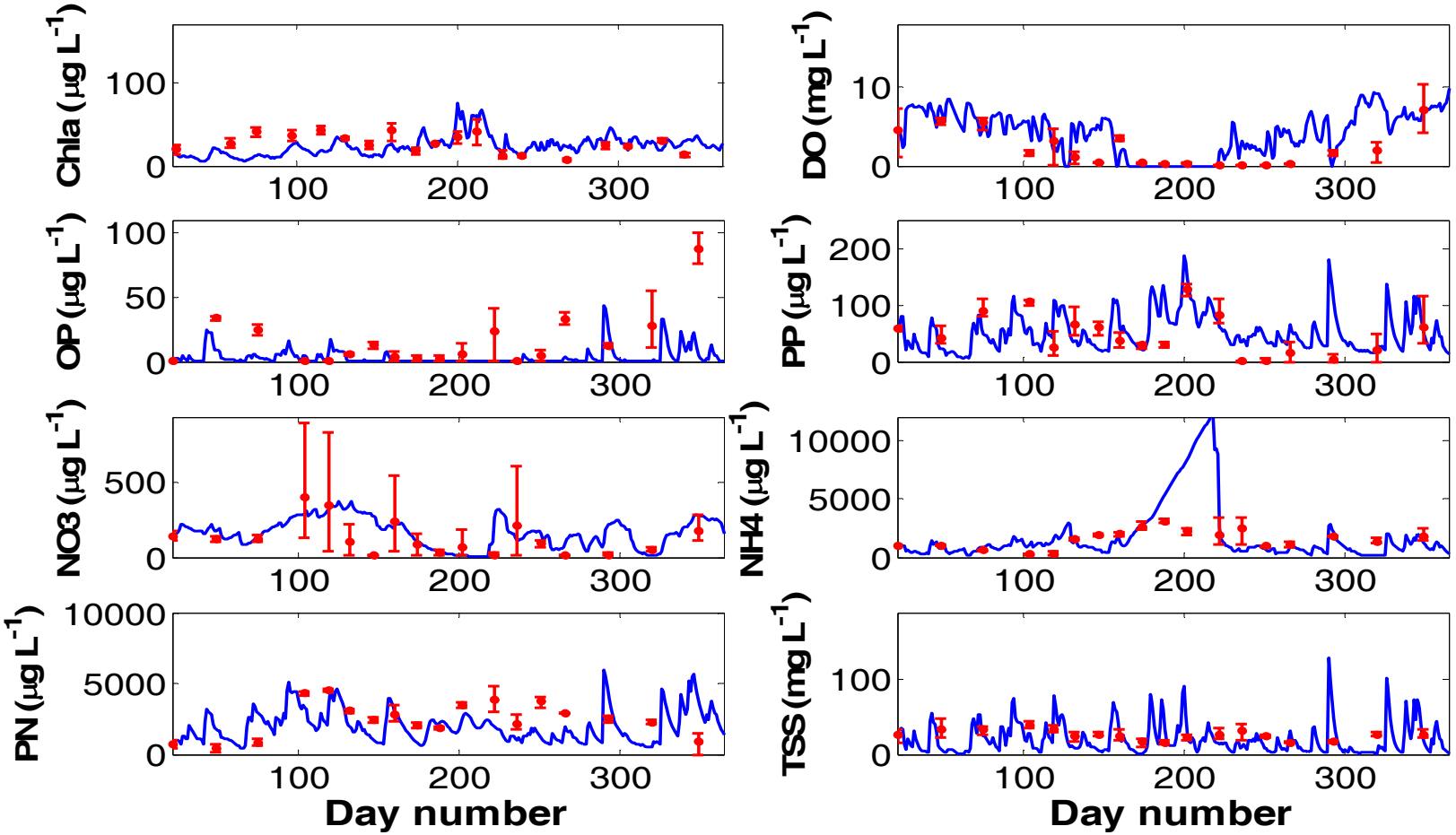

Figure 4.16 Comparison between measured data (symbols) and simulated data (lines) of water quality state variables, including chlorophyll ***a***, DO, OP, PP, NO3, NH4, PN, and TSS, of the Salton Sea by DLM–WQ with the extended relation of García and Parker (1993) in 1999 at 1 m from the bottom except chlorophyll ***a*** (at 7 m from the bottom). The symbols of the measured values are the average of three stations in the Sea, and their error bars indicate the minimum and the maximum at each sampling date.

Model simulation results

Based on the comparison of both statistical evaluation methods and graphical methods, DLM–WQ with the extended relation of García and Parker is considered the best model for describing the Salton Sea. In this section, we present the time series of outputs simulated by the resulting model using meteorological data from CIMIS station #127 in 1999. The simulated model outputs (shown by lines), including chlorophyll *a*, DO, OP, PP, NO3, NH4, PN, and TSS, are compared with the measured data (shown by symbols) at the surface and at the bottom, respectively in Figures 4.15 and 4.16.

The seasonal trends and some of the short term variations of chlorophyll *a*, except algal blooms in the winter, are well captured by the model. The differences between the measured and the simulated chlorophyll *a* concentrations may be due to the use of a single, hypothetical algal species as opposed to individual algal functional groups in the model. However, total chlorophyll *a* concentrations are the only data available for the Sea and there was no basis upon which to derive calibration values for individual functional groups. It is known that the Salton Sea algal population is composed of several functional groups including diatoms and prymnesiophyceae (Reifel et al., 2001; Lange and Tiffany, 2002).

The seasonal trends and short term variations in DO concentration, with the exception of the high concentrations of DO in the winter at the surface (around day 50), are captured fairly well by the model (Figures 4.15 and 4.16). The simulated low concentration of DO concurrent with the high measured DO may result from under-predicting the chlorophyll *a* concentration and thereby under-predicting photosynthetic production of oxygen. Near the bottom, the simulated and the measured DO concentrations demonstrate the occurrence of summer anoxia.

The general trends in the measured and simulated OP concentrations are in fairly good agreement with the exception of the measured high concentrations of OP in the summer and winter at the surface (around days 220 and 350) (Figures 4.15 and 4.16). The trends of the simulated and measured PP concentrations are in fairly good agreement, except measured peaks in the early spring at the surface, which are not captured by the model (Figures 4.15 and 4.16). The difference in the spring may account for the low concentration of chlorophyll *a* at that time. The model shows rapid changes in concentration (from 0 to 220 $\mu g\ L^{-1}$) caused by sediment resuspension, which is the same general range as the measurements. The 2–4 week sampling interval may preclude resolving such events in the field measurements.

The nitrogen model, especially for NH4 and PN, has been refined compared to those produced using by DLM–WQ with the relation of Somlyody (1986). The general trends and short term variations of the simulated NO3 concentration agree fairly well with the measured values (Figures 4.15 and 4.16). High values of NO3 in summer are directly related to the simulated DO and NH4 concentrations because nitrification from NH4 to NO3 does not occur under anoxic conditions, and NH4 is accumulated near the

bottom of the lake. The general trends and short term variations of PN are captured by the model fairly well, except measured low concentration at the bottom in the winter (around day 340) (Figures 4.15 and 4.16). The simulated high concentration of PN at the time may be related to peaks of TSS, because the ratio of nitrogen to TSS is based on an estimation of PN/TSS from Holdren and Montaño (2002), not direct measurement.

The simulated and measured concentrations of TSS demonstrate similar trends in Figures 4.15 and 4.16. It is interesting to notice that the measured points at the bottom mainly lie between the simulated peaks. Care should be taken in interpreting the measured results, because the coarse sampling interval (2–4 weeks), in association with only sampling during calm weather, may obscure intermediate peaks in TSS concentration. Due to safety issues, sampling is commonly conducted under weather conditions when significant sediment resuspension is not usually occurring. Thus, it is expected that the measured values likely under-represent the occurrence of peaks in TSS.

These results show that variations in water quality of the Salton Sea are closely related to the hydrodynamic processes, such as thermal stratification and sediment resuspension. As mentioned previously, if sediment resuspension is a dominant process, then rapid and significant variations are to be expected. From the comparison between the measured and the simulated values produced by DLM–WQ with the extended García and Parker, the model successfully represents the seasonal trends as well as short-term variations, and provides an indication of potential variations in properties that were not able to be measured.

MODEL PERFORMANCE UNDER ALTERNATIVES

The California Department of Water Resources (CDWR) and California Department of Fish and Game (CDFG) developed and proposed eight alternatives to restore important ecological functions of the Salton Sea that have existed for about 100 years. The Draft Programmatic Environmental Impact Report (PEIR) evaluates and analyzes potential environmental impacts of alternatives developed for restoration of the Salton Sea, which is a requirement of the Salton Sea Restoration Act and related legislation, to implement the Colorado River Quantification Settlement Agreement (QSA) (California Department of Water Resources and California Department of Fish and Game, 2006).

In this section, DLM-WQ using the extended García and Parker relationship (demonstrated the best model to describe the measured data) simulates water quality characteristics of two alternatives, including Alternative 6 (North Sea Combined) and Alternative 8 (South Sea Combined) proposed in the PEIR (see Figure 4.17). Graphical locations and bathymetries of these alternatives are quite different from those of the whole Sea. Figure 4.18 compares the areas and volumes of the whole Sea and the modeled two alternatives.

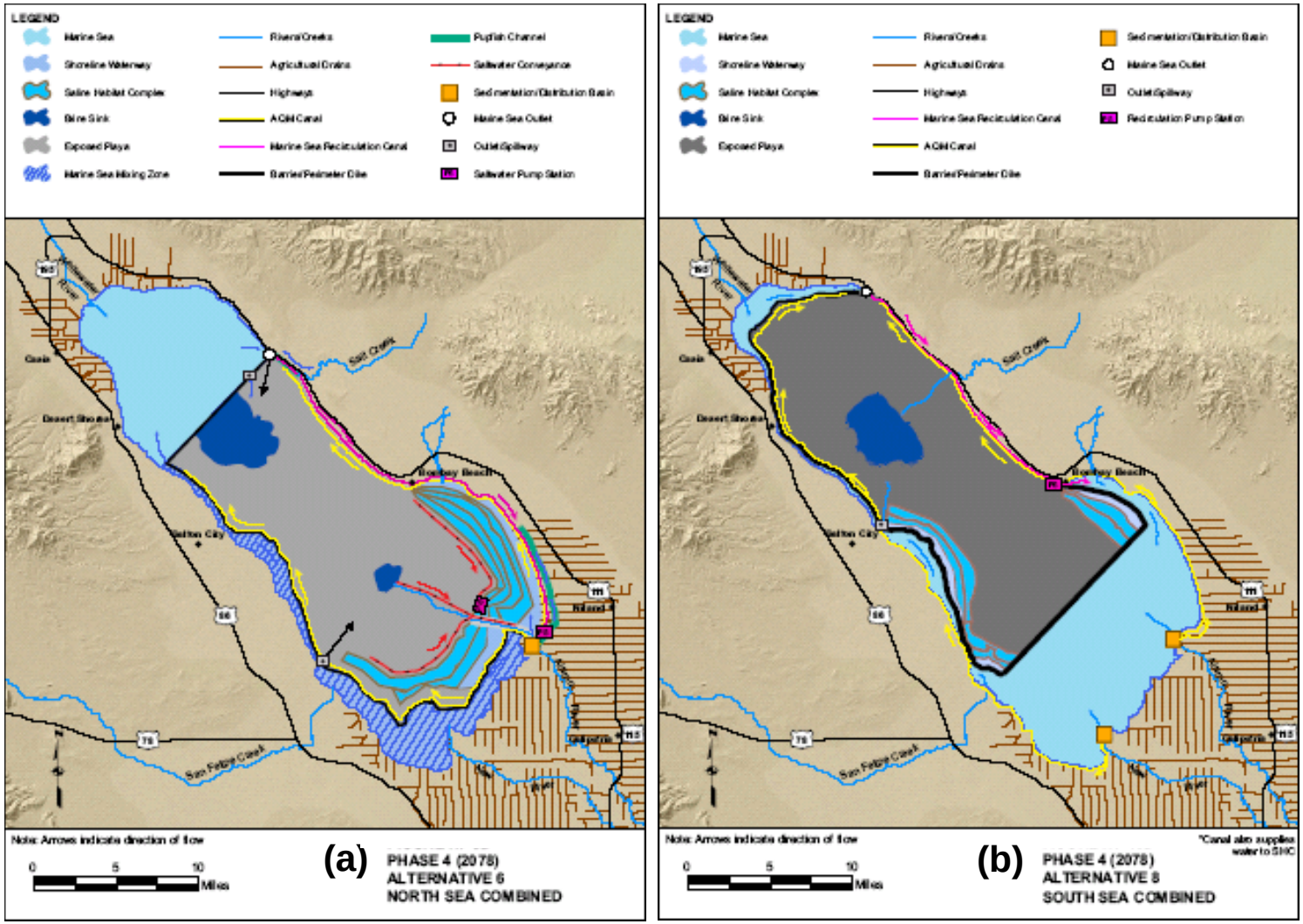

Figure 4.11 Graphic representations of the locations of components at phase 4 (year 2076) of two alternatives of the Salton Sea proposed by the PEIR: (a) Alternative 6; (b) Alternative 8 (Source: CDWR and CDFG, 2006).

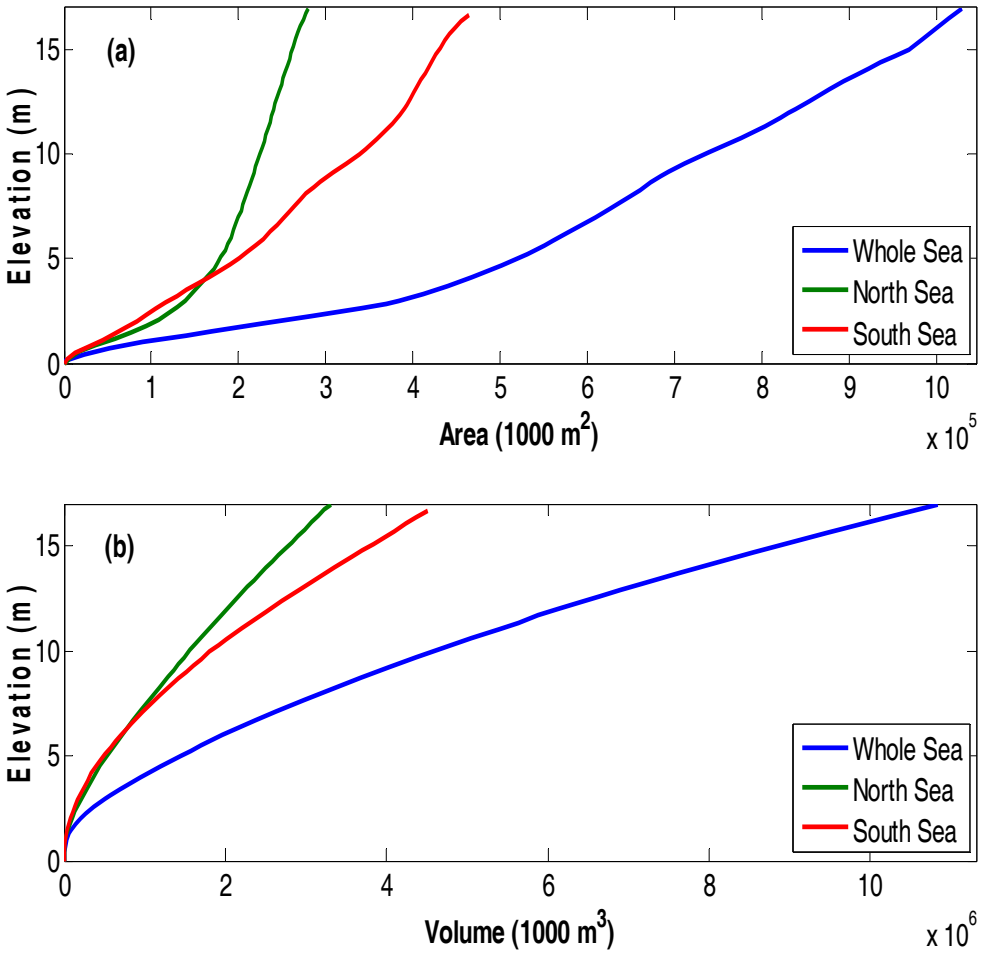

Figure 4.12 Comparison of the areas and volumes among two alternatives, including the North Sea Combined, the South Sea Combined, and the whole Sea: (a) Area (1000 m^2); (b) Volume (1000 m^3).

North Sea Combined

The Marine Sea of the North Sea Combined Alternative (NSCA) is located in the northern portion of Salton Sea and up to near Salt Creek. The alternative is separated by a large Barrier from the Brine Sink with a recirculation lake and a channel in the southern Sea Bed as shown in Figure 4.17(a). The NSCA is designed to accommodate both recreation and an aquatic marine habitat. The water would flow from the northern NSCA through a diversion on the southern portion of the lake to the southern marine water body, then flow back to the NSCA (CDWR and CDFG, 2006).

The water surface and salinity of the NSCA would be maintained at -230 feet MSL and around 35 ppt, respectively. Inflows to the Sea are mainly from two sources, including Whitewater River and combined inflows of New River, Alamo River, direct drains, creek inflows and recirculation flows. Meteorological data from CIMIS Station

154, which is the nearest CIMIS Station around the NSCA, were used for this simulation. In addition, the current water quality of the whole Sea was used as the initial condition for this simulation. The water quality data of Whitewater River remained the same as the condition in year 1999 simulation; while those of combined inflows were the average of New River and Alamo River data.

The graph in Figure 4.19 represents the simulated depth-time contours of the NSCA in 1999. Thermal stratification of the NSCA lasts longer in summer, such as from day 165 to day 265, than that of the whole Sea (Figure 4.19(a)). The maximum and minimum temperatures of the NSCA were also lower than those of the whole Sea by about 1 °C. The longer stratification period may be caused by the reduced surface inputs of heat and momentum and shear production, since the area and the volume of the NSCA are reduced to only about 20% and 25%, respectively, of the whole Sea at 14 m elevation while the water depth of the NSCA is decreased only by about 1 m compared with that of the whole Sea. In addition, wind speed data from CIMIS Station 154 were lower than those of other stations, such as Station 127 and 128 (see CDWR and CDFG (2006)).

Based on this thermal stratification of the NSCA, simulated bottom concentrations of chlorophyll *a* reach a minimum concentration, and DO and NO3 are depleted, and OP is sequestered for longer period compared to the whole Sea case (Figure 4.19(b)-(d),(f)). However, NH4 is accumulated near the bottom during the longer stratification period, and then released right after the stratification breaks up (Figure 4.19(d)). Sediment resuspension maintains relatively high concentrations of OP, PP, NO3, NH4, PN, and SS in this simulation; however, the maximum concentrations are 2–5 times lower than those of the whole Sea (Figure 2.19(d)-(i)). In terms of eutrophication, the NSCA might have a better eutrophic status than that of the whole Sea. The stronger stratification and the fewer wind storm events do not allow the sediment resuspension to occur as often as in the whole Sea. Therefore, algal blooms of the NSCA are expected less frequently than those of the whole Sea. However, the toxic substances and organic materials, such as hydrogen sulfide, which accumulate during the anoxic periods when the NSCA is stratified, can be released right after the stratification of the Sea is mixed.

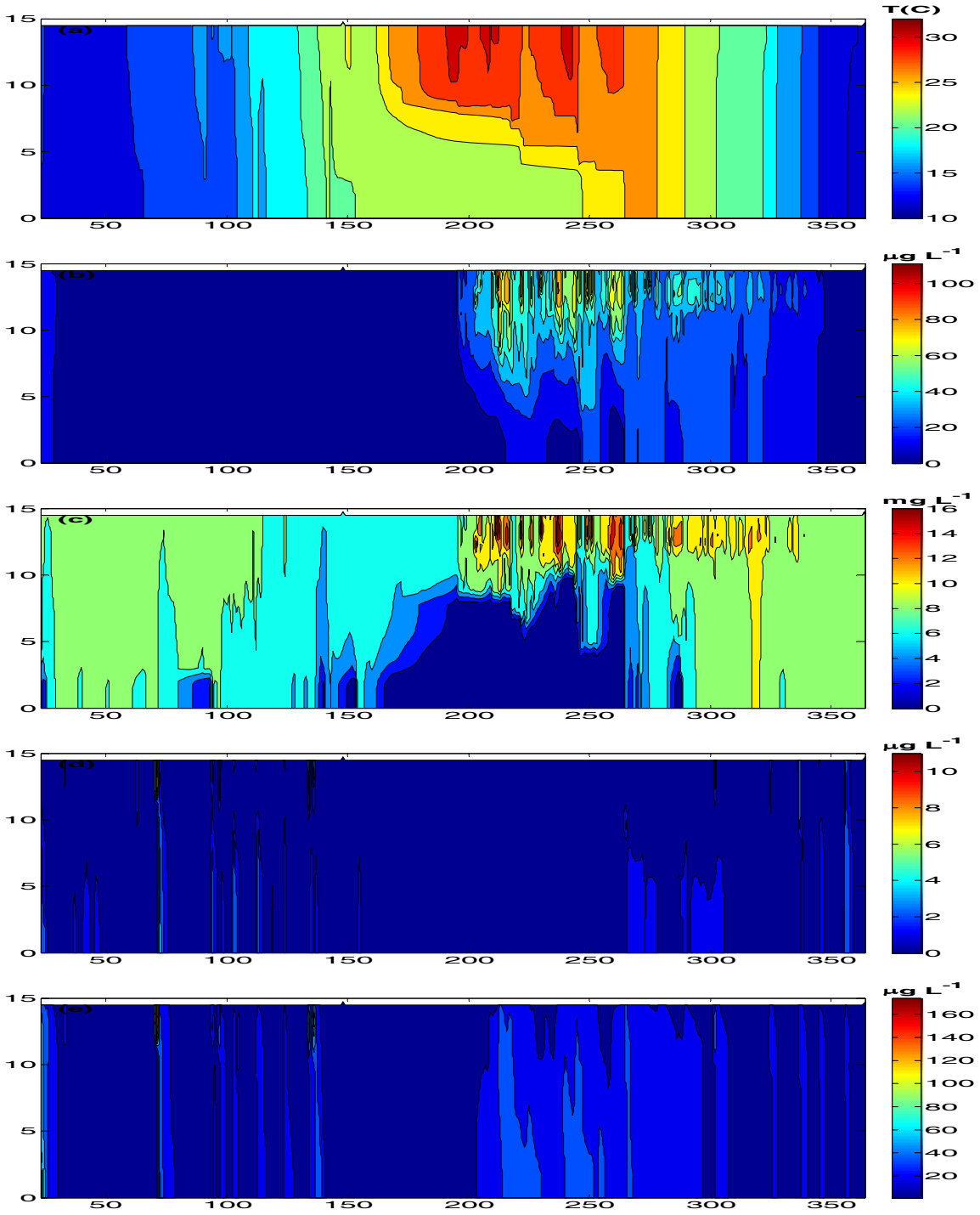

Figure 4.13 Simulated time-elevation contour of NSCA by DLM-WQ with García and Parker (1991; 1993) in 1999: (a) Temperature; (b) Chlorophyll a; (c) **DO; (d) OP**; (e) PP; (f) NO3; (g) NH4; (h) PN; (i) SS.

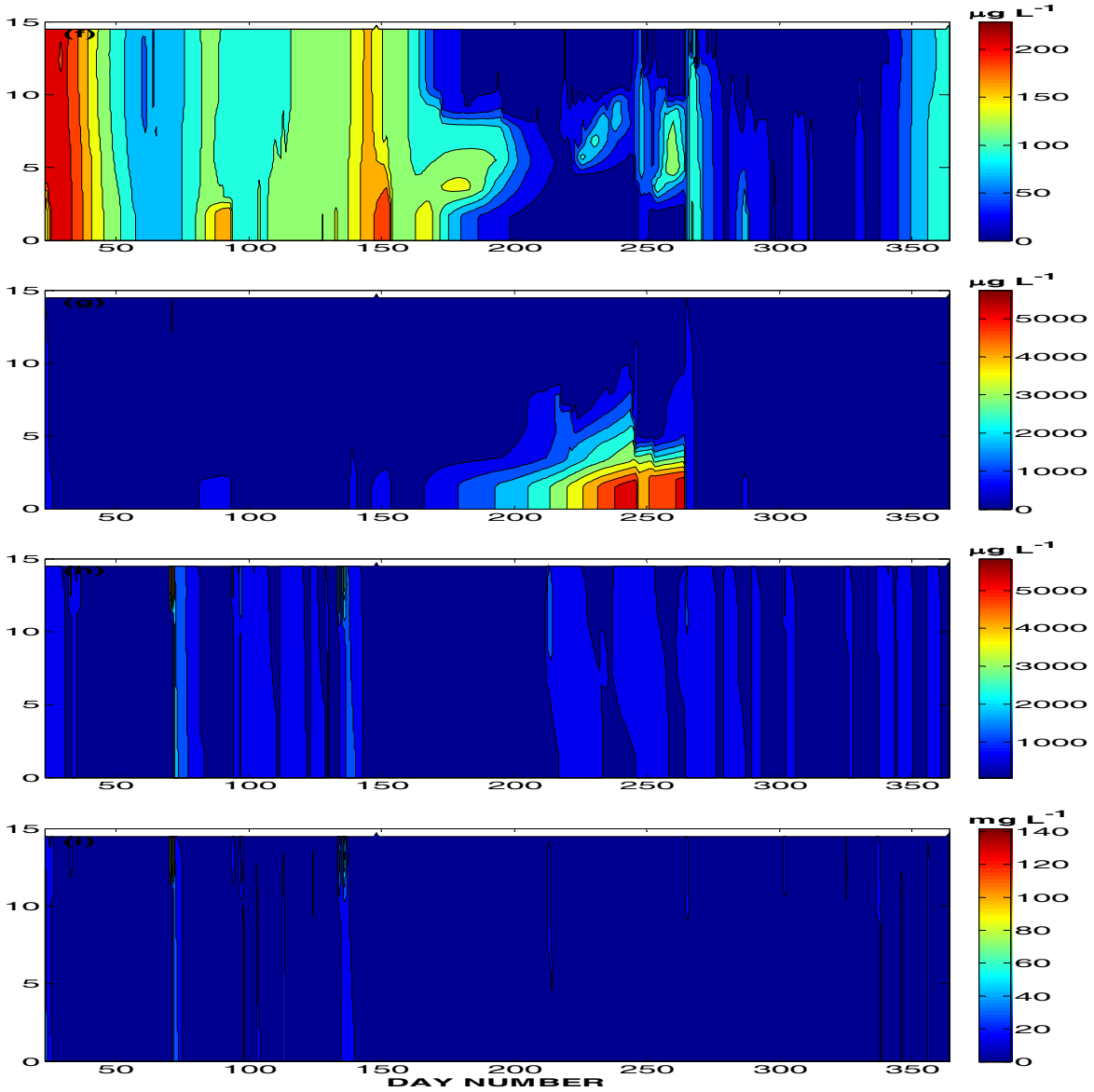

Figure 4.19 (continued) Simulated time-elevation contour of NSCA by DLM-WQ with García and Parker (1991; 1993) in 1999: (a) Temperature; (b) Chlorophyll a; (c) DO; (d) OP; (e) PP; (f) NO3; (g) NH4; (h) PN; (i) SS.

South Sea Combined

The Marine Sea of the South Sea Combined, Alternative (SSCA) is located in the southern portion of the Salton Sea and up to near Bombay Beach, is separated by a large Barrier from the Brine Sink and with a recirculation lake and a channel in the southern Sea Bed shown in Figure 4.17(b). The water of the SSCA would be pumped and conveyed through a channel to the small northern lake, and then flow back into the southern SSCA. This alternative is also designed for recreation and an aquatic marine habitat. The water surface of the SSCA would be maintained at -230 feet MSL, be up to

45 feet in depth and its salinity would be at around 35 ppt. Inflows to the SSCA are assumed to be the same as those of the NSCA (CDWR and CDFG, 2006).

Meteorological data from Station 128, which is the nearest CIMIS Station to the SSCA, were used for this simulation. In addition, the water quality of the current whole Sea was assumed as the initial condition for this simulation. The water quality data of Whitewater River remained the same as in year 1999 simulation, while those of combined inflows were the average of New River and Alamo River data like the NSCA.

The simulated depth-elevation contours of the SSCA in 1999 are shown in Figure 4.20. Thermal stratification of the SSCA lasts longer, such as from day 165 to day 245, than that of the whole Sea by 20-25 days (Figure 4.20(a)). The maximum temperatures of the SSCA and the whole Sea are almost the same, but the minimum of the SSCA is lower than that of the whole Sea by 1.5 °C. The period of summer stratification is longer than that of the whole Sea, but shorter than that of the NSCA, since the area and the volume of the SSCA are larger than those of the NSCA while the water depth of the SSCA is relatively shallow. For example, the area and the volume of the SSCA at 13m elevation are about 40% and about 30% of the whole Sea, respectively. In addition, relatively high wind speed data from CIMIS Station 128 could keep the SSCA less strongly stratified.

Based on this thermal stratification of the SSCA, the simulated bottom concentrations of DO and NO3 are depleted, and OP is sequestered as the cases of the NSCA alternative and the whole Sea (Figure 4.20(c)-(d),(f)). NH4 is also accumulated near the bottom during the stratification period, and then released during periods of mixing events which break up the stratification (Figure 4.20(d)). However, the concentrations of all water quality variables are much higher than those of the NSCA, and of the same magnitude as those of the whole Sea, even though the thermal stratification persists longer than for the whole Sea. These high concentrations of water quality variables are mainly caused by the shallower water depth and by strong wind events (Figure 4.20(b)-(i)).

The SSCA simulation indicates that the concentrations of nutrients in the water column would be the same or higher than those of the whole Sea, and the eutrophication status of the SSCA would be the similar to that of the whole Sea. Furthermore, the anoxia in the hypolimnion would be spatially and temporally increased due to longer stratification periods. Therefore, high toxic materials accumulated in the sediments during summer stratification could be released from sediments when the Sea mixes.

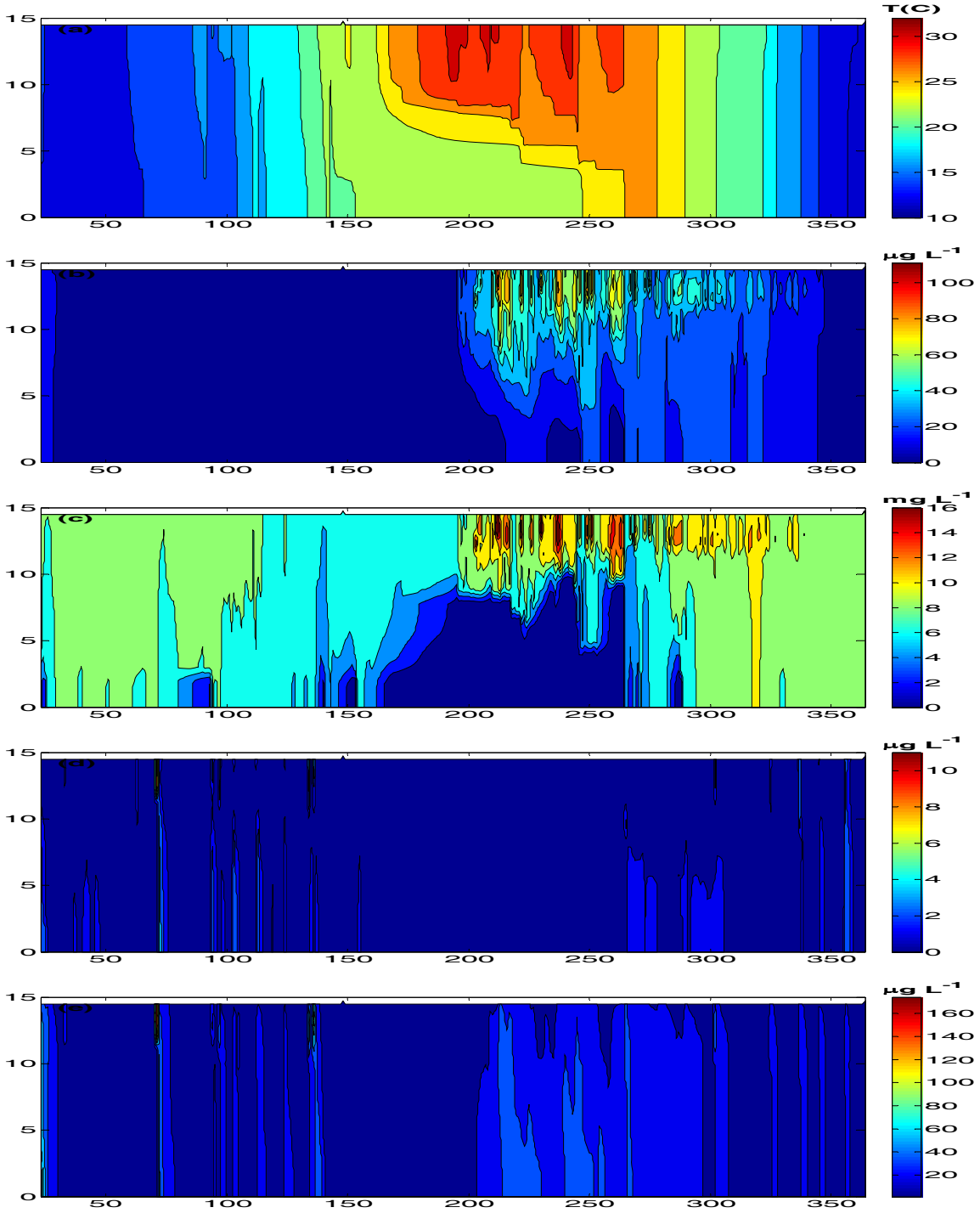

Figure 4.14 Simulated time-elevation contour of SSCA by DLM-WQ with García and Parker (1991; 1993) in 1999: (a) Temperature; (b) Chlorophyll a; (c) DO; (d) OP**;** (e) PP; (f) NO3; (g) NH4; (h) PN; (i) SS.

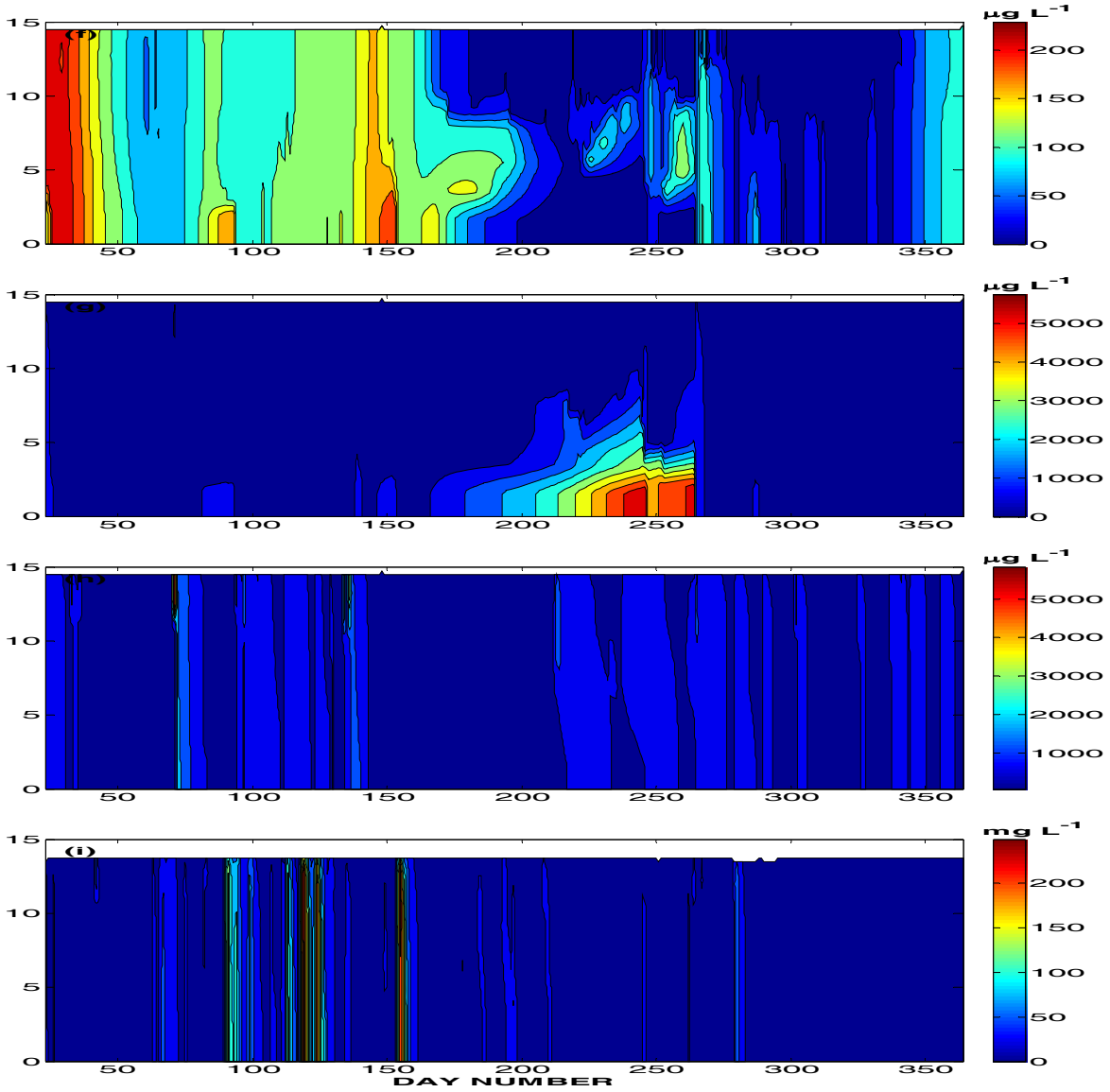

Figure 4.20 (continued) Simulated time-elevation contour of SSCA by DLM-WQ with García and Parker (1991; 1993) in 1999: (a) Temperature; (b) Chlorophyll a; (c) DO; (d) OP; (e) PP; (f) NO3; (g) NH4; (h) PN; (i) SS.

References

Abraham, B., and Ledolter, J. 1983. Statistical methods for forecasting. John Wiley & Sons.

Arhonditsis, G. B., and Brett, M. T. 2005. Eutrophication model for Lake Washington (USA) Part II - model calibration and system dynamics analysis. Ecological Modelling **187:** 179-200.

Bowie, G. L., Mills, W. B., Porcella, D. B., Campbell, C. L., Pagenkopf, J. R., Rupp, G. L., Johnson, K. M., Chan, P. W. H., and Gherini, S. A. 1985. Rates, Constants, and Kinetics Formulations in Surface Water Quality Modeling. U.S. EPA.

California Department of Water Resources, and California Department of Fish and Game. 2006. Salton Sea Ecosystem Restoration Program Draft Programmatic Environmental Impact Report. State of California The Resources Agency.

CDWR, and CDFG. 2006. Salton Sea Ecosystem Restoration Program Draft Programmatic Environmental Impact Report. State of California The Resources Agency.

Chapra, S. C. 1997. Surface Water-Quality Modeling. McGraw-Hill Companies, Inc.

Chung, E. G., Schladow, S. G., Losada, J. P., and Robertson, D. M. in press. A linked hydrodynamic and water quality model for the Salton Sea. Hydrobiologia.

Cook, C. B. 2000. Internal dynamics of terminal basin lake: A numerical model for management of the Salton Sea. Ph.D. dissertation. University of California.

Cook, C. B., Orlob, G. T., and Huston, D. W. 2002. Simulation of wind-driven circulation in the Salton Sea: implications for indigenous ecosystems. Hydrobiologia **473:** 59-75.

Gowland, J. E., Mehta, A. J., Stuck, J. D., John, C. V., and Parchure, T. M. [eds.]. 2007. Organic-rich fine sediments in Florida, Part II: Resuspension in a lake.

Hamilton, D. P., and Mitchell, S. F. 1997. Wave-induced shear stresses, plant nutrients and chlorophyll in seven shallow lakes. Freshwater Biology **38:** 159-168.

Hamilton, D. P., and Schladow, S. G. 1997. Prediction of water quality in lakes and reservoirs .1. Model description. Ecological Modelling **96:** 91-110.

Hawley, N., and Lesht, B. M. 1992. Sediment Resuspension in Lake St-Clair. Limnology and Oceanography **37:** 1720-1737.

Holdren, G. C., and Montaño, A. 2002. Chemical and Physical Limnology of the Salton Sea -1999. U.S. Department of the interior Bureau of Reclamation.

Imberger, J., and Patterson, J. 1981. A Dynamic Reservoir Simulation Model - DYRESM 5. *In* Fischer, H. B. [ed.], Transport Models for Inland and Coastal Waters. Academic Press.

Imberger, J. P., J.;Hebbert, B.;Loh, I. 1978. Dynamics of Reservoir of Medium Size. Journal of the Hydraulics Division-Asce **104:** 725-743.

Jellison, R., Miller, L. G., Melack, J. M., and Dana, G. L. 1993. Meromixis in Hypersaline Mono Lake, California .2. Nitrogen Fluxes. Limnology and Oceanography **38:** 1020-1039.

Jørgensen, S. E., Kamp-nielsen, L., Christensen, T., Windolf-nielsen, J., and Westergaard, B. 1986. Validation of a Prognosis Based Upon a Eutrophication Model. Ecological Modelling **32:** 165-182.

Loague, K., and Green, R. E. 1991. Statistical and graphical methods for evaluating solute transport models: Overivew and application. Journal of Contaminant Hydrology **7:** 51-73.

Losada, J. P. 2001. A Deterministic Model for Lake Clarity; Application to Management of Lake Tahoe (California-Nevada), USA. University of Girona.

Mayer, D. G., and Butler, D. G. 1993. Statistical Validation. Ecological Modelling **68:** 21-32.

McCord, S. A. 1999. The effects of artificial mixing on lake water quality. Dissertation. University of California, Davis.

McGill, R., Tukey, J. W., and Larsen, W. A. 1978. Variations of Box Plots. American Statistician **32:** 12-16.

Mei, C. C., Fan, S. J., and Jin, K. R. 1997. Resuspension and transport of fine sediments by waves. Journal of Geophysical Research-Oceans **102:** 15807-15821.

Ni, J. Q. 1999. Mechanistic models of ammonia release from liquid manure: a review. Journal of Agricultural Engineering Research **72:** 1-17.

OECD. 1982. Eutrophication of waters. Monitoring, assessment and
control. OECD.

Oreskes, N., Shraderfrechette, K., and Belitz, K. 1994. Verification, Validation, and Confirmation of Numerical-Models in the Earth-Sciences. Science **263:** 641-646.

Poisson, A., Gadhoumi, M. H., and Morcos, S. 1991. Salinity and density of seawater: Tables for high salinities (42 to 50).

Power, M. 1993. The Predictive Validation of Ecological and Environmental-Models. Ecological Modelling **68:** 33-50.

Reckhow, K. H. 1980. Techniques for Exploring and Presenting Data Applied to Lake Phosphorus Concentration. Canadian Journal of Fisheries and Aquatic Sciences **37:** 290-294.

Reckhow, K. H., and Chapra, S. C. 1983. Confirmation of Water-Quality Models. Ecological Modelling **20:** 113-133.

Reckhow, K. H., Clements, J. T., and Dodd, R. C. 1990. Statistical Evaluation of Mechanistic Water-Quality Models. Journal of Environmental Engineering-Asce **116:** 250-268.

Rykiel, E. J. 1996. Testing ecological models: The meaning of validation. Ecological Modelling **90:** 229-244.

Sanford, L. P., and Halka, J. P. 1993. Assessing the Paradigm of Mutually Exclusive Erosion and Deposition of Mud, with Examples from Upper Chesapeake Bay. Marine Geology **114:** 37-57.

Sanford, L. P., and Maa, J. P. Y. 2001. A unified erosion formulation for fine sediments. Marine Geology **179:** 9-23.

Schladow, S. G., and Hamilton, D. P. 1997. Prediction of water quality in lakes and reservoirs .2. Model calibration, sensitivity analysis and application. Ecological Modelling **96:** 111-123.

Schladow, S. G., Robertson, D. M., Hook, S. J., Chung, E. G., Losada, J. P., Cardona, B. M., Palmarsson, S. O., Steissberg, T. E., and Fleenor, W. E. 2004. Salton Sea Nutrients TMDL Modeling Studies. Colorado River Basin Regional Water Quality Control Board.

Schlesinger, W. H. 1991. Biogeochemistry, An Analysis of Global Change. Academic Press, Inc.

Stow, C. A., Roessler, C., Borsuk, M. E., Bowen, J. D., and Reckhow, K. H. 2003. Comparison of estuarine water quality models for total maximum daily load development in Neuse River Estuary. Journal of Water Resources Planning and Management-Asce **129:** 307-314.

Walker, W. W. J. 1986. Empirical Methods for Predicting Eutrophication in Impoundments; Report 3, Phase III: Applications Manual. U.S. Army Engineer Waterways Experiment Station.

CHAPTER 5: SUMMARY AND CONCLUSIONS

The Salton Sea is currently a hyper-eutrophic water body characterized by low oxygen concentrations, massive fish kills, noxious odors and possibly related bird kills. Recent water quality modeling conducted by the University of California, Davis, indicated that eutrophication in the Sea is driven primarily by nutrients associated with sediment resuspension and suggests that inflow control alone will not produce the desired state. The possibility that resuspension-driven, internal nutrient loading may be such a dominant factor in the ecological status of the sea casts uncertainty on the future restoration efforts. Alternative restoration scenarios have been developed by groups with a direct interest in the Sea, although none have yet been adopted by the State. As the Sea recedes (due to the 20% inflow reduction) or if, as appears possible, a massive construction project is undertaken to change the physical construction of the Sea, the extent and the effects of sediment resuspension will change. Furthermore, the effectiveness of any scenario may be impossible to determine without better information on sediment resuspension, since the Sea's ecological restoration is still tied to controlling the nutrient fluxes that drive the process of eutrophication.

The UC Davis research involved a 24-month study (including a 4-month measurement program) in the Salton Sea to directly measure sediment resuspension using an array of OBS instruments and a wave height and current profiling instrument (AWAC). The data provided by these instruments, in conjunction with existing UC Davis temperature recording instruments in the Sea and the existing CIMIS meteorological network, point to the existence of a quasi-equilibrium condition for the suspension of sediments in the lake, where there is a clear cause-effect relation between wind intensity- waves- suspended sediment.

Scaling analyses provided a framework of existing entrainment formulations for *cohesive* and non-*cohesive* sediment. The framework has been useful in this research to define suitable exponent values for the variables, such as wind speed, which is related to suspended sediments. For non-*cohesive* sediments, the range of variation of exponents (2–10) is larger than the range for *cohesive* sediment (2–4). The exponent of the formula by Mian and Yanful (2004) for *cohesive* sediment, 4, is very close to the exponent for non-*cohesive* sediment, 5. Non-linear relations were developed between the wind intensity and turbidity near the bottom at three monitoring stations including Stations 4 m and 6 m bottom. The powers ranged between 4 and 5, depending on water depths, and were in relative agreement with relationships from reviewed literature.

The observed data also confirmed that the bed shear stress due to wind-induced waves is more dominant than bed shear stress due to currents. The relationships of Mian and Yanful (2004) were adopted along with an extended García and Parker formulation to estimate sediment entrainment rates in the Salton Sea. The simulated sediment entrainment rates were based on the bed shear stress due to wind-induced waves, where the wave characteristics were simulated using the SMB method.

To improve the empirical sediment resuspension model presently in DLM-WQ, three additional sediment models, including the a linear relation between sediment entrainment rate and bed shear stress, Mian and Yanful (2004) and García and Parker

(1991; 1993), were incorporated into DLM-WQ. Each sediment resuspension model was then compared to one another using statistical evaluation methods. Simulations with the calibrated models suggest that sediment resuspension of nutrients in both particulate and dissolved form (from sediment porewater) is presently the most dominant factor in the Sea's nutrient cycling. From the comparison among the four sediment models, three of the new sediment models improved the model predictions over the existing sediment model, Somlyody (1986). In particular, the extended García and Parker formulation with DLM-WQ shows the best prediction to describe the seasonal trends as well as short-term variations.

The DLM-WQ, combined with this new sediment model, was used to more fully explore the potential for ecological restoration of the Salton Sea under possible future configurations. Two scenarios, the North Sea Combined Alternative and South Sea Combined Alternative, as suggested by PEIR were examined. The simulation of North Sea Combined Alternative indicates that the Marine Sea might have a better eutrophic status than that of the whole Sea because of fewer sediment resuspension events due to lower average wind speed acting on a smaller surface. On the other hand, the simulation of South Sea Combined Alternative suggested that the concentrations of nutrients in the water column would be the same or higher than those of the whole Sea, because of more sediment resuspension events due to higher average wind speed and due to shallower water depth. In the both alternatives, however, the anoxia in the hypolimnion would be spatially and temporally increased due to increased stratification periods, during which time toxic substances (including odorous hydrogen sulfide) and organic materials could be accumulated in the sediments.

DLM-WQ with the new sediment resuspension algorithm successfully accounts for the dominant processes that control eutrophication in the current Salton Sea and provides an indication of variations in properties that could be expected in potential future configurations. In addition to being a tool for comparing future configurations, DLM-WQ provides a basis for designing future monitoring needs.

APPENDIX 1: RELATIONS BETWEEN SEDIMENT ENTRAINMENT AND SHEAR STRESS

The various relationships mentioned in Table 1.1 are reviewed about sediment entrainment, E, as a function of flow parameters, such as the bed shear stress, τ_b, and wind velocity, Ua, as shown in the equation (1.3).

NON COHESIVE SEDIMENT

Garcia and Parker (1991, 1993)

$$E = \frac{AZ_u^5}{\left(1+\frac{A}{0.3}Z_u^5\right)} = \frac{A}{\left(\frac{1}{Z_u^5}+\frac{A}{0.3}\right)};$$

$$A = 1.3e-7;$$

$$Z_u \approx 0.1 \Rightarrow \frac{1}{Z_u^5} = 1e^5$$

$$\Rightarrow E \sim Z_u^5$$

$$Z_u = \frac{u_* R_p^{0.6}}{\nu_s};\ Z_u \sim u_*.$$

$$u_* \sim \tau_b^{1/2};\ Z_u \sim \tau_b^{1/2}.$$

$$\Rightarrow E \sim \tau_b^{5/2}$$

$$E \sim U_a^5 \Leftarrow \tau_b \sim U_a^2 \text{ for currents}$$

Smith and McLean (1977)

$$c_{ae} = \frac{0.65\gamma_0 T}{1+\gamma_0 T};\ T = \frac{\tau_s^* - \tau_c^*}{\tau_c^*};$$

$$\gamma_0 = 2.4 \cdot 10^{-3}$$

$$E \approx \frac{0.65\gamma_0 T}{1+\gamma_0 T} = \frac{0.65\gamma_0}{\frac{1}{T}+\gamma_0} = \frac{1.56e-3}{\frac{1}{T}+2.4e-3} \quad \because \frac{1}{T} \sim 20$$

$$E \sim \frac{1}{\frac{1}{T}} \sim T \ \because \frac{1}{T} \sim 20$$

$$E \sim \tau_s^* \sim \tau_b \ \because \tau_b^* = \frac{\tau_b}{\rho g R D} \sim \tau_b$$

$$E \sim U_a^2 \ \Leftarrow \ \tau_b \sim U_a^2 \text{ for currents}$$

Itakura and Kishi (1980)

$$c_{ae} = k_1\left(k_2 \frac{u_*}{\nu_s}\frac{\Omega}{\tau^*} - 1\right);\ \Omega = \frac{\tau^*}{k_3}\left(k_4 + \left[\frac{\exp\left(-A_0^2\right)}{\int_{A_0}^{\infty}\exp\left(-\xi^2\right)d\xi}\right]\right) - 1;$$

$$A_0 = \frac{k_3}{\tau^*} - k_4;\ k_1 = 0.008; k_2 = 0.14; k_3 = 0.143; k_4 = 2.0$$

$$E \approx k_1\left(k_2 \frac{u_*}{\nu_s}\frac{\Omega}{\tau^*} - 1\right)$$

$$A_0 \sim \frac{1}{\tau^*} \sim \tau^{*-1} \ \Leftarrow A_0 \approx \frac{0.143}{0.05} - 2$$

$$\Omega \sim \tau^* \exp\left(-\left(\tau^{*-1}\right)^2\right)$$

$$E \sim \frac{u_*}{\tau^*}\Omega \sim \frac{u_*}{\tau^*}\tau^* \exp\left(-\left(\tau^{*-1}\right)^2\right)$$

$$E \sim u_* \exp\left(-\left(\tau^{*-1}\right)^2\right)$$

Van Rijn (1984)

$$c_{ae} = 0.015\frac{D_s}{b}\frac{T^{1.5}}{D_*^{0.3}};\ D_* = D_s\left(\frac{gR}{\nu^2}\right)^{1/3}$$

$$E \approx 0.015\frac{D_s}{b}\frac{T^{1.5}}{D_*^{0.3}}$$

$$E \sim T^{1.5} \sim \tau_s^{*1.5} \sim \tau_b^{1.5} \ \because \tau_b^* = \frac{\tau_b}{\rho g R D} \sim \tau_b$$

$$E \sim U_a^3 \Leftarrow \tau_b \sim U_a^2 \text{ for currents}$$

Celik and Rodi (1984)

$$c_{ae} = \frac{k_0 C_m}{I};\ C_m = 0.034\left[1-\left(\frac{k_s}{H}\right)^{0.06}\right]\frac{u_*^2}{gRH}\frac{U_m}{\nu_s};\ I = \int_{0.05}^{1}\left(\frac{1-\eta}{\eta}\cdot\frac{\eta_b}{1-\eta_b}\right)^{\nu_s/0.4u_*} d\eta;$$

$$\eta = z/H;\ \eta_b = 0.05;\ k_0 = 1.13$$

$$C_m \sim u_*^2 U_m$$

$$U_m = u_*\left[\frac{1}{k}\ln\left(\frac{z}{k_s}\right)+8.5\right] \sim u_*$$

$$C_m \sim u_*^3$$

$$E \approx \frac{k_0 C_m}{I} \sim C_m \sim u_*^3 \sim \tau_*^{3/2} \ \because\ \tau^* = \frac{u_*^2}{RgD}$$

$$E \sim \tau_b^{3/2} \ \because\ \tau_b^* = \frac{\tau_b}{\rho g R D} \sim \tau_b$$

$$E \sim U_a^3 \Leftarrow \tau_b \sim U_a^2 \text{ for currents}$$

Akiyama and Fukushima (1986)

$$E_s = 0;\ Z < Z_c$$

$$E_s = 3\cdot 10^{-12} Z^{10}\left(1-\frac{Z_c}{Z}\right);\ Z_c < Z < Z_m$$

$$E_s = 0.3;\ Z > Z_m$$

$$Z = \frac{u_*}{\nu_s} R_p^{0.5};\ R_p = \frac{\sqrt{gRD_s}D_s}{\nu};\ Z_c = 5;\ Z_m = 13.2$$

$$Z \cong \frac{0.008859}{1.00\text{E-}06}1.99 = 1.76\text{E}+04 >> \text{Z}_\text{c}$$

if $u_* = 0.008859$ when $\tau^* = 0.05$

$$\nu_s = 1.00\text{E-}06;\ R_p^{0.5} = 1.99;\ R_p = 3.95;$$

$$E \sim Z^{10} \ \because 1 >> \frac{Z_c}{Z}$$

$$E \sim \left(\frac{u_*}{\nu_s} R_p^{0.5} \right)^{10} \sim u_*^{10} \sim \tau_*^5 \ \because \ \tau^* = \frac{u_*^2}{RgD}$$

$$E \sim \tau_b^5 \ \because \ \tau_b^* = \frac{\tau_b}{\rho g R D} \sim \tau_b$$

$$E \sim U_a^{10} \ \Leftarrow \ \tau_b \sim U_a^2 \ \text{for currents}$$

Zyserman and Fredsoe (1994)

$$c_{ae} = \frac{0.331\left(\theta' - 0.045\right)^{1.75}}{1 + \frac{0.331}{0.46}\left(\theta' - 0.045\right)^{1.75}}; \ \theta' = \frac{\left(u_{*s}\right)^2}{RgD_s}$$

$$E \approx \frac{0.331\left(\theta' - 0.045\right)^{1.75}}{1 + \frac{0.331}{0.46}\left(\theta' - 0.045\right)^{1.75}} = \frac{0.331}{\frac{1}{\left(\theta' - 0.045\right)^{1.75}} + \frac{0.331}{0.46}} \sim \frac{1}{\frac{1}{\left(\theta' - 0.045\right)^{1.75}}}$$

$$E \sim \left(\theta' - 0.045\right)^{1.75} = \left(\tau_s^* - 0.045\right)^{1.75}$$

$$E \sim \tau_s^{*1.75} \sim \tau_b^{1.75} \ \because \ \tau_b^* = \frac{\tau_b}{\rho g R D} \sim \tau_b$$

$$E \sim U_a^{3.5} \ \Leftarrow \ \tau_b \sim U_a^2 \ \text{for currents}$$

COHESIVE SEDIMENT

Mian and Yanful (2004)

$$E = \alpha \left[\frac{\tau - \tau_{cr}}{\tau_{cr}} \right]^m \qquad \text{for } \tau \geq \tau_{cr}$$

$$E = 0 \qquad \text{for } \tau < \tau_{cr}$$

$$E \sim \tau^m$$

if m = 2, $E \sim \tau^2 \sim U_A^4$

Kandiah (1974); Arulanandan (1975)

$$\varepsilon = \alpha_3 \left(\frac{\tau - \tau_c}{\tau_c} \right)$$

$$\Rightarrow E \sim \tau \sim U_A^2$$

Mehta (1981)

$$\frac{\varepsilon - \varepsilon_{ch}}{\varepsilon_{ch}} = \alpha_6 \left(\frac{\tau - \tau_{ch}}{\tau_{ch}} \right)$$

$$\Rightarrow E \sim \tau \sim U_A^2$$

Thorn and Parsons (1980)

$$\varepsilon = \delta_3(z)[\tau - \tau_c(z)]$$

$$\Rightarrow E \sim \tau \sim U_A^2$$

APPENDIX 2: PUBLISHED MANUSCRIPTS

Chung, E. G., Schladow, S. G., Perez-Losada, J., Robertson, D. M. 2007. A Linked Hydrodynamic and Water Quality Model for the Salton Sea. In press, Hydrobiologia.